

UNIVERSITY OF OKLAHOMA
GRADUATE COLLEGE

RECONSTRUCTING RESTING STATE NETWORKS FROM EEG

A DISSERTATION
SUBMITTED TO THE GRADUATE FACULTY
in partial fulfillment of the requirements for the
Degree of
DOCTOR OF PHILOSOPHY

By

CHUANG LI
Norman, Oklahoma
2018

RECONSTRUCTING RESTING STATE NETWORKS FROM EEG

A DISSERTATION APPROVED FOR THE
SCHOOL OF ELECTRICAL AND COMPUTER ENGINEERING

BY

Dr. Lei Ding, Chair

Dr. Michael Wenger

Dr. Bin Zheng

Dr. Jerzy Bodurka

Dr. Joseph Havlicek

© Copyright by CHUANG LI 2018
All Rights Reserved.

Acknowledgements

Firstly, I would like to express my gratitude to Dr. Lei Ding for his guidance: he provided tremendous academic support and valuable advice. Through writing this dissertation and carrying out the studies, I learned a lot about the academic research. Without his guidance and persistent help, this dissertation would not have been possible.

Besides, I would like to thank my committee members, Dr. Michael Wenger, Dr. Bin Zheng, Dr. Jerzy Bodurka, and Dr. Joseph Havlicek, who provided me with constructive suggestions on my research.

I would like to thank Dr. Yoon-Hee Cha and her lab at the Laureate Institute for Brain Research, Tulsa, for their assistance with the collection of experimental data. I would also like to thank Dr. Yuan Han and Dr. Guofa Shou for their support in my studies.

Moreover, I am deeply grateful to Lisa Wilkins, who unfortunately passed away in 2017. It is her kindly help and encouragement that makes me go through hard times.

Finally, but by no means least, I would like to thank Dr. Yao Fu, Erdnuss Fu, and all my family members for their physical and mental support. They are the most important people in my world.

Table of Contents

Acknowledgements	iv
Table of Contents	v
List of Tables	ix
List of Figures.....	x
Abstract.....	xii
1 Introduction	1
2 Background.....	9
2.1 Introduction to Resting State Networks	10
2.2 Resting-State Recording with EEG	13
2.2.1 Techniques for Resting-State Recording.....	14
2.2.2 Introduction to EEG	17
2.2.3 Resting-State EEG.....	19
2.2.4 Inverse Source Imaging of EEG.....	20
2.3 Methods for Analyzing Resting State EEG.....	23
2.3.1 Seed-based Connectivity Analysis	23
2.3.2 Independent Component Analysis.....	24
3 Resting State Networks in the Sensor Space and the Source Space.....	27
3.1 Introduction	27
3.2 Materials and Methods	29
3.2.1 Simulated EEG Data.....	29
3.2.2 Experimental EEG Data	30
3.2.3 Sensor-space ICA and Source-space ICA	31

3.2.4	Evaluation of Simulation Results	33
3.2.5	Evaluation of Experimental Results	33
3.3	Results	34
3.3.1	Simulation Results.....	34
3.3.2	Experimental EEG Data	36
3.4	Discussion and Summary	39
4	Frequency Domain and Statistical Correlation Tomography of Resting State Networks.....	42
4.1	Introduction	42
4.2	Materials and Methods	45
4.2.1	Cortical Statistical Correlation Tomography of RSNs.....	45
4.2.2	Experimental Protocols	51
4.2.3	Data Analysis Protocols	53
4.2.4	Evaluation and Validation Protocols	55
4.3	Results	58
4.3.1	Spatial and Spectral Patterns of RSNs.....	58
4.3.2	TFICA-SCT derived RSNs vs. fMRI derived RSN templates	63
4.3.3	Consistency of RSNs across different datasets	65
4.3.4	Contrast resolutions of EEG RSNs revealing condition differences	66
4.4	Discussion and Conclusion.....	69
5	An Advanced Inverse Source Imaging Method for Reconstructing EEG Resting State Networks.....	79
5.1	Introduction	79

5.2	Materials and Methods	83
5.2.1	Variation and Wavelet-based Sparse Source Imaging	83
5.2.2	Computational Framework to Reconstruct RSNs	86
5.2.3	Construction of Models	88
5.2.4	Simulation Protocols	88
5.2.5	Experimental Protocols	90
5.2.6	Data Analysis Protocols	91
5.2.7	Evaluation Protocols.....	92
5.3	Results	95
5.3.1	Simulation.....	95
5.3.2	Experiment	99
5.4	Discussion.....	104
6	Assessing EEG Resting State Networks Changes in Different Conditions	111
6.1	Introduction	111
6.2	Materials and Methods	113
6.2.1	Assessing RSN Changes in Different Conditions	113
6.2.2	Simulation Protocols	116
6.2.3	Experimental Data	119
6.2.4	Analysis and Evaluation Protocols.....	119
6.3	Results	121
6.3.1	Simulation.....	121
6.3.2	Experiment	125
6.4	Discussion and Summary	130

7	Discussion and Conclusion.....	134
7.1	Summary of the Findings	135
7.2	Limitations and Future Works.....	139
7.3	Conclusion.....	141
8	References	143

List of Tables

Table 4-1 Summary of spectral power differences.....	69
--	----

List of Figures

Figure 2.1 Multiple Resting State Networks identified with fMRI.....	12
Figure 2.2 Schematic of fMRI, MEG, and EEG systems.....	14
Figure 2.3 Physics of BOLD fMRI	16
Figure 2.4 Structure of neuron and cortical generator of EEG signals	19
Figure 2.5 Schematic of inverse source imaging.....	21
Figure 2.6 Schematic of seed-based connectivity analysis	24
Figure 2.7 Schematic of temporal group-ICA	26
Figure 3.1 An example of simulated sources and the reconstruction from two ICA procedures.....	35
Figure 3.2 Spatial and temporal correlation coefficients of two ICA procedures	36
Figure 3.3 Spatial and spectral patterns of RSNs from two ICA procedures.....	38
Figure 4.1 Diagram of TFICA-SCT	46
Figure 4.2 Spatial and spectral patterns of RSNs from the EC/EO EEG data	61
Figure 4.3 Spatial and spectral patterns of RSNs from the HC/MdDS EEG data.....	62
Figure 4.4 Spatial and spectral patterns of RSNs from the Pre-/Post-rTMS EEG data .	63
Figure 4.5 Template-matching degree (TD) between RSNs and fMRI RSN templates	64
Figure 4.6 TD between a pair of SCTs from two different datasets.....	66
Figure 4.7 SCT differences between data from two conditions	68
Figure 5.1 Schematic of the simulation.....	89
Figure 5.2 Spatial and temporal reconstruction of the simulation.....	97
Figure 5.3 Performance of VW-SSI and MNE in the simulation.....	98
Figure 5.4 Spatial and spectral patterns of RSNs from VW-SSI	99

Figure 5.5 Spatial and spectral patterns of RSNs from MNE	100
Figure 5.6 Spatial TD between spatial patterns and fMRI RSN templates	104
Figure 6.1 Schematic of the simulation	118
Figure 6.2 Simulation results of comparisons	123
Figure 6.3 Examples of Simulation Results of linear relationships	124
Figure 6.4 Spatial patterns of RSNs	126
Figure 6.5 RSN differences between HCs and MdDS	128
Figure 6.6 Linear relationships between ICC and VAS	129

Abstract

Resting state networks (RSNs) have been found in human brains during awake resting states. RSNs are composed of spatially distributed regions in which spontaneous activity fluctuations are temporally and dynamically correlated. In contrast to task-related brain activities, RSNs reflect intrinsic functional organizations and rhythms of the human brain when it is not engaged in any task and/or disturbed by external stimuli. To date, RSNs have been widely studied using functional magnetic resonance imaging (fMRI), which has identified various RSNs associated with different brain functions. More recently, due to the advantage of millisecond temporal resolution, both electroencephalography (EEG) and magnetoencephalography (MEG) have been used to investigate RSNs and their electrophysiological underpinnings. Despite these advantages, current RSN studies using EEG/MEG, as compared with those using fMRI, are still at their infant stage in many aspects, such as the quality of spatial pattern reconstructions and the reliability of detections. These limitations require further studies to obtain accurate reconstructions of RSNs directly from EEG/MEG data.

My research aims to develop, optimize, and validate a variety of computational and analytical frameworks to reconstruct and investigate RSNs based on EEG data. In this dissertation, several studies have been conducted as outlined below. Firstly, a comparison in defining RSNs at the sensor space and at the source space was performed to evaluate the accuracy in reconstructing RSN spatial patterns. Results from both simulated and experimental data indicated that the analysis in the source space performed better in reconstructing various features of RSNs. Secondly, a new computational framework for reconstructing RSNs with human EEG data was developed. The proposed

framework utilized independent component analysis (ICA) on short-time Fourier transformed inverse source maps imaged from EEG data and statistical correlation analysis to generate cortical tomography of electrophysiological RSNs. The proposed framework was validated using three sets of experimental data. The results indicated that the framework is reliable and efficient in the reconstruction of RSNs. Thirdly, an advanced inverse source imaging (ISI) method was used in the established framework discussed above to improve the spatial estimation of RSNs. The comparison between the new and conventional frameworks suggested that the ISI method significantly improved the accuracy of spatial estimations of RSNs. Fourthly, an ICA-based framework was used to assess RSN alternations under different conditions, which has been the model to identify imaging biomarkers, for example, for diseased patients as compared with healthy control. The results from both simulated and experimental data indicated that the framework could detect RSN alternations due to condition differences. My results further suggest that the framework could provide a finer resolution in detecting RSN changes as a contrast for multi-level (more than 2) condition differences, which can be used to study the difference, for example, among patients with a long history of a certain disorder, a short history, and healthy control. Overall, the findings of this dissertation study provided insights into the underlying electrophysiological basis of RSNs. More importantly, this study developed new frameworks that can be used as powerful tools for future investigations of more characteristics of RSNs, in particular for those not available in fMRI, e.g., spectral patterns.

1 Introduction

The human brain is a highly complex, interconnected structure with over 100 billion neurons, which are anatomically organized into networks distributed within and between neural systems (Herculano-Houzel, 2009; Oh et al., 2014). Human brain networks facilitate efficient communication among distinct brain regions, enabling the global integration of information (Ward, 2003). The integrative architecture determines the underlying principles of how the neurons work synergistically to realize different brain functions (Park and Friston, 2013). Therefore, understanding and modeling human brain functions are based not only on the identification of brain regions but also on the investigation of functional networks.

To date, there has been growing interest in probing structural and functional patterns of brain networks (Bressler and Menon, 2010; Castellanos and Proal, 2012; Menon, 2011). Recent research has shown that most of the cognitive and executive functions are dependent on brain networks, rather than on a single brain region (Bressler and Menon, 2010; Sridharan et al., 2008). In these task-related networks, different areas of the brain communicate efficiently in order to exchange information, perform their functions, and provide feedback for particular tasks. For instance, enhanced communication has been detected between the visual cortex and the somatosensory/motor cortex during associative learning (Miltner et al., 1999).

Traditionally, studies of brain functions have focused on task-related networks. However, the brain is not always engaged in imposed tasks or external stimuli, and it is attractive to investigate brain networks during the resting state because they reflect intrinsic and fundamental characteristics of the brain. Through assessing brain activities

during the resting state, studies reported on the existence of resting state networks (RSNs), which are formed by the spontaneous fluctuations in distributed brain regions when the brain is awake but resting (Biswal et al., 1995; Biswal, 2012). In contrast to task-related networks, RSNs reflect brain functions beyond explicit tasks and represent the intrinsic functional architecture of the brain (Smith et al., 2009). The discovery of RSNs provides a novel perspective to investigate and understand the nature of brain, which is followed by a growing body of research regarding RSNs in the past two decades (Finn et al., 2015; Hipp et al., 2012; Yuan et al., 2016). So far, studies concerning RSNs have provided encouraging results, such as spatial distributions (Biswal, 2012; Yuan et al., 2016) and characteristics of network connectivity (Brookes et al., 2011b; Chen et al., 2013; Hipp et al., 2011). Despite these exciting advances, our understanding of RSNs is still preliminary, which requires further studies.

In order to record brain signals during the resting state, different neuroimaging techniques have been used, including functional magnetic resonance imaging (fMRI), electroencephalography (EEG), and magnetoencephalography (MEG) (Biswal et al., 1995; Brookes et al., 2011b; Yuan et al., 2016). Since the discovery of RSNs in 1995 (Biswal et al., 1995), fMRI has been extensively used in RSN studies (Biswal et al., 1995; Biswal, 2012). fMRI offers high spatial resolution by measuring blood-oxygenation-level-dependent (BOLD) signals. However, its temporal resolution is relatively low, precluding analyses on temporal information of fast neural oscillations (Logothetis, 2008). In the past decade, MEG and EEG have also been used to study RSNs (Brookes et al., 2011a; Hipp et al., 2011; Sockeel et al., 2016). In contrast to fMRI, MEG and EEG directly measure the neural activity by recording the magnetic fields or the electrical

potentials generated by the neuron's electrical activity. Although MEG and EEG have a spatial resolution that is relatively coarse compared to fMRI, both techniques offer excellent temporal resolution, which provides insights into the temporal characteristics of RSNs (Cohen et al., 1990; da Silva, 2013; Klimesch, 1999; Michel et al., 2004; Mosher et al., 1999). Due to their advantages, MEG and EEG have been increasingly used in studies regarding RSNs (Brookes et al., 2011a; Hipp et al., 2011; Sockeel et al., 2016). Some of these studies generated spatial patterns with significant similarity to RSNs derived from fMRI data (Brookes et al., 2011b; Liu et al., 2017; Ramkumar et al., 2012; Yuan et al., 2016). More importantly, some of these studies revealed RSN characteristics that are beyond the capability of fMRI (Ding et al., 2014; Li et al., 2018).

To detect and probe RSNs based on EEG and MEG data, earlier studies have proposed and adopted various frameworks consisting of multiple computational and analytical methods that served different purposes within the whole frameworks (Liu et al., 2017; Ramkumar et al., 2012; Sockeel et al., 2016). For instance, inverse source imaging (ISI) (Grech et al., 2008; Pascual-Marqui, 1999), which estimates underlying sources on the cortical surface based on MEG/EEG data, has been widely used in RSN studies in which analyses were conducted in the cortical space (Brookes et al., 2011b; Yuan et al., 2016). On the other hand, independent component analysis (ICA) has also been widely used to identify RSNs from both EEG/MEG data (Brookes et al., 2011b; Hipp et al., 2012). ICA is a data-driven method which decomposes data from linear mixed signals into components with maximal statistical independence (Lee et al., 1999). In frameworks using ICA, RSNs were generated based on independent components from ICA (Brookes et al., 2011b; Liu et al., 2017). Both ISI and ICA have been extensively

employed as analytical steps in frameworks concerning MEG/EEG RSNs. Among the previously developed frameworks, the advancement in frameworks mainly emerged from the collective contribution of these component methods, such as the adopted methods (i.e., what to use), the implementation of methods (i.e., how to use), and even the sequence of methods (i.e., when to use) (Calhoun et al., 2009; Li et al., 2017). For instance, ICA can be conducted either in the sensor space (Ding et al., 2014) or in the source space (Li et al., 2018) to derive RSNs in different domains. The combination and implementation of multiple computational methods have produced various frameworks for RSN studies, which enables the reconstruction of RSNs and the exploration of different aspects. Despite recent development and findings of EEG/MEG RSNs, there are several limitations to the developed frameworks.

First, the sequence of different methods, which may affect the performance of a framework, has rarely been assessed regarding its influence on the reconstruction of RSNs. ISI and ICA, two critical methods used in current frameworks, can be used in either sequence. ICA can be applied to MEG/EEG data in the sensor space to generate topography of RSNs, which can be projected into the source space using ISI (Yuan et al., 2010). Or, ICA can be applied to data in the source space that are generated via ISI (Brookes et al., 2011b). Both sequences have been followed to explore RSNs, and meaningful patterns have been successfully found (Brookes et al., 2011b; Yuan et al., 2010; Yuan et al., 2012b). However, there has been no detailed investigation of their performance, which is required to give a direction in further improvement of computational frameworks for MEG/EEG RSNs.

Second, the strategy to explore the spectral characteristics of RSNs is limited. Spectral characteristics of RSNs are critical in the investigation of RSNs (Mantini et al., 2007). Analysis over the spectral domain can yield informative features of RSNs that is necessary to achieve a deeper understanding of RSNs. Previous studies used pre-selected band-pass filters to probe spectral characteristics in specific frequency bands (Brookes et al., 2011b; Mantini et al., 2007). This strategy, however, precludes the insight into spectral features over a wider band, which is necessary for an unbiased investigation. To date, this limitation has not been comprehensively examined.

Third, the group-level analysis on RSNs, which has been widely conducted in RSN studies, is not optimal to provide less-biased and convincing features of RSNs. Previous studies have only focused on group-level ICA, while group-level statistical analysis after ICA has not obtained enough research interest. For instance, the autocorrelation of signals, which determine the accuracy of the group-level analysis has been taken into consideration in fMRI studies (Honey et al., 2009; Rombouts et al., 2005; Roy et al., 2009; Woolrich et al., 2001). On the contrary, it has been largely overlooked in MEG/EEG RSN studies.

Fourth, little research has been done to explore the role of ISI in RSN studies. Previous studies of MEG/EEG RSNs typically focused on the analysis of cortical data, e.g., ICA (Liu et al., 2017; Yuan et al., 2016). Surprisingly, there has been little advancement in the ISI step of frameworks for EEG/MEG RSNs; only conventional ISI methods such as the minimum norm estimation (Hamalainen and Ilmoniemi, 1994) were used in proposed frameworks. Given the critical role of ISI, the estimation accuracy of ISI can further determine the quality of reconstructed RSNs. Thus, further research is

needed in order to evaluate the influence of ISI and to provide improved mathematical solutions.

The primary aim of this dissertation is to advance the reconstruction of RSNs from EEG data. In this dissertation, a comparison is conducted to evaluate the impact of method arrangement in computational frameworks; a new ICA method is proposed to probe spatial and spectral features of RSNs; advanced statistical analysis is developed to provide a statistical justification for spatial definition; a new ISI method is used in an RSN-reconstructing framework. Using both experimental EEG data and simulated data, comparisons are conducted to identify the performance difference, and proposed frameworks are evaluated from a different perspective. This study makes important contributions to multiple aspects of computational frameworks for RSN reconstruction, such as a new type of ICA and an advanced ISI method, which gives us a deeper understanding of RSNs.

The overall structure of this dissertation takes the form of seven chapters.

Chapter 2 gives a brief introduction about RSNs to help the reader understand where the contribution of each study fits into the big picture of RSN reconstruction. The section begins with background knowledge of RSNs, including the history, the characteristics, and some of current findings. Next, EEG, the technique used in my studies, is described regarding how resting-state data are obtained with this technique. Then, an overview of current computational frameworks to analyze EEG RSNs is provided. Finally, the advantages and limitations of these frameworks are discussed to demonstrate the necessity of proposing new frameworks.

Chapter 3 examines the influence of the sequence by which ISI and ICA are applied in a framework for the RSN reconstruction. In this chapter, RSNs are reconstructed using two frameworks: 1) ICA is used before ISI to decompose sensor-space data. 2) ICA is performed after ISI to decompose source-space data. This study uses both experimental data and simulated data. Comparisons are conducted to evaluate the performance of two frameworks in terms of spatial, temporal, and spectral reconstructions. To our best knowledge, this study is the first attempt to determine an optimal sequence to apply ISI and ICA in RSN-reconstructing frameworks. This is an important study in this dissertation because it provides further justifications for employing one sequence over the other in later chapters.

Chapter 4 introduces a new computational framework, time-frequency ICA-based statistical correlation tomography, for reconstructing RSNs with EEG data. The proposed framework utilizes ICA on short-time Fourier transformed EEG data to include the spectral domain in RSN analyses. Besides, statistical correlation analysis is proposed to define the spatial coverage of RSNs. The spatial/spectral features, the spatial similarity to fMRI RSN templates and the robustness of the new framework are evaluated systematically using three sets of resting-state EEG data. The proposed framework significantly improves the spectral analysis of EEG RSNs. Moreover, it provides a statistical solution to the spatial definition of EEG RSNs, overcoming the shortage of statistical analyses confronting previous studies.

Chapter 5 shifts the research interest from ICA to improving the accuracy of ISI. Previous studies only employed conventional ISI methods that are limited in estimation accuracy. In this study, an advanced ISI method, variation and wavelet based sparse

source imaging (VW-SSI), is used in a computational framework to improve the reconstruction of RSNs, especially in the spatial aspect. This framework is similar to the one introduced in Chapter 4, but with the employment of VW-SSI in the ISI step. The performance of the framework is evaluated using both experimental and simulated data. The improvement is assessed by comparisons between this modified framework and a control framework that uses a conventional ISI method. This study sheds new light on the importance of ISI in RSN-reconstructing frameworks.

Chapter 6 uses the framework introduced in Chapter 4 to assess RSNs in different conditions. In this study, RSNs reflecting different conditions or condition levels are evaluated together using the proposed framework, aiming to find the difference between two conditions and detect the relationship between RSNs and condition levels. Simulated data are generated in order to quantitatively examine the capability of assessing RSNs. The proposed framework is also applied to experimental data including both healthy controls and patients with a balance disorder, aiming to find biomarkers that indicate the change of RSNs and the relationship between RSNs and the symptom severity.

Chapter 7 summarized and discussed the significance of the works and findings described in this dissertation. This chapter is subdivided into three sections. The first section gives a summary of the contributions made by the three studies, including the optimal ICA method, statistical correlation analysis, and the ISI method. The second section discusses the limitations of my studies and raises potential perspectives for future work. The third section provides the conclusion of this dissertation.

2 Background

The discovery of resting state networks (RSNs) is perhaps the most significant breakthrough in the research field of human neuroscience in the past century. RSNs identified in the human brain are formed by spontaneous activity fluctuations in distributed brain regions when people are in task-free and awake states. In contrast to brain networks evoked by imposed tasks or external stimulus, RSNs reflect intrinsic connectivity and inherent architecture of the human brain. Since its discovery in 1995 (Biswal et al., 1995), RSNs have been extensively studied in a large body of research, and the reported findings inform our understanding of the organizational and functional principles of the human brain. The exploration of RSN is promoted by the evolution of neuroimaging techniques and the advance of computational frameworks. To date, different neuroimaging techniques have been used to record brain activities during the resting state, including fMRI, MEG, and EEG (Biswal et al., 1995; Brookes et al., 2011b; Li et al., 2018). Each of these techniques has its advantages and disadvantages (Logothetis, 2008). Fortunately, the technological progress is reducing their deficiency and enhancing their benefits, making these techniques more useful for RSN research. On the other hand, various computational frameworks have been developed in order to obtain different features of RSNs. These frameworks employed a wide range of computational and analytical methods, each of which serves specific purposes in the whole pipeline.

The aim of this chapter is to introduce RSNs, neuroimaging techniques to record resting-state brain signals, and computational methods to study RSNs. In the beginning, the background knowledge of RSNs is provided. Then, EEG, the technique used in this dissertation, is introduced to explain the generation and the recording of signals. Finally,

a brief overview of current computational methods is given to help the reader understand how frameworks are developed and improved in this dissertation.

2.1 Introduction to Resting State Networks

The human brain can be approached as a complex network consisting of spatially distributed but functionally linked regions (Herculano-Houzel, 2009; Oh et al., 2014). When the human brain is engaged in imposed tasks or stimuli, networked brain regions process and integrate the external information cooperatively in order to give reasonable responses (Allison et al., 2000). Importantly, the interconnected architecture of the human brain persists in the absence of external disturbance. Previous studies have demonstrated that spontaneous neuronal activities in distributed brain regions are temporally correlated in the awake resting state, forming intrinsic networks known as resting state networks (RSNs) (Biswal et al., 1995; Brookes et al., 2011b; Greicius et al., 2007).

RSNs are attractive and valuable for neuroscientists. From a functional point of view, RSNs reflect the intrinsic functional architecture of the human brain (Biswal et al., 1995; Fox and Raichle, 2007; Vincent et al., 2007). Studies of RSNs provide an extensive understanding of the human brain. In terms of the experiment, RSN studies can be conducted on young children or patients who cannot finish complex tasks due to the age or disease. As a result of their significance and uniqueness, RSNs have become an indispensable part of neuroscience.

Research into RSNs has a long and tortuous history. Investigations of resting-state brain activities can be traced back to the 1950s. In 1955, the measurements of whole-brain blood flow and oxygen consumption obtained during the resting state were used in comparison with the task-performing state, which failed to detect any significant

difference in blood flow or oxygen consumption (Sokoloff et al., 1955). In 1988, using the technique of positron-emission tomography (PET), brain activities during the resting state were used as a control state to compare with brain activities during the stimulus, i.e., the vibration of the fingers on the left hand (Fox et al., 1988). This study, however, failed to reveal the significant role of resting-state data. In 1995, Biswal et al demonstrated that signals recorded by functional magnetic resonance imaging (fMRI) are temporally correlated within the somatomotor cortex, which revealed the existence of RSNs for the first time. However, the significance of the discovery of RSNs was not widely recognized in the early stage. A large amount of literature attributed the spontaneous connectivity to artifacts such as head motion or to the vasculature (Friston et al., 1996; Mitra et al., 1997). In 2003, Michael Greicius generated an image of default mode network (Greicius et al., 2003), which significantly supports the validity of RSNs. Since then, RSNs have become an important area of neuroimaging.

During the past two decades, considerable literature has grown up around the theme of RSNs. Researchers have detected multiple types of RSNs, such as the visual network, the frontoparietal network, and the default mode network (Brookes et al., 2011b; Fox and Raichle, 2007; Fox et al., 2005; Smith et al., 2009; Smith et al., 2012; Yeo et al., 2011; Yuan et al., 2017). Besides, these studies on RSNs have revealed encouraging findings, which mainly characterize the spatial, spectral, and temporal features of RSNs.

The spatial feature of RSNs indicates the interconnected brain regions included in a specific RSN, which provide an intuitive representation of the anatomical layout of a network. Previous studies have revealed distinct spatial signatures for different RSNs (Biswal et al., 1995; Calhoun and Adali, 2012). For instance, the default mode network

(DMN) (Figure 2.1(A)), the most attractive RSN, includes the medial prefrontal cortex, posterior cingulate cortex, inferior parietal lobules, and medial temporal regions (Greicius et al., 2003). On the contrary, the sensorimotor network (Figure 2.1(B)) includes somatosensory regions, motor regions, and the supplementary motor regions (Chenji et al., 2016). In a considerable number of previous studies, the spatial pattern of RSNs is an essential factor to categorize a specific RSN.

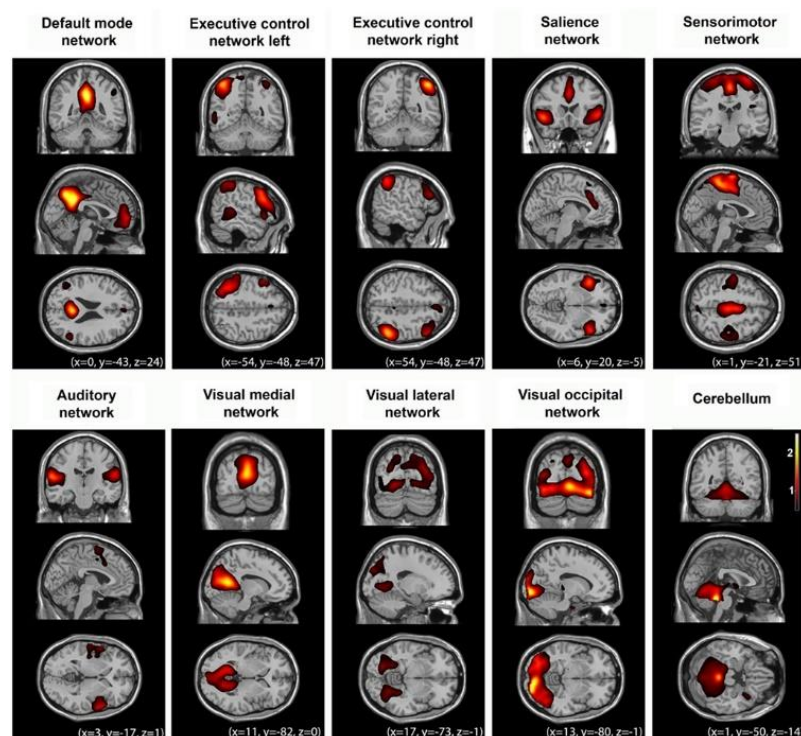


Figure 2.1 Multiple Resting State Networks identified with fMRI

(Figure as originally published in Heine L, Soddu A, Gómez F, Vanhaudenhuyse A, Tshibanda L, Thonnard M, Charland-Verville V, Kirsch M, Laureys S and Demertzi A (2012) Resting state networks and consciousness Alterations of multiple resting state network connectivity in physiological, pharmacological, and pathological consciousness states. *Front. Psychology* 3:295. doi: 10.3389/fpsyg.2012.00295, with permission)

The spectral feature of RSNs represents the properties of RSNs, e.g., power or connectivity, in the frequency domain. A critical finding of the RSN spectral feature is that the connectivity in RSNs varies across the frequencies of signals (Hipp et al., 2012; Mantini et al., 2007). By calculating the correlation of signals between pre-selected seed

regions within RSNs (auditory, somatosensory, and visual), Hawellek, Hipp et al obtained distributions of correlation over different frequencies and showed that the correlation is strongest in the alpha and the beta bands (Hawellek et al., 2011). This finding indicates that the functional connectivity within RSNs prefers specific rhythms.

The temporal feature of RSNs is mainly reflected in the temporal dynamics of connectivity. For a long time, the analysis of RSNs has been conducted under the assumption of temporal stationarity (Biswal et al., 1995; Greicius et al., 2003), i.e., the functional connectivity within RSNs is constant. However, recent research has shown that the functional connectivity within RSNs is variable over time (Chang and Glover, 2010; Chen et al., 2013). For example, Brookes, Groom et al. showed that the dynamics in attentional networks changes with age (Brookes et al., 2018).

In addition to the features mentioned above, RSNs exhibit interesting features that implicate their significance in health and disease. Specifically, previous studies have demonstrated the consistency of RSNs in healthy subjects (Beckmann et al., 2005; Damoiseaux et al., 2006), alterations in patients with neuropsychiatric disorders (Agosta et al., 2012; Greicius et al., 2007; Rombouts et al., 2005; Sorg et al., 2007), and changes with cognitive tasks (Buckner et al., 2008; Greicius et al., 2003). These findings are important because they reveal critical characteristics of RSNs and shed new light on the potential clinical utility of RSNs.

2.2 Resting-State Recording with EEG

Various neuroimaging techniques have been used to obtain brain signals during the resting state, including functional magnetic resonance imaging (fMRI), electroencephalography (EEG), and magnetoencephalography (MEG) (Figure 2.2)

(Biswal et al., 1995; Brookes et al., 2011b; Yuan et al., 2016). In this section, the description and discussion focus on EEG rather than the other two techniques because it was used to obtain resting-state data for this dissertation (see the following section). Besides, an important computational method for EEG is also introduced.

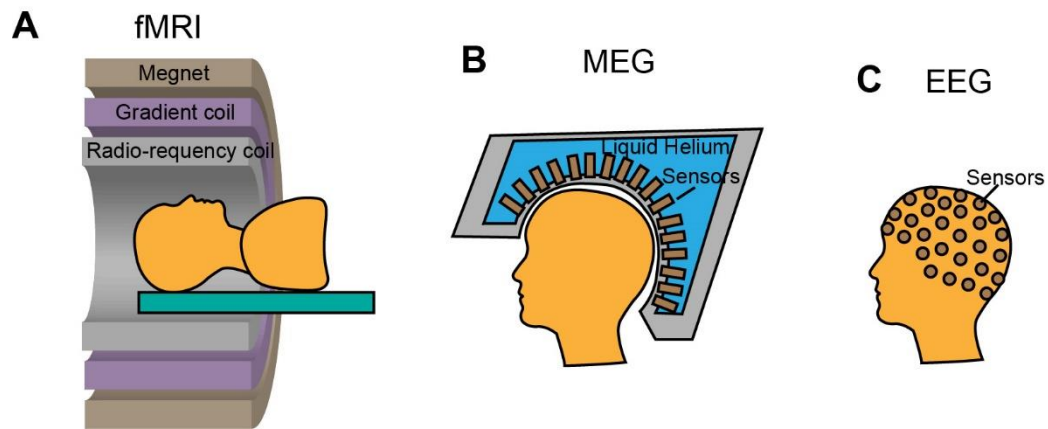


Figure 2.2 Schematic of fMRI, MEG, and EEG systems
(A) fMRI system. (B) MEG system. (C) EEG system.

2.2.1 Techniques for Resting-State Recording

Before a detailed description of EEG can be provided, a brief overview of popular neuroimaging techniques for RSN studies (i.e., fMRI, MEG, and EEG) is necessary to justify the selection of EEG in this dissertation. fMRI is an important neuroimaging technique and plays a critical role in RSN studies. Not only it was used to detect the first RSN, i.e., the sensorimotor network, (Biswal et al., 1995), but also it has been employed in a considerable amount of research which characterizes RSNs from different perspectives (Agosta et al., 2012; Chang and Glover, 2010; De Luca et al., 2006; de Pasquale et al., 2010).

Functional MRI measures the blood-oxygenation-level-dependent (BOLD) changes in the MRI signal that emerge when neuronal activity occurs in the brain. Increased neural activity in a brain region is accompanied by an increase in local blood

flow that meets the requirement of oxygen and other substrates in that region (Figure 2.3), which is more than the actual requirement. This, in return, results in a decrease in the concentration of deoxyhemoglobin. The changes in the oxygenation and blood flow, called hemodynamic changes, result in changes in the relative concentration of oxyhemoglobin and deoxyhemoglobin, which has a direct effect on the signals captured by fMRI. In particular, whether hemoglobin is saturated with oxygen affects its magnetic properties. When oxygen is bound to hemoglobin, forming oxygenated hemoglobin, it will be diamagnetic. However, when it is not bound to oxygen, forming deoxygenated hemoglobin, it becomes paramagnetic, which means it has significant magnetic moment that can affect the magnetization of the MRI machine. Thus, the changes in the concentration lead to an increase in the homogeneity of the static magnetic field which can be captured by BOLD fMRI. fMRI provides high spatial resolution on the order of millimeters, which is suitable for clinical and experimental practice. Due to its advantages, fMRI has been a major tool to study RSNs for a long time, which included a large body of research and a considerable number of findings. For example, Yeo, Krienen et al obtained multiple RSN templates using the fMRI data from over 1,000 participants, which offers compelling references for other studies with smaller sample sizes (Yeo et al., 2011). Because of the extensive and robust findings from this technique, RSN studies using fMRI guide research directions of studies using other techniques to a considerable degree, e.g., their analytical methods and research perspectives.

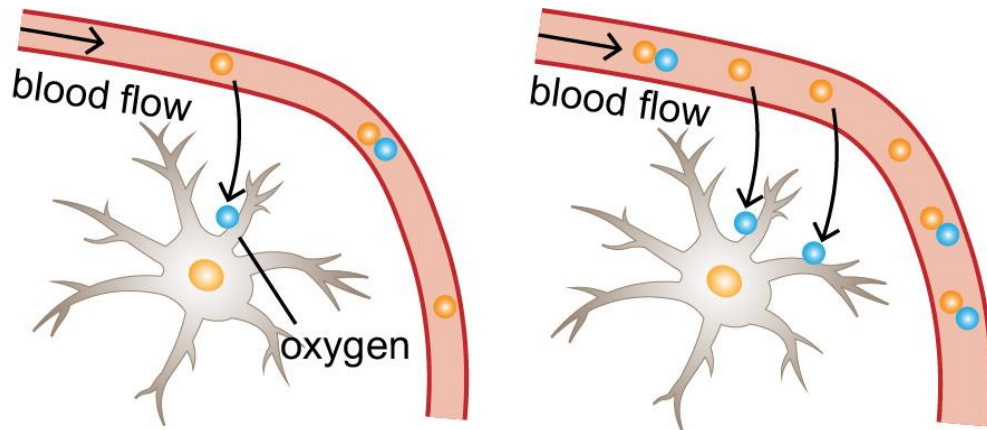


Figure 2.3 Physics of BOLD fMRI

In spite of the advantage and popularity of fMRI, probing RSNs using other techniques is an attractive proposition because it offers new perspective to understand the underpinnings of RSNs, such as the temporal and spectral domains. Moreover, the RSNs analyses using different techniques provides compelling support to the findings from fMRI, which are still under debate to a certain degree networks (Cole et al., 2010; Friston et al., 1996; Mitra et al., 1997). More importantly, the combination of different techniques in RSN studies is of great value to provide a better understanding of the reported characteristics of RSNs.

EEG and MEG are popular non-invasive techniques for mapping brain activities. In contrast to fMRI, EEG and MEG are direct measures neuronal activity (details are in the following section). Their excellent temporal resolution allows examination of neuronal dynamics on the millisecond timescale (Hämäläinen et al., 1993; Laufs et al., 2003b). Over the past decade, EEG/MEG has been increasingly employed by RSN studies (Brookes et al., 2011b; Li et al., 2018; Liu et al., 2017; Yuan et al., 2016). The implementation of these techniques offers new perspectives to characterize RSNs, such as the spectral feature of RSNs.

Although MEG and EEG share the same advantages in terms of temporal resolution and direct measurement, the two techniques have some distinguishing properties. MEG is less sensitive to the volume conduction effect and more sensitive to deep neural sources, while EEG has better sensitivity to tangential sources (Baillet et al., 2001; Hämäläinen et al., 1993). EEG offers lower cost and higher portability, which enables massive application. More importantly, EEG can be recorded simultaneously with fMRI, which can lead to the opportunity to understand the neurophysiological underpinnings of fMRI RSNs (Yuan et al., 2012a).

Despite the advantages of EEG over fMRI and MEG, it should be noted that the three techniques are complementary in characterizing RSNs. Every neuroimaging technique requires considerably more work to obtain efficient and accurate recordings of brain signals, which lays the groundworks for RSN analyses. In this dissertation, EEG is used as the main neuroimaging technique to record resting-state data from participants. An introduction to EEG is provided in the following section.

2.2.2 Introduction to EEG

The human brain has approximately 100 billion nerve cells, called neurons, which transmit and process information through electrochemical signals. Neurons have three basic parts: a cell body, an axon, and dendrites (Figure 2.4A). Each part plays a critical role in neuronal function. The cell body contains the nucleus and produces the energy for the cell. The axon stretches away from the cell body and branches out into multiple axon terminals; it conveys electrical signals along the length of the cell. The dendrites receive signals from other neurons with their branch-like structures (Hämäläinen et al., 1993; Kandel et al., 2000).

When a neuron is excited, the apical dendritic membrane is temporarily depolarized by excitatory postsynaptic potentials (EPSPs), which are generated by the influx of Na^+ or Ca^{2+} from the extracellular space. The potential difference between the cell body and the dendrites leads to intracellular electric current, called the primary current, flow in active neurons (Hämäläinen et al., 1993). Due to the parallel arrangement and orientation of neurons (Figure 2.4B), primary currents from tens of thousands of synchronously activated neurons can be accumulated. The accumulated primary currents are believed to be the primary contributor to EEG signals (Nunez and Silberstein, 2000). Different layers of brain structures, such as the cerebrospinal fluid (CSF), skull, and scalp, are conductive to the electrical signals generated by neurons (van den Broek et al., 1998; Wendel et al., 2008). Therefore, the signals from neurons can be measured by EEG sensors which are placed on the surface of the scalp.

EEG is a non-invasive neuroimaging technique than has been used for over a century. While technology improvements have tremendously advanced this technique, the basic principle remains unchanged: measuring the electrical potentials on the scalp. In EEG measurements, electrodes are placed on the scalp (Figure 2.4C), with the gap between the scalp and the electrodes filled with conductive medium. Locations and names of EEG electrodes have been standardized by the International 10–20 system (Towle et al., 1993) for most clinical and research applications. The number of EEG electrodes varies in different EEG systems, ranging from tens to hundreds. The typical amplitude of EEG signals from human adults is around 10 to 200 microvolts, and an amplifier is required to capture and digitize the signal. By gathering recordings from all electrodes in

an EEG system, EEG data can be obtained to reflect the time-varying electrical potentials over distributed locations on the scalp.

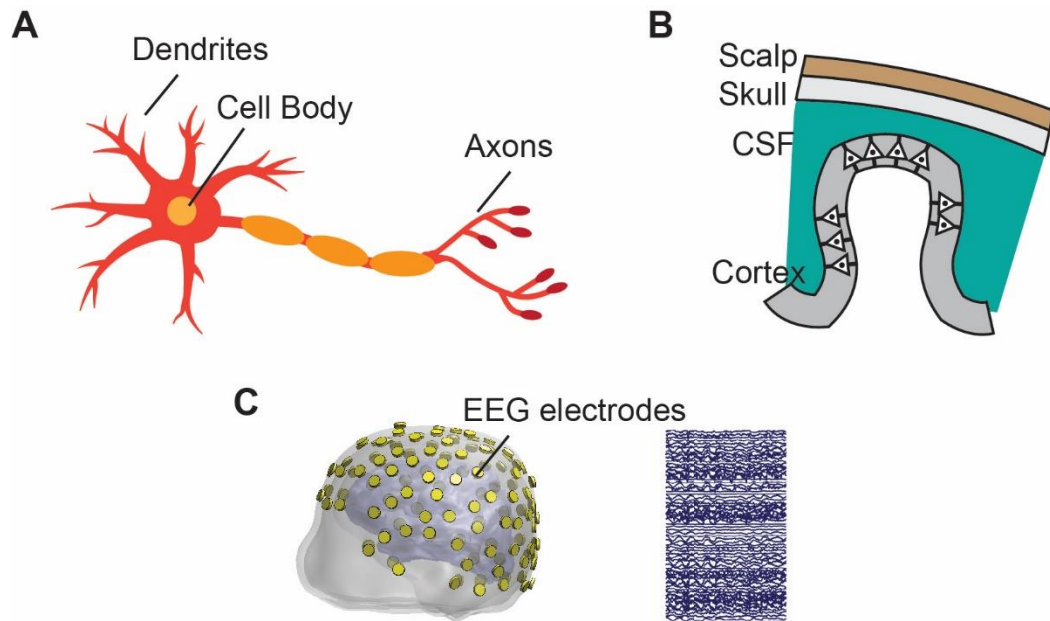


Figure 2.4 Structure of neuron and cortical generator of EEG signals

(A) a typical neuron cell has three parts: the cell body, axons, and dendrites. (B) currents from a large number of synchronously activated neuron cells. (C) Schematic illustration of EEG electrodes and EEG signals

2.2.3 Resting-State EEG

EEG has emerged as a popular technique to record resting-state signals (Li et al., 2018; Li et al., 2017; Liu et al., 2017; Yuan et al., 2016). Compared with task-related experiments, the resting-state EEG recording has similar recording environments. The recording takes place in a shielded room, which is built to block external electromagnetic interference, with a quiet environment, dim light, and normal room temperature. Before the recording, an EEG cap of suitable size is placed on the participant's head, with conductive medium being applied under electrodes. The participant is informed about the experiment in details. Each participant is informed of the experimental protocol. The

resting-state EEG recording begins after all experimenters leave the room and close the door.

During the recording, the participant is asked to keep still in a specific body position (e.g., sitting, standing, and supine) with their eyes open or closed. The participant is not allowed to fall asleep. Experimenters outside the room monitor the behavior of the participant using video cameras and record situations when the participant is not in the resting-state. Periods in which the participant is observed moving are rejected during the data pre-processing. The duration of the resting-state EEG recording varies across different experiments, ranging from several minutes to an hour.

2.2.4 Inverse Source Imaging of EEG

Resting state EEG data represent the time-varying electric potential on the scalp. Without further data processing, any analysis of the data would be confined to the space of the scalp, i.e., the sensor space. Nevertheless, the space of the cortex, i.e., the source space, is desirable for analyses of RSNs because the findings in the source space are directly associated with the anatomical structure of the human brain. Hence, inverse source imaging (ISI) is required to bridge the gap between the sensor space and the source space (Figure 2.5).

There are two important problems in inverse source imaging: the forward problem and the inverse problem. In the forward problem, EEG signals at electrodes are predicted given known cortical sources. In the inverse problem, EEG signals are used to estimate unknown cortical sources. The forward problem can be expressed in the following equation:

$$\Phi = A \cdot S + N$$

2-1

where Φ is a matrix of recorded EEG signals at electrodes each as a function of time, S is the unknown sources defined in the source space, A is the lead field matrix, which represents how the cortical sources contribute to scalp data. and N is the noise. In the forward problem, some key parameters are known, such as the geometry of the head, conductivity of tissues, and locations of sensors, providing significant information for calculating the lead field matrix.

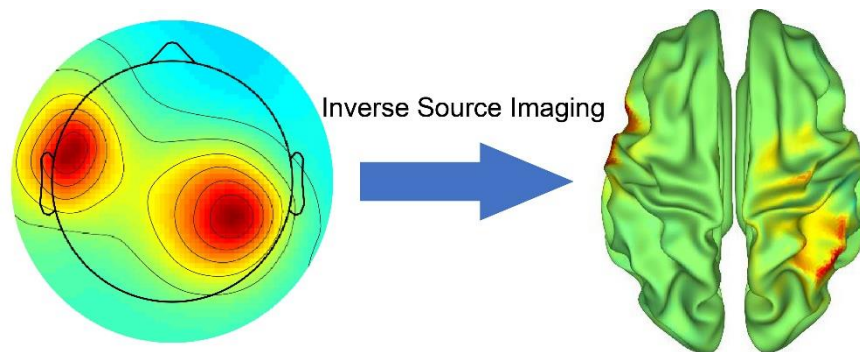


Figure 2.5 Schematic of inverse source imaging
ISI locates the sources from recorded measurements

The inverse problem is the procedure to estimate S using known Φ . Because the number of EEG sensors is far less than the number of cortical sources, the inverse problem is highly underdetermined and there are an infinite number of solutions. Fortunately, this conundrum is addressed with ISI methods, which provide unique solutions to the inverse problem. Different ISI methods have been developed to solve the inverse problem, such as minimum norm estimation (MNE) (Hämäläinen et al., 1993), low resolution brain electromagnetic tomography (LORETA) (Pascual-Marqui et al., 1999), and beamformer (Barnes and Hillebrand, 2003; Van Veen et al., 1997). As an example of ISI methods, a brief description of MNE is provided here. MNE is chosen here not only because it is a popular ISI method, but also because it is employed in the studies of this dissertation. Another advanced ISI method will be introduced in Chapter 5.

In order to obtain the lead field, it is necessary to build the source model. Using structural MRI data, the surfaces of the cortex and other layers of the anatomical structure are segmented into triangles. Each cortical source is placed at the center of a triangle on the cortical mesh and its orientation is perpendicular to the corresponding triangle. The volumes between different layers are assigned different conductivities (Lai et al., 2005). Based on the model and locations of EEG electrodes, the lead field can be calculated using the boundary element method (BEM) (Hamalainen and Sarvas, 1989).

MNE is based on a search for the solution with minimum power and corresponds to Tikhonov regularization.

$$\mathit{min}(\|\Phi - A \cdot S\|^2 + \lambda \cdot \|S\|^2) \quad 2-2$$

where $\|\cdot\|$ indicates the L2-norm and λ is the regularization parameter. Minimization in Eq. 2.3 over Φ yields the MNE estimate of S , i.e., S' , in the following form:

$$S' = T \cdot \Phi \quad 2-3$$

and T is a linear inverse operator to measured signals expressed by

$$T = A^T \cdot (A \cdot A^T + \lambda \cdot I)^{-1} \quad 2-4$$

where I is the identity matrix. The selection of the regularization parameter λ was achieved using the generalized cross validation (GCV) method (Golub et al., 1979; Wahba, 1990). After obtaining the linear inverse operator, the estimated cortical sources can be calculated.

Different ISI methods have been used in recent RSN studies (Brookes et al., 2011b; Hipp et al., 2012; Liu et al., 2017). In this dissertation, MNE is selected as the primary ISI method due to its promising performance in previous research (Yuan et al., 2016). Besides, an advanced ISI method is employed in the study of Chapter 5.

2.3 Methods for Analyzing Resting State EEG

The previous section introduced how to obtain resting-state data in the cortex from EEG, which is only the initial phase of EEG RSN research. In order to analyze RSNs based on the data, computational and analytical methods are required. In previous EEG RSN studies, two types of methods were commonly used: seed-based connectivity analysis (SCA) and independent component analysis (ICA).

2.3.1 Seed-based Connectivity Analysis

The aim of seed-based connectivity analysis (SCA) (Fox et al., 2005) is to investigate the functional connectivity in the human brain, which represents a fundamental aspect of brain physiology and psychology. Over the past two decades, SCA has emerged as a popular method to explore RSNs, regardless of the neuroimaging technique used. To conduct SCA, a particular seed, i.e., a small region of interest (ROI), is selected on the cortex. Then, connectivity is quantified by calculating the correlation between the time course of the seed with every other region within the cortex (Figure 2.6). After the statistical significance is evaluated, regions showing significant connectivity are considered to be functionally connected to the seed (Brookes et al., 2016; Chang and Glover, 2010; Finn et al., 2015).

SCA has two critical aspects: the seed and the connectivity. According to the aim of a study, the seed can be spatially defined as a single voxel, a set of voxels in an enclosed area, or a brain region defined by a brain atlas. Besides, a seed can also be selected based on statistical significance in prior studies. The selection of seeds is challenging because it requires prior knowledge of both anatomical and functional aspects of the human brain. It should be noted that a slight shift of seed location may have a significant impact on the

resultant connectivity (Cole et al., 2010). In terms of connectivity, a variety of metrics have been developed, such as amplitude envelope correlation (AEC), absolute coherence (Coh), and phase lag index (PLI) (Colclough et al., 2016). These metrics evaluate connectivity from different perspectives; their performances also vary (Colclough et al., 2016).

SCA has been used extensively to study RSNs. (Brookes et al., 2011a; Brookes et al., 2011b; Hipp et al., 2012; Siems et al., 2016; Stam et al., 2007). These studies revealed the characteristics of the connectivity in RSNs, which are critical for understanding the functional linkage among networked regions. In addition, SCA has been used to investigate the RSN change caused by different conditions (Cao and Slobounov, 2010; Di Martino et al., 2008; Ku et al., 2014; Zhang et al., 2017).

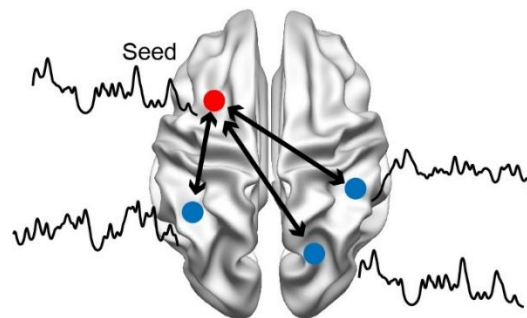


Figure 2.6 Schematic of seed-based connectivity analysis

SCA quantifies the connectivity between the seed node and other nodes on the cortex.

2.3.2 Independent Component Analysis

Another popular method for investigating RSNs is the independent component analysis (Hyvärinen et al., 2004; Hyvärinen and Oja, 2000). ICA was originally developed to solve the cocktail party problem, which separates underlying speech patterns from multiple speakers using recorded data from a few recording devices. The goal of ICA is to find a linear representation of non-Gaussian data from multivariate

statistical data so that the components are statistically independent. In ICA, the observation is assumed to be a linear mixture of independent components (ICs), which can be expressed as:

$$\mathbf{X} = \mathbf{A} \cdot \mathbf{S} \quad 2-5$$

where \mathbf{A} is the mixing matrix. \mathbf{X} is the observed data and \mathbf{S} are independent components. In order to determine \mathbf{A} , a critical principle is that the components in \mathbf{S} are statistically independent, which means each component has no contribution or influence on another component. After obtaining \mathbf{A} , the unmixing procedure can be formulated as

$$\mathbf{S}' = \mathbf{A}^{-1} \cdot \mathbf{X} \quad 2-6$$

ICA has been used extensively for artifact rejection in EEG studies. Recently, ICA has also been used to investigate RSNs given its capability to identify underlying factors (Brookes et al., 2011b; Liu et al., 2017; Sockeel et al., 2016; Yuan et al., 2016). In practice, ICA is usually implemented at the group level in which data from all participants are concatenated into a single matrix (Figure 2.7). Two types of ICA are mostly used in previous EEG-RSN studies: temporal ICA (TICA), where ICs are temporally independent (Brookes et al., 2011b; Yuan et al., 2016), and spatial ICA (SICA), where ICs are spatially independent (Liu et al., 2017; Sockeel et al., 2016). In addition, new types of ICA have been developed for RSNs. For instance, temporal Fourier ICA (TFICA) sought to obtain components that are statistically independent on both the temporal and the spectral domains (Ramkumar et al., 2014).

In contrast to SCA, ICA is data-driven and does not require *a priori* structural knowledge. Additionally, ICA provides a broad view of RSNs over the whole cortex, rather than focusing on a few seed points. From a research point of view, ICA was mainly

used to explore spatial patterns of EEG RSNs. Through ICA, previous studies have successfully derived RSN patterns from EEG data, which showed remarkable similarity to fMRI RSNs.

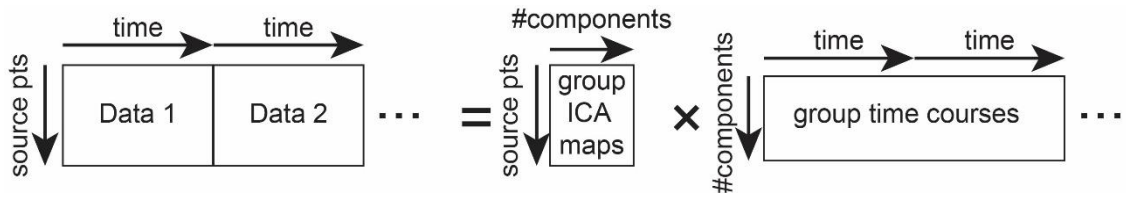


Figure 2.7 Schematic of temporal group-ICA

3 Resting State Networks in the Sensor Space and the Source Space

3.1 Introduction

Over the past decade, a variety of computational frameworks have been developed in order to reconstruct and analyze resting state networks (RSNs) based on MEG/EEG (Brookes et al., 2011b; Hipp et al., 2012; Yuan et al., 2016). Among these proposed frameworks, independent component analysis (ICA) (Hyvärinen and Oja, 2000; Makeig et al., 1996) plays a critical role in the identification of RSNs and has been widely adopted in different studies (Ding et al., 2014; Liu et al., 2017). ICA is used to decompose electrophysiological signals into multiple components that are statistically independent, and RSNs are identified from these components according to their characteristics such as spatial patterns (Brookes et al., 2011b). Previous studies have demonstrated that ICA can be applied to the data either in the sensor space, i.e., the scalp surface (Ding et al., 2014; Jann et al., 2010; Scheeringa et al., 2008), or in the source space, i.e., the cortex (Yuan et al., 2016). Although both options have demonstrated the capability in finding RSNs from EEG/MEG data, few studies have systematically investigated the performance difference between them. Since the major aim of this study is to develop and improve computational frameworks for the reconstruction of EEG RSNs, selecting an optimal space for RSN analysis is an important prerequisite for the establishment of other studies in this dissertation. To eliminate this confusion, a quantitative comparison is carried out to evaluate the performance of the two ICAs in this chapter, aiming to determine which space is more suitable for RSN analysis.

RSNs have been extensively studied using the neuroimaging technique of functional magnetic resonance imaging (fMRI) (Beckmann et al., 2009; Biswal, 2012;

De Luca et al., 2006; Di Martino et al., 2008). Because fMRI measures blood oxygen level-dependent (BOLD) signals from the cortex, RSNs derived using fMRI data RSNs are in the cortex, which can be called as the source space. Recently, novel frameworks to reconstruct RSNs from MEG (Brookes et al., 2011b) and EEG (Yuan et al., 2012b) have also been developed to investigate electrophysiological aspects of RSNs. In these frameworks, the inverse source imaging (ISI) technique (Hamalainen and Ilmoniemi, 1994; Pascual-Marqui, 1999) is an essential step in the process because it can project the sensor-space information such as MEG/EEG signals or topographies into the source space. Due to the function of ISI, the anatomical and structural information of MEG/EEG RSNs can be investigated and evaluated with fMRI RSNs as references.

Depending on the sequence to apply ICA and the ICI technique, the ICA-based frameworks can be split into two categories in the literature: the sensor-space ICA and source-space ICA. In the sensor-space ICA, ICA directly operates on the sensor-space data (Yuan et al., 2010). Following ICA, a specific ISI technique is applied to IC topographies to obtain spatial patterns in the source space. On the other hand, the source-space ICA is performed on source-space data (Yuan et al., 2012b), which are obtained through ISI techniques that are applied on EEG/MEG sensor-space data (Brookes et al., 2011b; Yuan et al., 2012b). Both ICAs have been used to explore RSNs, and meaningful patterns have been successfully found (Brookes et al., 2011b; Yuan et al., 2010; Yuan et al., 2012b). Nonetheless, there has been no comparison of the two ICAs, and little is known regarding the performance differences between them. It is, therefore, of interests to compare the sensor-space and source-space ICAs directly to evaluate their capacity and accuracy in studying RSNs.

The aim of the present study was to investigate the performance of both ICA procedures on the reconstruction of RSNs from EEG data. Simulated data with distributed sources were used and the ICs from both were compared with the ground truth. Their spatial and temporal reconstructions were evaluated through statistical analysis. With real resting-state EEG data obtained from seven healthy participants, their results, in reference to five RSN templates from fMRI data, were also compared to further evaluate the difference between two ICA procedures.

3.2 Materials and Methods

3.2.1 Simulated EEG Data

A head model segmented from a structural magnetic resonance imaging (MRI) dataset by FreeSurfer (<https://surfer.nmr.mgh.harvard.edu/>) was used in the simulation. The sensor positions from the 128-channel EGI EEG system (Eugene, OR) were co-registered to the model by aligning three landmarks, i.e., nasion, left and right preauricular points. Two dimensional (2D) cortical surface was generated by segmenting the white matter/gray matter interface from the same MRI data, and it was triangulated into small triangles, each of which was modeled as a dipole source with its moment perpendicular to the triangle surface. Finally, the forward lead field, which links dipole sources with EEG measurements, was calculated using the boundary element method (BEM) (Hamalainen and Sarvas, 1989).

In order to quantitatively compare the performance of two ICAs, a simulation with 200 iterations was proposed as follows. In each simulation, three distributed sources were generated on the cortical surface (Figure 3.1A). The three sources included three, two, and one cluster(s), respectively. And each cluster encompasses a surface region with the

diameter of ~20 mm without overlap. The envelopes of simulated time courses, which were obtained from experimental resting-state EEG data, were independent of each other. The duration of the envelopes are 5 minutes and the sampling frequency is 250 Hz. To simulate the realistic EEG data, different carrier frequencies were selected for each cluster of each source: 8 Hz, 10 Hz, and 12 Hz for the three clusters of the first source; 9 Hz and 11 Hz for the two clusters of the second source; 15 Hz for the single cluster of the third source. To obtain amplitude-modulated signals, the carrier waveforms were multiplied with the corresponding envelopes to generate six time courses for the six clusters. Then, the simulated time courses were projected to the sensor space using the lead field, and white Gaussian noise was added to simulate the measurement noise, achieving a signal-to-noise ratio at 10 dB. Simulations were repeated 200 times, each time with randomly selected locations for clusters.

3.2.2 Experimental EEG Data

Seven healthy participants (age 41-65) were recruited for the study. This study was approved by Western IRB, and all participants were informed about the protocol of the study and signed a written informed consent form prior to the experiment. A 128-channel EEG system with the BrainAmp amplifier (Brain Products GmbH, Munich, Germany) was used in this study. Resting-state recordings were obtained for five minutes for each participant while they were asked to keep still and have their eyes closed. The electrode at AFz was chosen as the ground electrode, and all electrodes were referenced to FCz. The impedance was kept below 10 K Ω . The sampling frequency for EEG recording was 1000 Hz.

After obtaining resting-state EEG data, data were pre-processed with an established pipeline including rejection of bad segments, interpolation of bad channels, and re-reference to common average. Then data were down-sampled to 250 Hz and band-pass filtered from 4 Hz to 30 Hz. ICA was used to remove artifacts caused by eye and muscle movements and heart noise.

For each participant, structural MRI data were obtained using a 3D MPRAGE sequence (124 contiguous axial slices with 1.2 mm slice thickness; matrix size = 256×256; FOV = 220 mm × 198 mm; TR/TE/TI/TD = 5 /1.98 /725 /1400 ms, flip angle = 8 degree; sampling bandwidth = 31.25 kHz, SENSE acceleration = 2). The head models and the source models were generated using FreeSurfer, and the corresponding lead field was computed as described in the previous section.

3.2.3 Sensor-space ICA and Source-space ICA

Previous studies regarding MEG/EEG RSNs have employed different ISI techniques, such as minimum norm estimation (MNE) (Hamalainen and Ilmoniemi, 1994) and beamformer (Barnes and Hillebrand, 2003), and different ICA techniques, such as Infomax ICA (Lee et al., 1999) and FAST ICA (Nolan et al., 2010), to construct various computational frameworks (Brookes et al., 2011b; Ding et al., 2014). In this study, MNE and Infomax ICA were used in both sensor-space ICA and source-space ICA, aiming to be consistent with the previous works in terms of techniques (Ding et al., 2014; Yuan et al., 2016).

Minimum Norm Estimation: In ISI, the forward model can be expressed as:

$$\Phi = A \cdot S + N \quad \mathbf{3-1}$$

where Φ is a matrix of recorded EEG signals at electrodes each as a function of time, S is the unknown matrix of amplitudes of dipole sources at triangles on CCD each as a function of time, and A is the lead field. N is noise.

A minimum-norm estimate (MNE) (Dale and Sereno, 1993; Hämäläinen and Ilmoniemi, 1984) of dipole amplitudes was obtained by

$$\min(\|\Phi - A \cdot S\|^2 + \lambda \cdot \|S\|^2) \quad \mathbf{3-2}$$

where $\|\cdot\|$ indicates the L2-norm and λ is the regularization parameter. Minimization over Φ yields the MNE estimate of S , i.e., S' , in the following form

$$S' = T \cdot \Phi \quad \mathbf{3-3}$$

and T is a linear inverse operator to measured signals expressed by

$$T = A^T \cdot (A \cdot A^T + \lambda \cdot I)^{-1} \quad \mathbf{3-4}$$

The selection of the regularization parameter λ can be achieved using the generalized cross validation (GCV) method (Golub et al., 1979; Wahba, 1990).

Independent Component Analysis: The Infomax ICA (Lee et al., 1999) from EEGLAB (Delorme and Makeig, 2004) was applied to the data S to obtain independent components (C), as:

$$C = W^{-1} \cdot S \quad \mathbf{3-5}$$

where W is the mixing matrix.

Sensor-Space and Source-Space ICAs: Other than ISI and ICA, the processing of data is built upon previously published research (Ding et al., 2014; Yuan et al., 2016).

In the sensor-space ICA, the Infomax ICA was applied to the envelope of sensor-space data, either simulated or real. Then the mixing matrix was projected into the source space using MNE. In the source-space ICA, EEG data were firstly projected from the sensor space to the source space using the MNE, followed by the Infomax ICA on the

envelope of the source-space data. Fifteen ICs were obtained from simulated data, and twenty-five ICs were obtained from real EEG data. For real data, both ICA procedures were applied on group-level EEG data, which was obtained by the temporal concatenation of normalized data from all participants.

3.2.4 Evaluation of Simulation Results

ICA generated two matrices: the mixing matrix, which contains the spatial information, and the IC matrix, which represents the time courses of each IC. Within the fifteen ICs generated from simulated data, only three are associated with the ground truth. The three components were selected based on their spatial and temporal correlation with the ground truth. The Pearson's correlation coefficients (CCs) between the fifteen spatial maps and the three simulated patterns in the source space were calculated. Similarly, CCs between the fifteen estimated time courses and the three simulated envelopes were also calculated. The absolute values of spatial CCs and temporal CCs were then summed, and the component with the maximal sum was selected as the best match to a simulated source. In order to compare the two ICAs, the difference between the sensor-space and source-space ICAs was then examined by a paired t-test for each simulated source on both spatial and temporal patterns and $p < 0.001$ was selected as the significance level.

3.2.5 Evaluation of Experimental Results

Similar to simulations, twenty-five spatial maps from both ICA procedures were obtained. The CCs between the time course of each IC and time courses of all dipoles in source space were computed to formulate twenty-five EEG RSNs on the cortical surface for both ICA procedures. The spatial maps were converted to z-scores and thresholded with a Z-score of 2.0.

Besides spatial maps, the spectra of ICs were also calculated and analyzed. Since the time courses of ICs only reflected envelopes instead of the original data, real time courses for ICs were obtained by multiplying the ICA un-mixing matrix with original data. After that, short-time Fourier transform (STFT) was applied to data from non-overlapping 1-s window to compute power spectra. In the present study, only power spectra within 4~30 Hz were kept for comparison.

Since the ground truth of real RSNs is unknown, cortical RSN templates constructed mainly from resting-state fMRI data (Yeo et al., 2011) were used as references to evaluate results. Multiple RSNs, including the dorsal attention, visual, sensorimotor, default mode and frontoparietal networks, were selected for further evaluation. Corresponding ICs from two ICA procedures were selected based on the spatial CC to these templates. Moreover, it was observed that some EEG RSNs were lateralized to one hemisphere while the RSN templates were always symmetric on both hemispheres. In such conditions, one EEG RSN with major patterns on the left hemisphere and one with major patterns on the right hemisphere (total two) were selected for one RSN template. The spatial CCs of selected patterns were compared to assess their spatial similarity to the templates.

3.3 Results

3.3.1 Simulation Results

Figure 3.1 shows the reconstruction from one example of the 200 simulations, including the ground truth and the reconstructions from the sensor-space and source-space ICAs. The patterns from the sensor-space ICA (Figure 3.1B) provide similar regions and locations in comparison with the ground truth. Figure 3.1C shows the source-

space patterns from the source-space ICA. For both ICAs, the results all showed great similarity with the ground truth. However, patterns from the source-space ICA seems less widespread than those from the sensor-space ICA. This phenomenon was most obvious in the reconstruction of the third source.

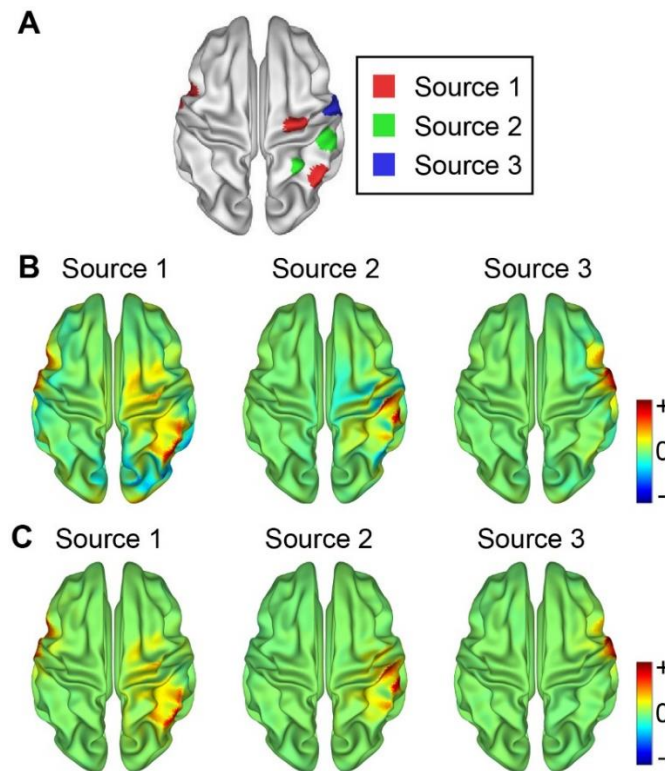


Figure 3.1 An example of simulated sources and the reconstruction from two ICA procedures

(A) Three simulated sources. (B) The reconstruction using the sensor-space ICA. (C) The reconstruction using the source-space ICA.

The summary of spatial and temporal CCs between simulated and reconstructed data from 200 simulations is shown in Figure 3.2. In terms of spatial CCs, the performance of the source-space ICA is significantly better ($p < 0.001$) than the sensor-space ICA in all three sources. Regarding temporal CCs, the source-space ICA also indicates significantly higher similarity ($p < 0.001$) to simulated temporal patterns than the source space ICA in all three sources. However, among the three sources, the performance on the temporal aspect of the source-space ICA decreases from the first source to the third

source. A similar tendency is also observed in the spatial results, but not as obvious as the temporal results. Some extremely low CCs are observed in both spatial and temporal aspects, indicating both ICA procedures failed to reconstruct simulated sources in some simulations.

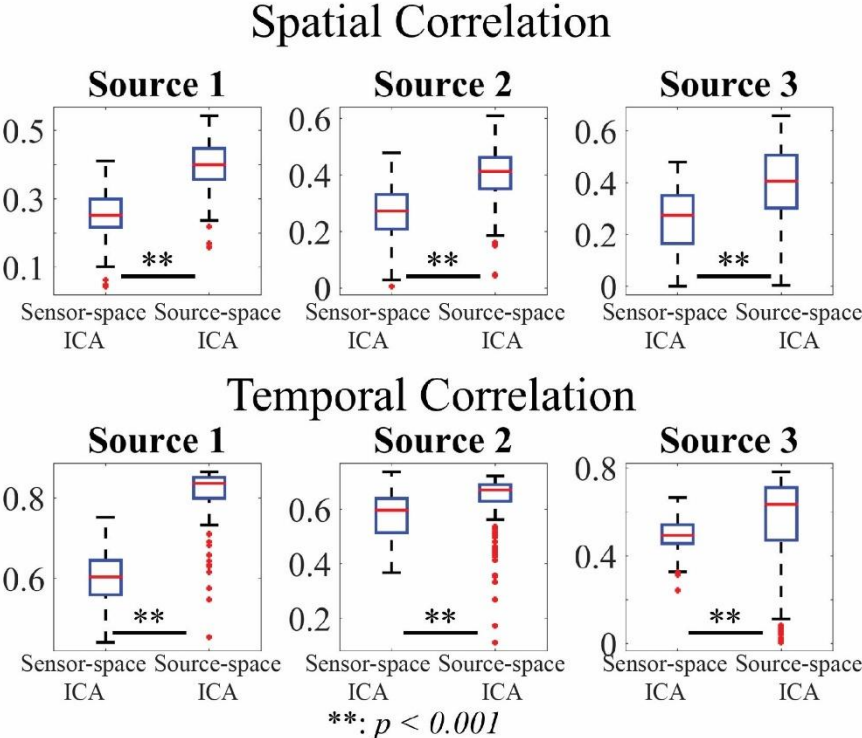


Figure 3.2 Spatial and temporal correlation coefficients of two ICA procedures

3.3.2 Experimental EEG Data

For five selected RSN templates, seven corresponding ICs from either ICA procedure were matched (Figure 3.3). These results were consistent with our previous studies obtained from a different dataset (Ding et al., 2014; Yuan et al., 2016). Both ICA procedures found bilateral network nodes in the parietal cortex for the dorsal attention network, but not the nodes in the frontal cortex. For the sensorimotor network, both ICA methods identified left and right sensorimotor areas but in separate ICs. The default mode network from the source-space ICA consists of nodes from both frontal and occipital

cortices while the sensor-space ICA only detected nodes in the frontal cortex. The frontoparietal network was also reflected in two ICs in both approaches. However, the sensor-space ICA mainly recovered the nodes in the parietal cortex while the source-space ICA revealed the nodes in the frontal cortex. In terms of spectra, evident alpha peaks were detected in all selected ICs. Beta peaks were also observed in many ICs, e.g., IC 13 from the source-space ICA peaked at 20 Hz.

These EEG RSNs exhibited the spatial similarity to the RSN templates from fMRI to a certain degree. In seven IC pairs from both procedures, five ICs from the source-space ICA have higher spatial CCs than those from the sensor-space ICA. Though visual inspections, the source-space ICA seems better in reconstructing distributed brain activations, such as IC 4 and IC 3.

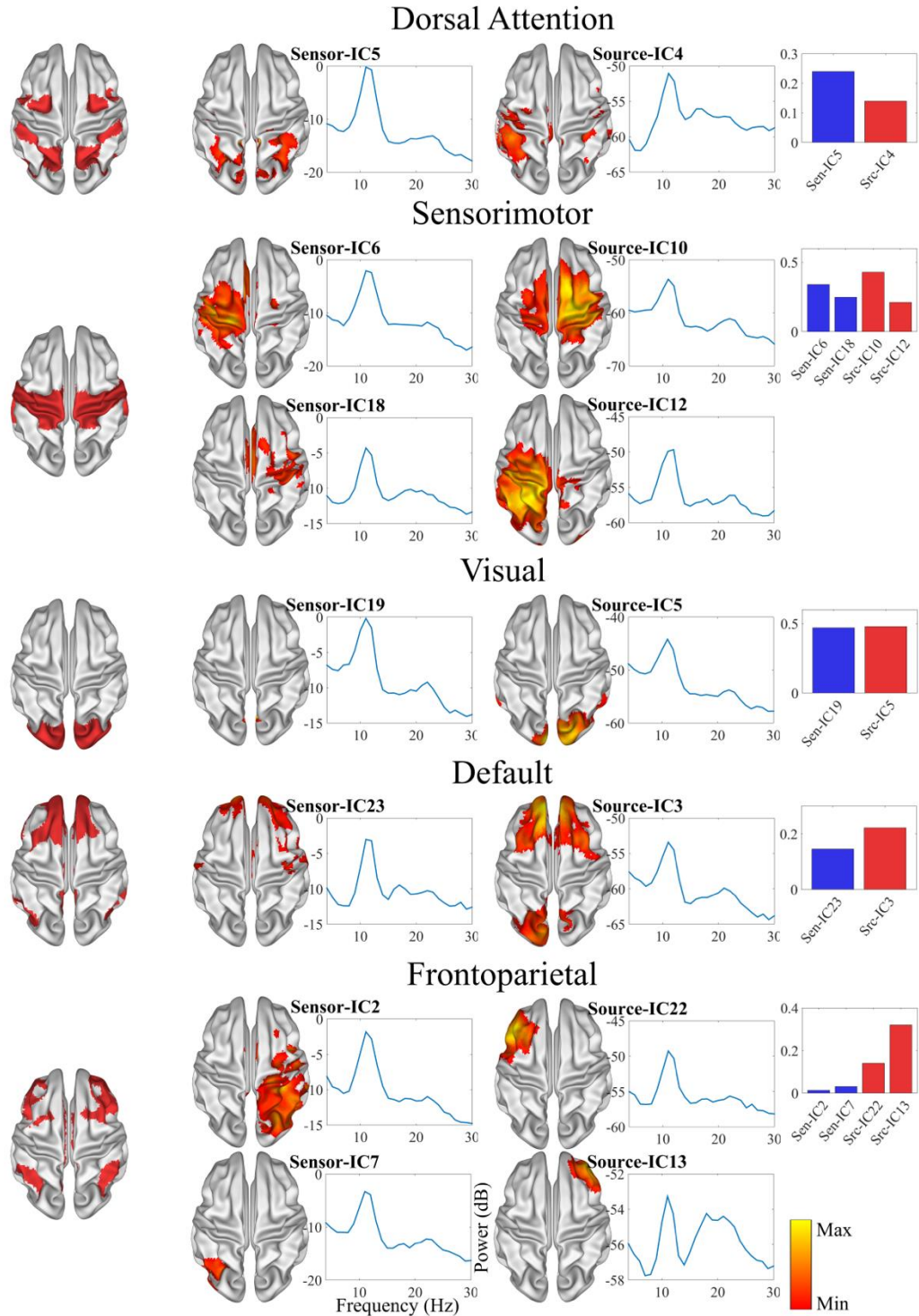


Figure 3.3 Spatial and spectral patterns of RSNs from two ICA procedures
 Left: fMRI RSN templates. Middle: spatial patterns and spectral patterns of RSNs reconstructed by two ICAs. Right: Spatial correlation coefficients between the reconstructed spatial patterns and the templates.

3.4 Discussion and Summary

Due to the advancement in modeling and computation, it has been demonstrated that the reconstruction of various properties of RSNs from EEG is feasible (Yuan et al., 2010; Yuan et al., 2012b). The further research on this topic is extremely significant since EEG can potentially characterize the dynamical and spectral features of RSNs that cannot be achieved by fMRI. Therefore, it is also of significance to further improve the performance of modeling and computation techniques in recovering RSNs from EEG. ICA and ISI techniques have been two important steps in recovering EEG RSNs in literature (Yuan et al., 2012b). In the present study, the performance on deriving RSNs using ICA either before or after ISI was compared and evaluated. The spatial, temporal and spectral patterns of EEG RSNs obtained through two ICA approaches were examined using both simulated and real data.

In the simulation, the source-space ICA achieved significantly better ($p < 0.001$) spatial and temporal feature estimations and slight better spectral estimation. All these results suggest the use of ICA after ISI is more reliable in recovering RSNs. The performance degradation of the source-space ICA from Source 1 to 3, especially in the metric for the temporal pattern, might be due to the difference in signal to noise ratios for three sources since Source 1 has three clusters and potentially generate stronger scalp signals than other two sources.

For real data, spatial patterns from both procedures showed similarity with the RSN templates from fMRI. But these spatial correlations are significantly lower than those from simulations. This might be due to the fact that real resting states are probably more complex than what has been simulated (only three networked activities simulated).

However, it is important to note that RSNs identified from EEG might be intrinsically different from RSNs from fMRI since EEG and fMRI are different signals and reflect different aspects of coordinated brain networks (Brookes et al., 2011b; Yuan et al., 2012b). As an example, neuronal events recorded in EEG are much faster (millisecond or tens of milliseconds) than hemodynamic responses in fMRI (seconds). The symmetric and wide spread fMRI RSNs might be captured due to the averaging effect of the convoluted process from neuronal events to hemodynamic response. As a fact, both sensorimotor and frontoparietal EEG RSNs are recovered in different ICs in the present study. It is further noted that the CCs calculated in real data were in reference to templates, where amplitudes are ignored that can significantly lower down CC values. However, if only ICs from two approaches are being compared, those from the source-space ICA seems relatively better in terms of spatial CC values to fMRI RSN templates and distributive nature of RSNs.

In the present study, only one ICA technique (i.e., Infomax ICA) and one ISI technique (i.e., MNE) were used to conduct the comparison. There are, however, more ICA methods (e.g., FASTICA (Hyvärinen and Oja, 2000)) and more ISI techniques (e.g., eLORETA (Pascual-Marqui, 2007)) that are available to further improve the performance in retrieving EEG RSNs. It is worth investigating them in the future. On the contrary, the present study focuses on the sequence of two data-driven and shows that the source-space ICA outperforms the sensor-space ICA. The findings suggest that the reconstruction of RSNs can be improved by applying ISI before ICA. Therefore, ICA will be used after ISI in the frameworks developed in later studies.

In summary, this study provided a quantitative evaluation of the source-space ICA and the sensor-space ICA. The simulation and experimental results demonstrated the performance differences in RSN reconstruction between two ICAs. The findings of this study narrowed down the optimal framework among two possible options and thus laid the foundation for my following studies. As a result, ICA will be used after ISI in my following studies.

4 Frequency Domain and Statistical Correlation Tomography of Resting State Networks

4.1 Introduction

The study in the previous chapter has compared the sequences in applying ISI and ICA. The results show that applying ICA after ISI can generate RSNs with better accuracies. With this sequence of applying two key algorithms in the framework to reconstruct RSNs being determined, further innovations and developments are to establish new and novel computational frameworks with better performances. In this chapter, a new framework is established based on the framework introduced in the previous chapter. Following the results from the previous Chapter, the new framework implemented the step of ICA after the step of ISI. Moreover, the new framework introduced new analytical methods, aiming to address multiple limitations of the conventional frameworks and to achieve more efficient analyses beyond previous frameworks.

Among various methods probing resting-state brain signals, independent component analysis (ICA) has been widely used to identify RSNs from both EEG/MEG and fMRI data. To achieve better computational accuracy of ICA, the sample domain has been taken in one large dimension (Hyvärinen et al., 2004). In particular, spatial ICA is often used on fMRI data (Beckmann et al., 2009; Calhoun et al., 2009) because the spatial dimension of fMRI data is relatively larger than its temporal dimension. Temporal ICA is widely performed on EEG/MEG data (Brookes et al., 2011b; Yuan et al., 2016) because of their relatively large temporal dimensions. In efforts to spatially define RSNs on the cortical surface from EEG/MEG, i.e., the same domain of fMRI RSNs, ICA has been

used in combination with EEG/MEG inverse source imaging (ISI) techniques (Grech et al., 2008; Mosher et al., 1999; Pascual-Marqui, 1999; Yuan et al., 2016). Resting state EEG/MEG data are subject to the inverse reconstruction of underlying sources on the cortical surface. Resulted cortical source data are analyzed by ICA to reconstruct a network-level organization of activities. It is noted that these techniques make it feasible to directly compare fMRI RSNs and EEG/MEG RSNs in a common spatial domain, providing new insights to the electrophysiological basis and hemodynamic aspects of RSNs, especially when fMRI and EEG data can be simultaneously recorded (Goldman et al., 2002; Goncalves et al., 2006; Yuan et al., 2016).

Despite these new advancements, methods to derive EEG/MEG RSNs are still limited in many ways. First, the mathematical principle of ICA favors the detection of non-Gaussian distributed components, making it a very successful tool in finding artifacts rather than components related to brain activity (Hyvärinen and Oja, 2000; Vigário et al., 2000), which is certainly not optimized for separating networks of organized neural activity. Second, spatial patterns defined with linear mixing weights of ICA for independent components (ICs) have been shown less optimal than those obtained through an extra correlation analysis between source time series and IC time series (Brookes et al., 2011b; Yuan et al., 2016). Third, ICA mixing weights are lack of statistical meanings to be systematically assessed in defining the spatial coverage of an RSN. Fourth, most brain activity is rhythmic in nature, and spectral characteristics of individual RSNs have been assumed *a priori* using pre-selected band-pass filters (Brookes et al., 2011b; Mantini et al., 2007). However, such a strategy is not always optimal and could introduce bias, especially when an RSN has a wide power spectral pattern and various power spectra

among different individuals. Finally, in group analysis with multiple individuals, inter-individual variance exists in resting state analysis (Goncalves et al., 2006), but it has not been addressed when data from all individuals are just simply concatenated to be analyzed by the ICA routine.

In the present study, a new framework termed as time-frequency ICA-based statistical correlation tomography (TFICA-SCT) is proposed to identify RSNs from EEG data by combining ISI, a unique time-frequency ICA method, and statistical correlation analysis. ISI was performed on complex EEG data after a short-time Fourier transform (STFT) to reconstruct cortical source maps. Instead of conventional temporal ICA (TICA), TFICA was implemented by applying an ICA algorithm on the time-frequency representation of cortical source data from ISI. The correlation analysis between IC time series and source time series from ISI was further used to obtain optimal spatial patterns of RSNs. A series of steps were further developed and conducted to reconstruct genuine tomography of RSNs, which included processes to address inter-individual variance, conversion to a statistical metric using the Fisher's z-transform, correction of false cross-correlation from autocorrelation, and thresholding by a cluster-based statistical approach.

The present study examined the performance of TFICA-SCT using three sets of experimental data from both healthy and symptomatic participants. Derived tomographic maps were compared with templates from resting-state fMRI to evaluate their consistency with RSN definitions from an independent neuroimaging modality. The robustness of the method in identifying RSNs in both spatial and spectral patterns was evaluated by comparing results obtained from three datasets. In each data set, there were two conditions (i.e., eyes-open vs. eyes-closed; healthy persons vs. patients; and before vs.

after treatment) and their comparisons were used to examine the resolution and capability of the proposed framework in identifying condition-specific differences.

4.2 Materials and Methods

4.2.1 Cortical Statistical Correlation Tomography of RSNs

Forward models and lead field computation: The cortical current density (CCD) source model (Dale and Sereno, 1993) was used in the present study, in which the source space was represented numerically by continuously distributed triangular elements over the cortical surface (Figure 4.1). The anatomical cortical model of each participant was obtained by segmenting the white matter/gray matter interface from the participant's head magnetic resonance imaging (MRI) using FreeSurfer (Fischl, 2012). The cortical surface was triangulated into a high-resolution mesh of 40,960 triangles (Figure 4.1). Each dipole source was placed at the center of a triangle on the cortical mesh, and its orientation was perpendicular to the corresponding triangle. Boundary element (BE) volume conductor models were used to represent the realistic geometrical shape of the human head and major conductivity profile (e.g., the scalp, skull, and brain) for the forward problem calculation. The BE models have 10,240 triangles in each of three surface meshes, which were obtained by segmenting the surfaces of the scalp, skull, and brain from structural MRI and were assigned different conductivities (0.33/ Ωm , 0.0165/ Ωm , and 0.33/ Ωm , respectively) (Lai et al., 2005). Co-registration of BE models and electrodes was implemented by aligning three landmarks, i.e., nasion, left and right pre-auricular points.

The forward model can be expressed in the following equation:

$$\Phi = A \cdot S + N \quad 4-1$$

where Φ is a matrix of recorded EEG signals at electrodes each as a function of time, S is the unknown matrix of amplitudes of dipole sources at triangles on CCD each as a function of time, and A is the lead field matrix linking dipole sources with EEG recordings, which was calculated using the boundary element method (BEM) (Hamalainen and Sarvas, 1989) based on the defined source model, volume conductor model, and co-registered EEG electrode locations. N is noise.

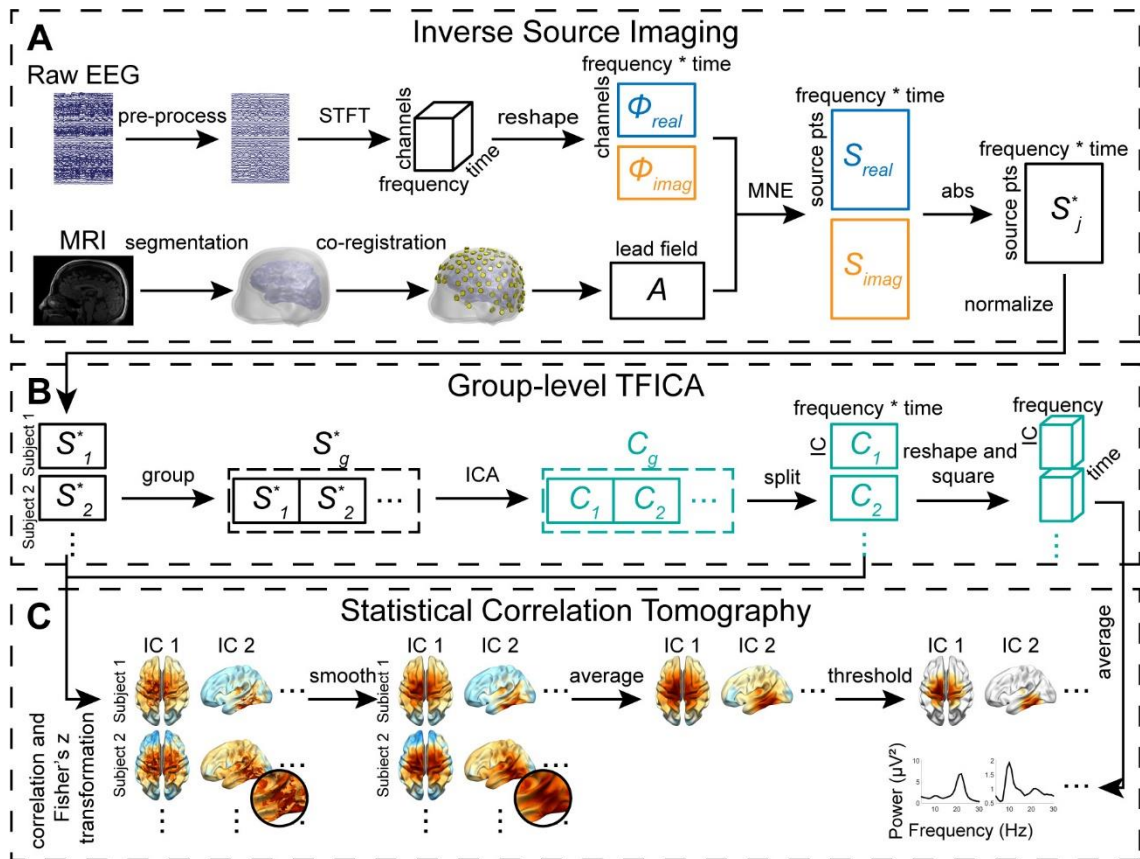


Figure 4.1 Diagram of TFICA-SCT

(A) Inverse source imaging, including EEG preprocessing, STFT, volume conduction modeling, BEM forward calculation of lead field, and MNE inverse solution. (B) Group-level TFICA on the cortical source domain. (C) Statistical correlation tomography derived by correlational analysis of time courses between ICs and sources. (Figure as originally published in Li, Yuan, Shou, Cha, Sunderam, Besio and Ding (2018). Front. Neurosci. 30 May 2018. doi: 10.3389/fnins.2018.00365)

Inverse Source Imaging: ISI was performed in the complex domain of recorded EEG data to prepare inverse source data for the analysis by TFICA. The short-time

Fourier transform (STFT) was applied on non-overlapping 1-second epoch EEG data, resulting in a 3D time-frequency representation (TFR) of EEG data, i.e., channel, frequency, and time (or epoch). Twenty-seven frequency bins from 4 to 30 Hz were kept with a resolution of 1 Hz. The 3D TFR was then reshaped into a 2D matrix by concatenating the dimensions for frequency and epoch.

Since STFT is a linear transformation, it does not change the relationship between dipole sources and EEG recordings in Eq. (1), while it leads to two values, i.e., real and imagery parts, for each measurement at an electrode. Therefore, Eq. (1) was re-arranged as:

$$\begin{bmatrix} \Phi_{real} \\ \Phi_{imag} \end{bmatrix} = \begin{bmatrix} A & 0 \\ 0 & A \end{bmatrix} \cdot \begin{bmatrix} S_{real} \\ S_{imag} \end{bmatrix} + \begin{bmatrix} N_{real} \\ N_{imag} \end{bmatrix} \quad 4-2$$

The lead field matrix is the same for both real and imaginary parts. Φ and S were redefined as $\Phi = \begin{bmatrix} \Phi_{real} \\ \Phi_{imag} \end{bmatrix}$ and $S = \begin{bmatrix} S_{real} \\ S_{imag} \end{bmatrix}$. Since the number of discrete sources was larger than the number of measurements (i.e., the number of electrodes), regularized solutions were needed to produce stable results (Michel et al., 2004). In the present study, a minimum-norm estimate (MNE) (Dale and Sereno, 1993; Hämäläinen and Ilmoniemi, 1984) of dipole amplitudes in the sense of L2-norm at each time-frequency point was obtained by

$$\min(\|\Phi - A \cdot S\|^2 + \lambda \cdot \|S\|^2) \quad 4-3$$

where $\|\cdot\|$ indicates the L2-norm and λ is the regularization parameter. Minimization in Eq. (3) over Φ yields the MNE estimate of S , i.e., S' , in the following form

$$S' = T \cdot \Phi \quad 4-4$$

And T is a linear inverse operator to measured signals expressed by

$$T = A^T \cdot (A \cdot A^T + \lambda \cdot I)^{-1} \quad 4-5$$

The selection of the regularization parameter λ was achieved using the generalized cross validation (GCV) method (Golub et al., 1979; Wahba, 1990).

Group-level TFICA: After obtaining source data from all subjects, ICA analysis was carried out at the group level. First, amplitudes of source data at individual time points were obtained as absolute values of complex time courses. Then, data from individuals were normalized using a z-transform to reduce inter-individual variations, yielding normalized source amplitude data, i.e., S^* . Afterward, individual source data from a group of participants were concatenated in the tempo-spectral domain, leading to a group-level 2D source matrix S_g^* (channels X (participants, epochs, frequency bins)), in which the subscript g indicates the group-level matrix. The Infomax ICA (Lee et al., 1999) from EEGLAB (Delorme and Makeig, 2004) was applied on S_g^* to obtain group-level independent components (C_g), each representing a cortical map of brain activities involving multiple regions (nodes) mutually dependent and forming a network, as:

$$C_g = W^{-1} \cdot S_g^* \quad 4-6$$

where W is the mixing matrix. The number of underlying sources had been suggested to be around 30 (Abou - Elseoud et al., 2010; Ramkumar et al., 2014; Smith et al., 2009). A relatively larger number of ICs (i.e., 40) was pre-selected in the present study. Each column in C_g represents the linear mixing weights from all dipole source points (i.e., 40,960), and each row represents concatenated time-frequency courses from all participants for the corresponding IC.

Statistical Correlation Tomography: To define spatial patterns of each IC on the cortical surface, columns of C_g were first segmented to form the C_i matrix for each

participant, as in Eq. (8). Correlation coefficients (CCs) between the time-frequency course of each IC (i.e., each row of C_i) and the time-frequency course of each source on the CCD model (i.e., each row of S_i^*) were calculated for all individual participants in the group, as in Eq. (9). CC values were converted into z-values using the Fisher's z-transformation (Fisher, 1915) according to Eq. (10).

$$C_g = [C_1, C_2, \dots, C_i, \dots, C_N],$$

$$i = 1, \dots, N \text{ and } N = \text{number of participants} \quad \mathbf{4-7}$$

$$CC_i(j, k) = \text{corr}(C_i(j), S_i^*(k)),$$

$$j = 1, \dots, 40; k = 1, \dots, 40,960 \quad \mathbf{4-8}$$

$$z_i(j, k) = \frac{1}{2} \ln \left(\frac{1 + CC_i(j, k)}{1 - CC_i(j, k)} \right),$$

$$j = 1, \dots, 40; k = 1, \dots, 40,960 \quad \mathbf{4-9}$$

All correlation maps were then smoothed by an iterative smoothing algorithm, i.e., the heat kernel smoothing with Full Width at Half Maximum of 8 mm (Chung et al., 2005), which has been widely used in fMRI (Chung et al., 2010; Hagler et al., 2006). It is known that cross correlations calculated in Eq. (9) are impacted by autocorrelations in either $C_i(j)$ or $S_i^*(k)$ signals (Friston et al., 1994). Therefore, autocorrelations of $C_i(j)$ and $S_i^*(k)$ were computed to correct z-values in Eq. (10) via adjusting the degree of freedom (DOF) according to the Bartlett's theory (Bartlett, 1935):

$$N'_i(j, k) = N_i(j, k) \cdot \frac{1 - \rho_C(j, k) \cdot \rho_S(j, k)}{1 + \rho_C(j, k) \cdot \rho_S(j, k)} \quad \mathbf{4-10}$$

$i = 1, \dots, P$ and $P = \text{number of participants}$

where the ρ_C and ρ_S are the autocorrelation coefficients of C_i and S_i^* , respectively. Thus, the square root of the theoretical variance of $z_i(j,k)$ is $1/\sqrt{N'_i(j,k) - 3}$. By dividing it, z-values were converted into z-scores (that is, zero mean, unit variance, Gaussian distributions under the null hypothesis of no correlation) (Vincent et al., 2007) for each IC, the group-level z-score maps were calculated using an approach that had been suggested more effective on relatively small samples (Alexander, 1990; Silver and Dunlap, 1987).

Cluster-based statistical thresholding: To quantitatively define brain regions that belong to an RSN (i.e., an IC), statistical correlation coefficient (SCC) maps obtained after Eq. (12) need to be thresholded. This was done by applying a t-test against zero on z-scores from all participants in a group at each source on the CCD model. The threshold was set at $p < 0.01$ to create a binary mask with 1 for locations of significant correlations. To address the multiple comparisons problem, a cluster-based correction method was employed (Hagler et al., 2006). Specifically, in a Monte Carlo simulation, random brain signals were generated on the CCD model and then the steps starting from Eq. (9) to Eq. (11) were followed to create pseudo-SCC maps thresholded at $p < 0.01$ as in real data. The process was repeated for 1,000 repetitions to create a histogram for the size of clusters (connected areas on the CCD mesh) under the null hypothesis. From the histogram, the threshold of cluster size for real data was identified at $p < 0.01$ and used to remove small clusters to reduce false positives (i.e., removing clusters on binary masks smaller than the threshold). The same procedure was performed on all ICs to create SCT for each RSN.

4.2.2 Experimental Protocols

To evaluate the performance of the proposed TFICA-SCT, systematic evaluations were conducted in three sets of experimental datasets acquired from both healthy individuals and individuals with a balance disorder called mal de débarquement syndrome (MdDS), which is described below. The datasets included 1) resting EEG in seven healthy individuals in eyes-closed (EC) and eyes-open (EO) conditions, termed as the EC/EO dataset; 2) resting EEG in seven healthy controls (HC) and seven individuals with MdDS termed as the HC/MdDS dataset; and 3) resting EEG in seven MdDS individuals before and after receiving treatment of repetitive transcranial magnetic stimulation (rTMS), termed as the Pre-/Post-rTMS dataset. The study protocol and acquisition settings of these experimental data have been detailed in our prior work (Ding et al., 2014; Yuan et al., 2017) and they are briefly described below.

Participants: Written informed consent was obtained from all participants before the study. All study procedures were approved by the Western Institutional Review Board (www.wirb.com). To examine the proposed tomography, the present study included data from seven healthy controls (all females; age: 51.1+/-8.0 years) and seven patients (all females; age: 53.1+/-12.1 years) with MdDS (Cha, 2009; Ding et al., 2014). The recruitment of participants of MdDS did not exclude male participants, but the prevalence of females is much higher than males in MdDS (Cha, 2009). Thus, the matched healthy control population only included female participants as well.

MdDS is caused by exposure to oscillating environments such as a flight or a cruise, leading to a persistent sensation of rocking dizziness (Cha, 2009; Cha et al., 2012; Cha et al., 2013; Cha, 2015). It is the unnatural persistence of the natural phenomenon of

motion entrainment. rTMS treatment had been demonstrated with therapeutic effects in MdDS (Cha et al., 2013; Cha et al., 2016a; Cha et al., 2016b; Ding et al., 2014). All MdDS patients in the present study received five consecutive days with one session on each day. The rTMS target in all patients was the dorsolateral prefrontal cortex (DLPFC), which was located by the Localite TMS Navigator (Localite GmbH, Germany) frameless stereotaxy system. The Magventure MagPro X100 stimulator (MagVenture A/S, Farum, Denmark) was used to generate magnetic stimulation pulses including 1 Hz right DLPFC stimulation of 1200 pulses followed by 10 Hz left DLPFC of 2000 pulses. The treatment effects were evaluated using a clinical visual analogue scale (VAS) (Cha et al., 2013; Shou et al., 2014; Yuan et al., 2017).

EEG recording: A BrainAmp amplifier (Brain Products GmbH, Munich, Germany) was used to record resting-state EEG signals from 126 channels at a sampling frequency of 1000Hz. The ground electrode was placed at AFz and FZ was chosen as the recording reference channel. Participants were recorded while lying quietly with eyes closed. Participants in the HC group performed two 5-min sessions of simultaneous fMRI-EEG recordings with their eyes open and closed, respectively. It should be noted that only EEG data were analyzed in the present study. Participants with MdDS underwent two 5-min sessions of EEG, one before the first TMS session (Pre-TMS) on the first day and the other 4 to 5 hours after the last TMS on the 5th day (Post-TMS). Since the effect of rTMS on MdDS patients has been investigated in our previous study (Ding et al., 2014), the inclusion of EEG data from MdDS patients before and after rTMS in the present study served as a contrast to examine the sensitivity of the proposed approach.

MRI: Structural magnetic resonance images of participants' heads were obtained using a General Electric Discovery MR750 whole-body 3-Tesla MRI scanner (GE Healthcare, Milwaukee, Wisconsin) through a T1-weighted magnetization-prepared rapid gradient echo (3D MPRAGE) sequence. The parameters for imaging were: FOV = 240 mm, axial slices per slab = 190, slice thickness = 0.9 mm, image matrix = 256×256, TR/TE = 5/2.012 millisecond, acceleration factor R = 2, flip angle = 8°, inversion time TI = 725 ms, sampling band-width = 31.2 kHz.

4.2.3 Data Analysis Protocols

Preprocessing of EEG: EEG data from each participant was preprocessed with the following pipeline. First, a band-pass filter of 0.5 to 100 Hz and a notch filter of 60 Hz was used on EEG data. Second, bad channels were detected using the FASTER toolbox (Nolan et al., 2010) with visual inspection as a supplemental check, followed by interpolation from neighboring channels using EEGLAB (Delorme and Makeig, 2004). Third, EEG data were divided into non-overlapping 1-sec epochs (same as those being analyzed using STFT in section of “*Inverse Source Imaging*”). Bad epochs were rejected using the FASTER toolbox. During detections of bad channels and bad epochs, a threshold at z-score > 3 was selected. Fourth, the Infomax ICA (Lee et al., 1999) was utilized to decompose time-domain EEG data concatenated from all epochs into 64 ICs. Basing on visual inspection of spatial and spectral features of all ICs, ICs linked to ocular, cardiac and muscular activities were removed. Finally, denoised EEG data were re-referenced to a common average and down-sampled to 250 Hz. For EEG data collected with fMRI, the same framework of preprocessing was employed as in our previous studies (Yuan et al., 2016; Yuan et al., 2012a), and an additional notch filter of 26 Hz was

used to reject vibration noise from the MRI system (Mayeli et al., 2016; Ritter and Villringer, 2006).

Analysis by TFICA-SCT: To directly compare tomography from different conditions, the TFICA step in the proposed framework was performed on combined EEG data from the two compared conditions for each group: eyes open vs. eyes closed in HC, HC vs. MdDS, and pre-TMS vs. post-TMS in MdDS. Three SCT analyses were performed on grouped data of participants in both conditions included, and averaged SCTs of ICs were obtained.

Spectral Powers of ICs: Spectral powers of all ICs were calculated in each participant by reshaping the 2D matrix C_g into a 3D matrix (channel×frequency×epoch), squaring all values, and averaging over epochs. These steps resulted in 40 power spectra for 40 ICs at 27 frequency bins ranging from 4 Hz to 30 Hz.

Selection of ICs: Brain activity-related ICs were selected from all 40 ICs based on their spatial-spectral features. Specifically, the corresponding SCTs of ICs were compared with RSNs defined from resting-state fMRI data (Yeo et al., 2011). Based on the anatomic locations of fMRI RSNs, EEG RSNs were identified mainly for visual, auditory, somatomotor, frontoparietal, and default mode networks. In the spectral domain, theta, alpha, and beta peaks were analyzed with reference to spectral features of RSNs (Mantini et al., 2007) and/or the general 1/f spectra (Freeman et al., 2000; Robinson et al., 2001) were treated as reasonable patterns, while spectral patterns of sharp and narrow peaks and over-oscillations were used in rejecting ICs as artifacts.

4.2.4 Evaluation and Validation Protocols

We conducted a series of validation steps on the performance of the TFICA-SCT method. First, RSNs defined through TFICA-SCT were compared with RSN templates derived from fMRI data (Yeo et al., 2011). Second, the SCTs from the three analyses were compared quantitatively to assess the spatial consistency of the obtained results. Third, SCTs from different conditions (i.e., EC vs. EO in the healthy, HC vs. MdDS group, Pre-rTMS vs. Post-rTMS in MdDS) were compared statistically in terms of both spatial and spectral patterns. Details are described below.

Comparisons with fMRI RSN Templates: To evaluate spatial patterns of obtained EEG RSNs, cortical maps from TFICA-SCT were compared with the five RSN templates from fMRI (Yeo et al., 2011) including visual, auditory, somatomotor, frontoparietal, and default mode networks. For each binary fMRI template and each SCT, the comparison was quantified by a template-matching method (Greicius et al., 2007) with normalization as follows:

$$TD(t, c) = \frac{Z_{in}(t, c) - Z_{out}(t, c)}{Z_{in}(t, c) + Z_{out}(t, c)} \quad \mathbf{4-11}$$

where TD is the template-matching degree; t is the index for the binary template and c is the index of the thresholded SCT. Z_{in} is the averaged z-score from source points on SCT inside the fMRI template and Z_{out} is the averaged z-score from source points outside. TD s were calculated for all possible pairs between selected RSNs and the five templates. The significance of TD was evaluated by a Monte Carlo simulation. Specifically, for a template-SCT pair, the z-scores on each source point were randomly shuffled 500,000 times and the corresponding TD s were computed, generating a histogram of TD s. Based on the histogram, the p value was obtained for each pair and the significance level was

0.01, with Bonferroni correction. Positive *TDs* confirmed the spatial similarity between templates and SCTs. To investigate possible confusion in matching templates and SCTs, positive *TDs* within- and between-class were compared using t-tests across five networks and three analyses.

Evaluation of Spatial Consistency in Multiple Datasets: To evaluate spatial pattern consistency of EEG RSNs obtained from multiple datasets, the spatial patterns of SCTs obtained from the three analyses (i.e., EC vs. EO in the healthy, HC vs. MdDS, Pre-rTMS vs. Post-rTMS in MdDS) were quantitatively compared in pairs using the metric of TD as follows,

$$\overline{TD}(i, j) = \frac{TD(i, j) + TD(j, i)}{2} \quad \mathbf{4-12}$$

where in $TD(i, j)$ the thresholded SCT i from one analysis was binarized and used as the template to calculate TD against the thresholded SCT j from another analysis. The same analysis was repeated after two SCTs were shifted where the thresholded SCT j was binarized. The TD between the SCTs i and j were taken as the average of two analyses, resulting in a TD map for all possible pairs. Since the SCTs were separated into five classes of RSNs, there were twenty-five large tiles in a TD map, each containing TD data for RSN-RSN pairs in one class. In the matrix representation of TD maps (see Figure 4.6 for an example), the diagonal tiles represented within-class TDs while off-diagonal tiles contained cross-class TDs. As in the above section, positive TDs within- and between-class were compared using a t-test.

Difference in Statistical Correlation Tomography: To probe differences between two conditions in each dataset, the SCTs for data from two conditions were re-calculated separately (Eqs. (8) -(12)) based on the group-level TFICA results and then statistically

compared. In each dataset for each RSN (defined by an IC), regions with significant differences were detected by applying a two-tailed t-test at each source point between two SCTs within binary masks defined in the section “*Cluster-based statistical thresholding*”. The resulted clusters of difference on the CCD model were subject to the same cluster-based correction method to control for false positives. For visualization, identified clusters of difference on the CCD model from two compared conditions were displayed as the difference of SCC values between two SCTs.

Power Spectra Difference: Power spectra of individual ICs were used as the second metric to evaluate the difference between two compared conditions. At each individual subject and for each selected IC, a two-tailed t-test was used to compare specific band power at theta, alpha or beta bands between conditions over all epochs, determining whether there were significant differences between two conditions and in the direction of difference (i.e., increase or decrease). The analysis was only performed on two datasets (i.e., EC vs. EO in the healthy controls and pre-rTMS vs. post-rTMS in MdDS) since the third dataset (i.e., HC vs. MdDS) involved different subject groups precluding the direct statistical comparison. Significant increase/decrease was collected from all subjects for each IC at each frequency band and aggregated for each class of RSNs, yielding data for five RSNs and three frequency bands (Figure 4.2). For each RSN class at each band, the number of increase/decrease was tested against the number of total significant changes at the group level using a binomial test (hypothetical probability of increase/decrease = 0.5).

4.3 Results

4.3.1 Spatial and Spectral Patterns of RSNs

Figure 4.2-4.4 illustrate spatial and spectral patterns of identified RSNs from three datasets (i.e., the EC/EO, HC/MdDS, Pre/Post-rTMS datasets), which were further categorized into five groups, i.e., visual (V), auditory (A), somatomotor (M), frontoparietal (F), and default mode (DMN) networks, based on criteria described above (see the section “**Evaluation and Validation Protocols**”). These five groups of RSNs were detected from all three datasets with high spatial and spectral similarities, while some condition-dependent variations were also observed.

In each RSN group, more than one EEG network was obtained by TFICA-SCT with significant spatial resemblance identified, each of which was termed as a subnetwork of the group. For the visual network, 4, 5, and 4 subnetworks were detected in EC/EO, HC/MdDS and Pre-/ Post-rTMS, respectively (Figure 4.2-4.4). They were generally associated with the primary visual cortex (i.e., V-d in EC/EO, V-e in HC/MdDS, and V-b in Pre-/Post-rTMS), middle temporal visual area (i.e., V-a and V-b in EC/EO, V-b and V-d in HC/MdDS), V2/V3 (i.e., V-c and V-d in Pre-/Post-rTMS), and parts of the ventral stream of visual systems (other subnetworks in Figure 4.2-4.4) (Goodale and Milner, 1992). Some of these subnetworks had bilateral symmetric distribution (e.g., V-d in Figure 4.2, V-e in Figure 4.3, V-c in Figure 4.4). Some showed the hemispheric dominance whereas the similar dominance was found on their symmetric hemisphere in other corresponding subnetworks (i.e., V-a and V-b in Figure 4.2, V-a and V-c in Figure 4.3, V-b and V-d in Figure 4.4). In terms of spectral patterns, the visual RSNs were characterized with an evident peak in the alpha band.

For the auditory network, 4, 3 and 3 RSNs were detected in three datasets, respectively (Figure 4.2-4.4). These RSNs mainly covered the temporal cortex, with either lateralized distribution (i.e., A-a, A-b, and A-d in EC/EO, and A-a and A-b in Pre-/Post-rTMS) or bilateral distribution (i.e., all in HC/MdDS and A-c in Pre-/Post-rTMS). Some were symmetric in their spatial patterns (e.g., A-a and A-b vs. A-c and A-d in EC/EO). Note that the bilateral symmetric subnetworks in HC/MdDS had opposite correlation values in the two hemispheres (A-a and A-b in HC/MdDS). Most RSNs had peaks in the alpha band while some showed additional peaks in the beta band.

For the somatomotor network (Figure 4.2-4.4), 2, 4 and 3 subnetworks were detected in three datasets, respectively. Two subnetworks in EC/EO covered the premotor and primary motor cortices. Four subnetworks in HC/MdDS covered different areas, i.e., M-b over the primary motor and premotor cortices, M-c over the somatosensory cortex, and M-a and M-d over the lateral primary motor cortices. The subnetworks in Pre/Post-rTMS had similar patterns compared to the subnetworks in HC/MdDS. Most of these subnetworks showed lateralized distributions (e.g., M-a and M-b in Figure 4.2, M-a and M-d in Figure 4.3, M-a and M-b in Figure 4.4) or lateralized dominance (e.g., M-b and M-c in Figure 4.3), while only one bilateral distribution was observed (i.e., M-c in Figure 4.4 Pre-/Post-rTMS). In terms of spectral patterns, distinct from auditory and visual networks, somatomotor subnetworks showed more peaks and higher amplitudes in the beta band than in the alpha band.

For the frontoparietal network (Figure 4.2-4.4), 6, 2 and 3 subnetworks were detected in three datasets, respectively. They mostly covered the prefrontal cortex with either unilateral (e.g., F-a and F-c in EC/EO) or bilateral (e.g., F-b in EC/EO) distributions.

For the unilateral subnetworks, symmetric pairs could be found in all three datasets (e.g., F-a and F-c in Figure 4.2, F-a and F-b in Figure 4.3, F-a and F-b in Figure 4.4). Several unilateral subnetworks (F-a and F-b in Figure 4.2, F-a and F-b in Figure 4.3) and one bilateral subnetwork (F-b in Figure 4.2) showed activity on both the lateral side(s) and the medial wall(s) of the hemisphere(s). Opposite correlation values were observed in F-d in EC/EO covering the left prefrontal cortex. These subnetworks had dominant peaks in the beta band with a few in the alpha band in their spectral patterns.

For the DMN network (Figure 4.2-4.4), 1, 3 and 6 subnetworks were detected in three datasets, respectively. These subnetworks exhibited more complicated spatial patterns than the other four networks. The only one detected in EC/EO covered the bilateral posterior cingulate cortex (PCC). Three subnetworks in HC/MdDS covered the medial prefrontal cortex (mPFC) and the bilateral PCC. Six subnetworks detected in Pre/Post-rTMS (Figure 4.4) covered the mPFC (D-a, D-b, and D-c), the inferior parietal lobe (IPL, all subnetworks except D-a), and PCC (D-d and D-e). In addition, a subnetwork (D-c) showed strong negative correlations between the mPFC and both the right PCC and the left IPL. Negative correlations were also observed in D-b between the mPFC and the right IPL. The spectral powers of all these networks showed peaks in the alpha band. Some from the Pre/Post-rTMS dataset also had another peak in the beta band.

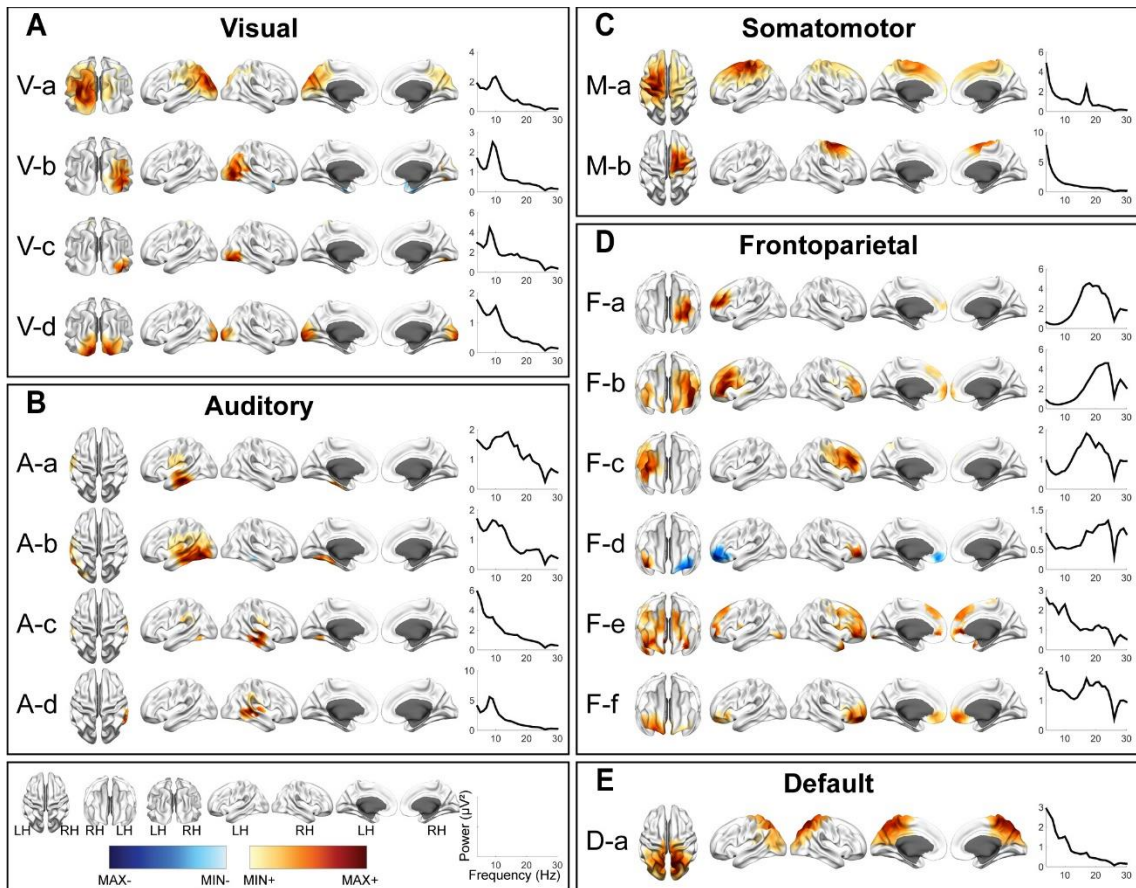


Figure 4.2 Spatial and spectral patterns of RSNs from the EC/EO EEG data (A) visual, (B) auditory, (C) somatomotor, (D) frontoparietal, and (E) default mode networks. Group-level SCT maps were thresholded at $p < 0.01$, cluster-based correction. (Figure as originally published in Li, Yuan, Shou, Cha, Sunderam, Besio and Ding (2018). *Front. Neurosci.* 30 May 2018. doi: 10.3389/fnins.2018.00365)

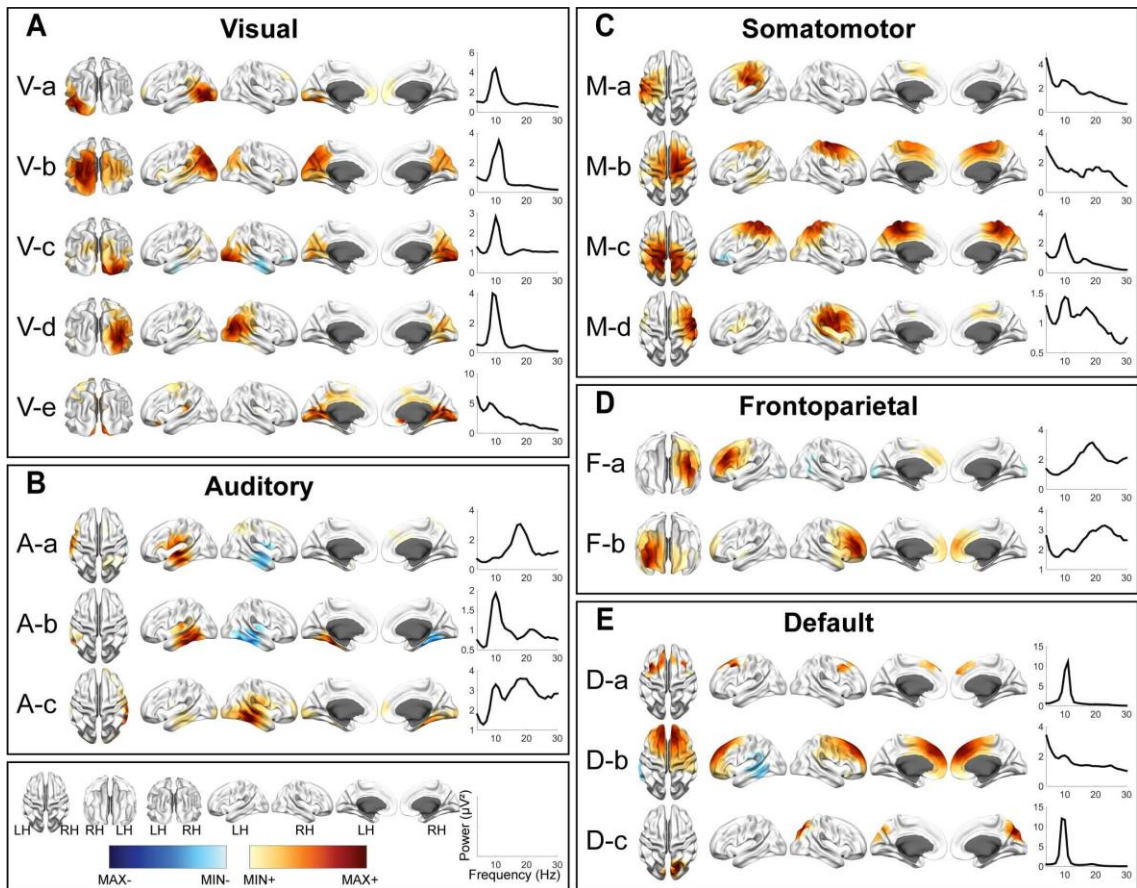


Figure 4.3 Spatial and spectral patterns of RSNs from the HC/MdDS EEG data (A) visual, (B) auditory, (C) somatomotor, (D) frontoparietal, and (E) default mode networks. Group-level SCT maps were thresholded at $p < 0.01$, cluster-based correction. (Figure as originally published in Li, Yuan, Shou, Cha, Sunderam, Besio and Ding (2018). Front. Neurosci. 30 May 2018. doi: 10.3389/fnins.2018.00365)

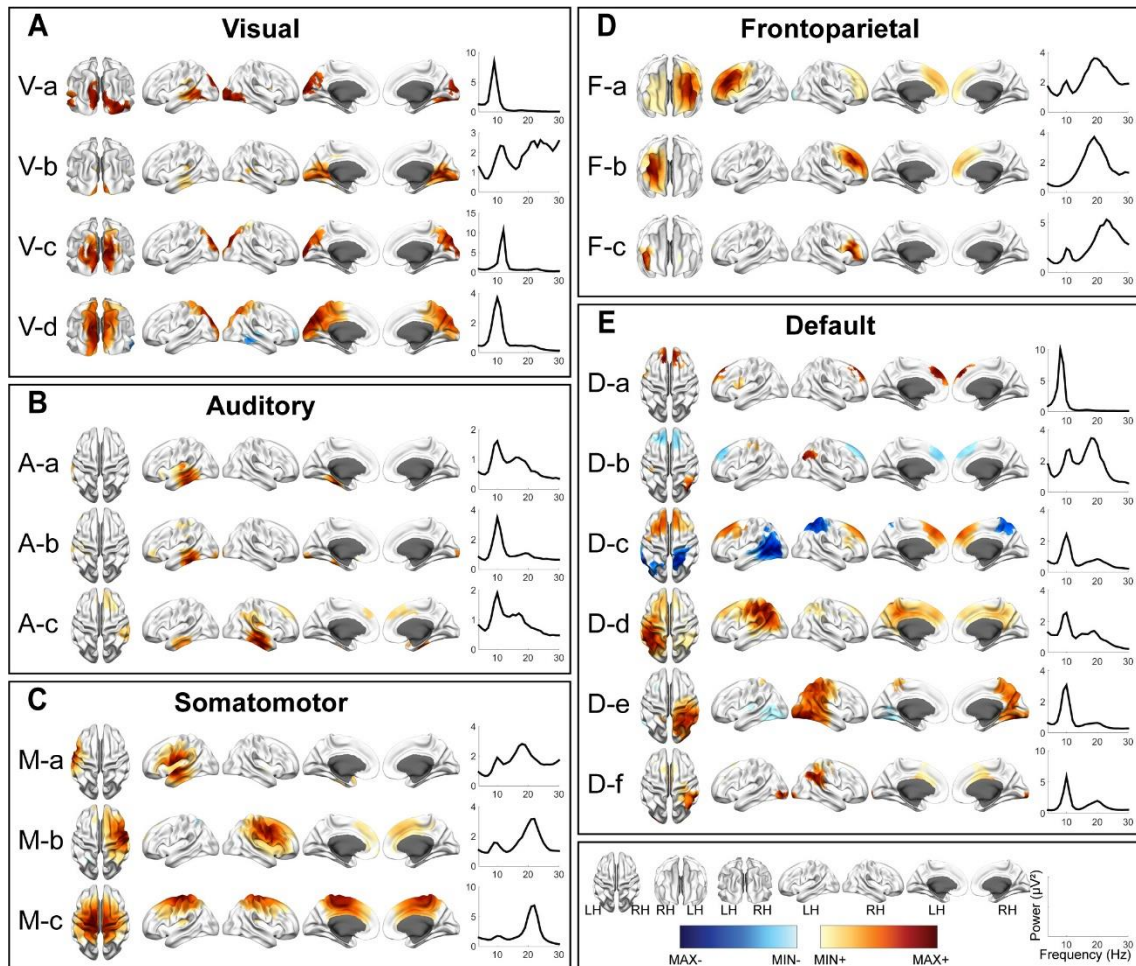


Figure 4.4 Spatial and spectral patterns of RSNs from the Pre-/Post-rTMS EEG data

(A) visual, (B) auditory, (C) somatomotor, (D) frontoparietal, and (E) default mode networks. Group-level SCT maps were thresholded at $p < 0.01$, cluster-based correction. (Figure as originally published in Li, Yuan, Shou, Cha, Sunderam, Besio and Ding (2018). Front. Neurosci. 30 May 2018. doi: 10.3389/fnins.2018.00365)

4.3.2 TFICA-SCT derived RSNs vs. fMRI derived RSN templates

TFICA-SCT derived RSNs were spatially compared to fMRI-derived RSN templates (Figure 4.5). Each EEG RSN was associated with an fMRI template RSN showing the largest TD. In general, all EEG RSNs in these five groups had significant TD values ($p < 0.01$, Bonferroni corrected) to their corresponding fMRI template RSNs (marked with “X” in the boxes along the diagonal tiles in Figure 4.5A-C). Similar patterns of spatial similarity was observed across three datasets. This observation was supported

by the comparison of the within-class and the cross-class TD values, in which the within-class TD values were significantly higher than the cross-class TD values (Figure 4.5D, t-test, $p < 0.01$) for all five network classes. For each dataset, the within-class TD values were always significantly higher than the between-class TD values when all network classes were considered together (Figure 4.5E, t-test, $p < 0.01$). Among different groups of RSNs, the DMN and frontoparietal networks showed competing similarity to a certain extent (Figure 4.5A-C).

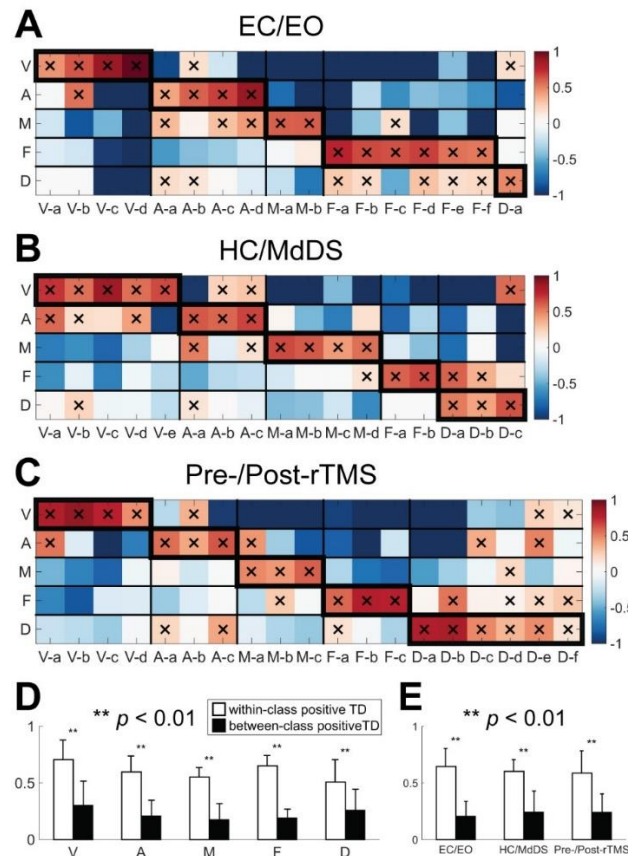


Figure 4.5 Template-matching degree (TD) between RSNs and fMRI RSN templates

(A) EC/EO; (B) HC/MdDS; (C) Pre-/Post-rTMS. (D) Bar-plots of the within-class (enclosed with thicker boundaries) and between-class positive TDs over five RSN classes; (E) Bar-plots of the within-class and between-class positive TDs over three datasets. Note that only positive TD values were considered since negative values indicate dissimilarity. (Figure as originally published in Li, Yuan, Shou, Cha, Sunderam, Besio and Ding (2018). Front. Neurosci. 30 May 2018. doi: 10.3389/fnins.2018.00365)

4.3.3 Consistency of RSNs across different datasets

The results of pair-wise RSN comparisons from different datasets are shown in Figure 4.6A (for the comparison between EC/EO and HC/MdDS), Figure 4.6A B (between EC/EO and Pre/Post-rTMS), and Figure 4.6C (between HC/MdDS and Pre/Post-rTMS). It is noted that significantly high spatial similarity can be observed in RSNs belonging to the same classes among three datasets. This was reflected in more positive TD values in the diagonal tiles than in the off-diagonal tiles, which were of significant difference (Figure 4.6D, t-test, $p < 0.01$) for the visual, auditory, somatomotor, and frontoparietal networks when all TD values Figure 4.6A-C) from three comparisons were included. For each pair-wise comparison, TD values in the diagonal tiles are higher than those in the off-diagonal tiles when all network classes were considered (Figure 4.6E, t-test, $p < 0.01$).

In terms of spectral powers, the alpha peak in the visual networks and the beta peaks in the frontoparietal networks were consistent across the three analyses. Additionally, peaks in both the alpha and the beta bands were consistently identified in both auditory and the somatomotor networks. The power spectra of the DMN revealed alpha peaks in all three analyses, though its amplitude in EC/EO was relatively low compared with the other two. The DMN in Pre/Post-rTMS showed more activity in the beta band as well, which was not obvious in the other two analyses, especially in those subnetworks including the posterior cortex. These results confirmed the similarity within the same classes of RSN in both spatial and spectral patterns.

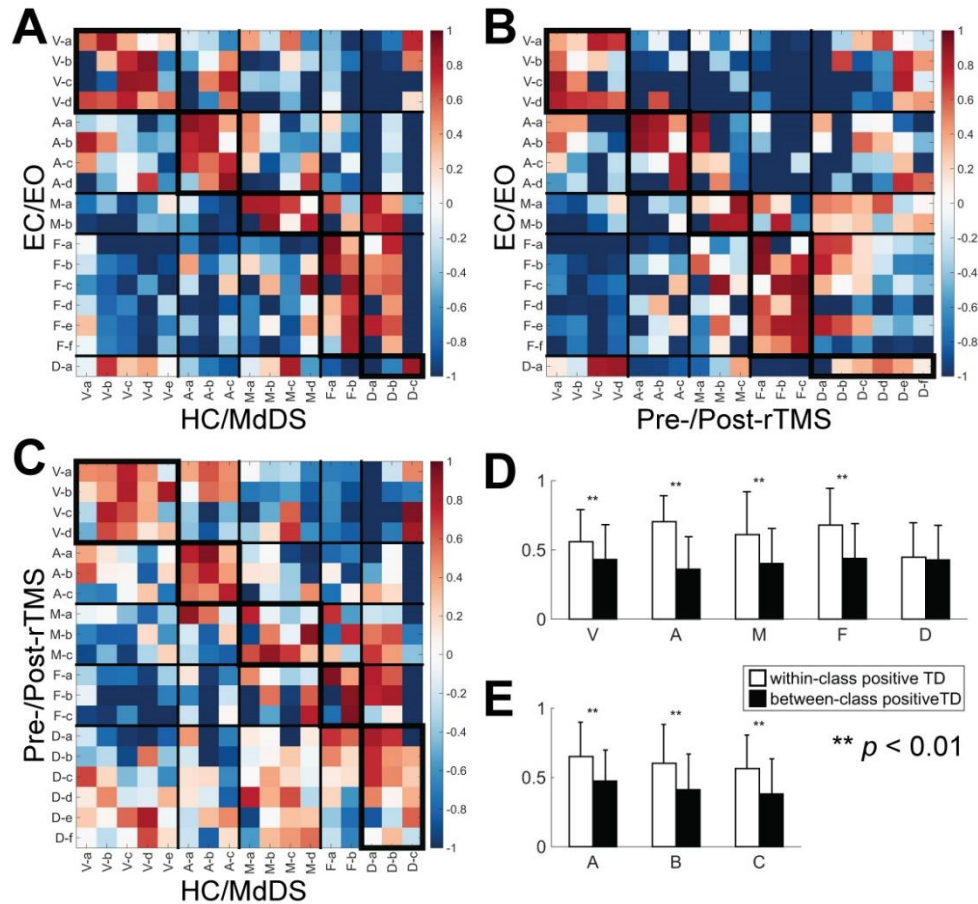


Figure 4.6 TD between a pair of SCTs from two different datasets (A) EC/EO vs. HC/MdDS; (B) EC/EO vs. Pre-/Post-rTMS; (C) HC/MdDS vs. Pre-/Post-rTMS; (D) Bar-plots of the within-class (enclosed with thicker boundaries) and between-class positive TDs over five RSNs. (Figure as originally published in Li, Yuan, Shou, Cha, Sunderam, Besio and Ding (2018). *Front. Neurosci.* 30 May 2018. doi: 10.3389/fnins.2018.00365).

4.3.4 Contrast resolutions of EEG RSNs revealing condition differences

The spatial differences of EEG RSNs in the three datasets (i.e., EC vs. EO in the EC/EO dataset, HC vs. MdDS in the HC/MdDS dataset, and Pre-rTMS vs. Post-rTMS in the Pre/Post-rTMS dataset) are illustrated in Figure 4.7. Their spectral power differences are summarized in Table 4.1.

Differences of RSNs between eyes-closed and eyes-open: Four subnetworks associated with the frontoparietal (i.e., F-b, F-d, F-2) and somatomotor (i.e., M-b) RSNs

were detected with significant differences ($p < 0.01$, cluster-based correction) (Figure 4.7A). Among them, significantly higher SCCs were detected in both left and right lateral prefrontal cortices (i.e., F-b and F-d), and significantly lower SCCs were detected in mPFC (i.e., F-e) in EO than in EC. In addition, the SCCs in the right motor areas were lower in EO than in EC. Regarding the spectral power (Table 4.1), significantly reduced powers in the theta and alpha bands were detected in the visual and somatomotor networks (visual theta: $p < 0.001$, visual alpha: $p < 0.001$, somatomotor theta: $p < 0.001$, motor alpha: $p < 0.005$), significantly enhanced alpha power ($p < 0.001$) in the frontoparietal network, and significantly enhanced beta powers ($p < 0.001$) in the visual, somatomotor, frontoparietal, and DMN networks were detected in EO as compared to EC.

Differences of RSNs between HC and MdDS: In the comparison of HC and MdDS patients, significant differences ($p < 0.01$, cluster-based correction) (Figure 4.6B) were detected in two auditory subnetworks and one DMN subnetwork. MdDS patients indicated significantly higher SCCs in the right temporal cortex and significantly lower SCCs in the left temporal cortex (i.e., auditory RSNs). Significantly higher SCCs were observed over mPFC. The differences in spectral powers were not statistically compared since the paired t-test was not applicable to this dataset.

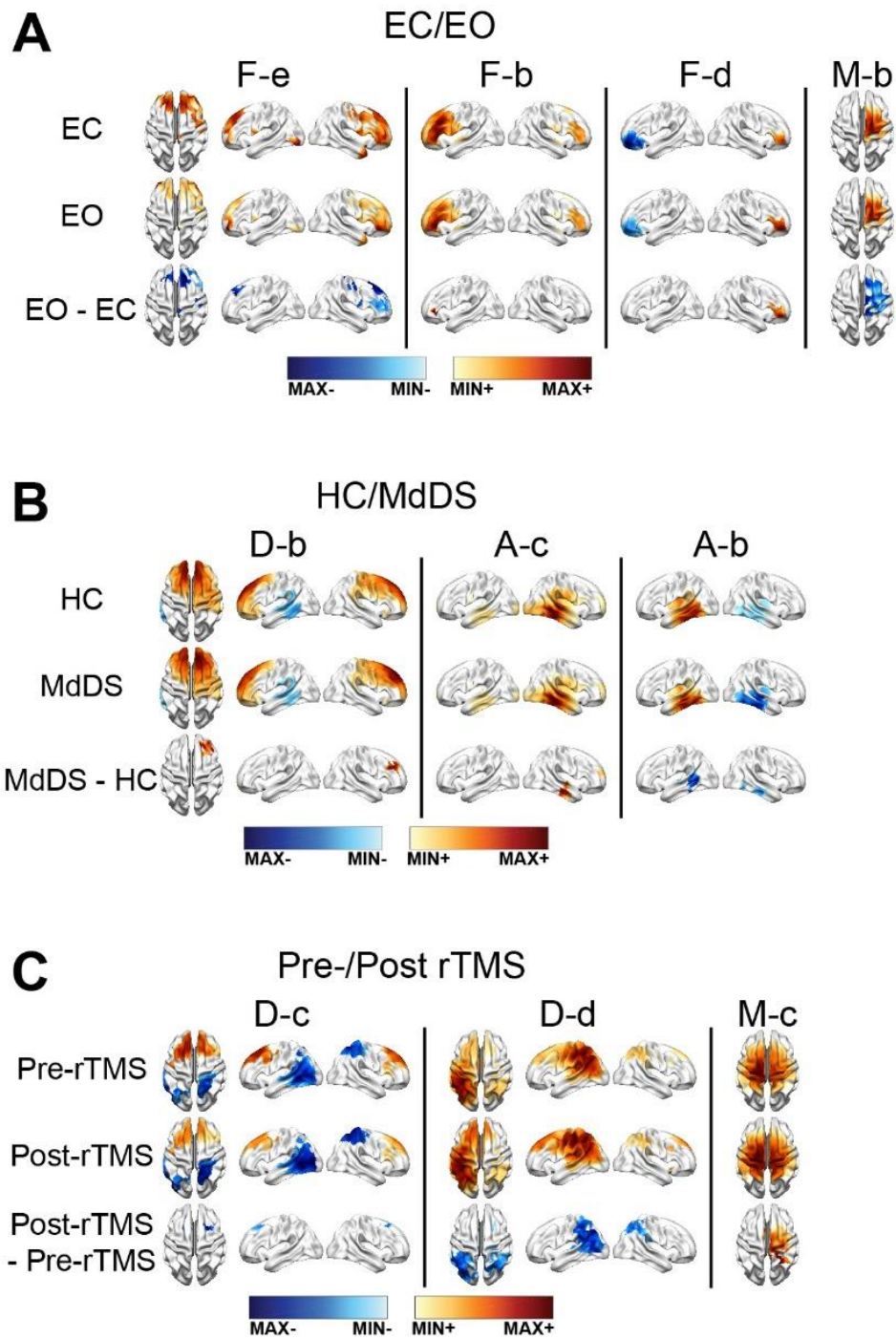


Figure 4.7 SCT differences between data from two conditions
 (A) EC/EO. (B) HC/MdDS. (C) Pre-/Post-rTMS. Maps were thresholded $p < 0.01$, cluster-based correction. (Figure as originally published in Li, Yuan, Shou, Cha, Sunderam, Besio and Ding (2018). *Front. Neurosci.* 30 May 2018. doi: 10.3389/fnins.2018.00365).

rTMS induced RSN changes: Three RSNs indicated significant rTMS induced changes between the Pre-TMS and Post-TMS conditions (Figure 4.7C). Specifically, following the rTMS treatment, it is observed with reduced SCCs in the bilateral mPFC nodes of a default-mode subnetwork (i.e., D-c) that showed negative connections between the frontal and parietal cortices, reduced SCCs in the bilateral IPL nodes of another DMN (i.e., D-d) that indicated positive connections between the frontal and parietal cortices, and enhanced SCCs in the right motor cortex in a somatomotor subnetwork showing bilateral patterns. Two classes of RSNs indicated significantly detected power changes, i.e., significantly enhanced theta power ($p < 0.05$) in the auditory network and significantly reduced alpha power ($p < 0.001$) in the DMN network, following rTMS treatment.

EC/EO					Pre-/Post-rTMS				
Theta					Theta				
	↑	<i>p</i> value	↓	<i>p</i> value		↑	<i>p</i> value	↓	<i>p</i> value
V	3	1.00	22	< 0.001	V	10	0.32	9	0.5
A	11	0.33	10	0.5	A	11	< 0.05	5	0.89
M	0	1.00	11	< 0.001	M	9	0.5	10	0.32
F	20	0.06	12	0.89	F	8	0.68	11	0.18
D	2	0.66	4	0.11	D	15	0.57	17	0.30
Alpha					Alpha				
	↑	<i>p</i> value	↓	<i>p</i> value		↑	<i>p</i> value	↓	<i>p</i> value
V	3	0.998	16	< 0.001	V	11	0.42	11	0.42
A	14	0.154	10	0.729	A	10	0.17	7	0.69
M	1	0.980	8	< 0.005	M	12	0.13	8	0.75
F	29	< 0.001	7	1.00	F	12	0.19	9	0.67
D	1	0.688	3	0.06	D	6	1.00	28	< 0.001
Beta					Beta				
	↑	<i>p</i> value	↓	<i>p</i> value		↑	<i>p</i> value	↓	<i>p</i> value
V	22	< 0.001	5	1.00	V	8	0.86	14	0.07
A	25	< 0.001	3	1.00	A	12	0.13	8	0.75
M	5	0.71	8	0.13	M	11	0.18	8	0.68
F	41	< 0.001	1	1.000	F	11	0.18	8	0.68
D	5	< 0.001	0	0.97	D	17	0.57	19	0.31

Table 4-1 Summary of spectral power differences
 (A) EC/EO and (B) Pre-/Post-rTMS. BOLD: $p < 0.05$ at least.

4.4 Discussion and Conclusion

In the present study, a new data-driven analysis framework, termed as TFICA-SCT, was developed to directly probe RSNs from EEG data. The proposed framework

combined EEG source imaging, ICA in the time-frequency domain and statistical correlation analysis, allowing the reconstruction of RSNs over a broad frequency range with unsurpassed high temporal resolution, as compared to RSN definitions from fMRI data of low resolutions in both time and frequency domains. Meanwhile, the method provided statistical power for subject-specific spatial patterns of RSNs. The proposed method was evaluated using three datasets of representative experimental conditions, i.e., eye-open vs. eyes-closed in healthy subjects, health controls vs. MdDS patients, and pre- vs. post-rTMS in MdDS patients. Various aspects of performance of the proposed framework, i.e., the capability of identifying multiple RSNs, their spatial and spectral properties, consistency, and robustness, were assessed. TFICA-SCT identified five groups of major resting-state networks, i.e., visual, auditory, somatomotor, frontoparietal, and DMN networks. These RSNs were found with significant and consistent spatial similarity to fMRI RSNs. Their spatial and spectral consistencies and detection robustness were suggested from comparisons among three different datasets. Identified RSNs further revealed condition-specific changes in both spatial and spectral domains for the three compared experimental conditions.

It is noted that the proposed SCT introduces a statistical framework that includes correcting false cross-correlations from autocorrelation and cluster-based statistical thresholding in constructing the tomography of RSNs. Many of these have already been adapted in fMRI (Rombouts et al., 2005; Roy et al., 2009; Woolrich et al., 2001), but were used for the first time in creating EEG/MEG RSN tomography in our algorithm. The introduction of correlation-based statistical analysis provides two merits. First, it provides statistical quantitative metrics to be further evaluated using such a

nonparametric statistical test, thereby identifying regions that significantly belong to specific RSNs. Second, it provides a means to obtain subject-specific spatial patterns, which are not readily yielded by the group-level ICA. Based on subject-specific spatial patterns, a group-level inference can be made about spatial differences of RSNs because of different conditions. The effect of autocorrelation on generating false cross-correlations has been considered in the present study, as in resting-state fMRI studies (Honey et al., 2009; Rombouts et al., 2005; Roy et al., 2009; Woolrich et al., 2001). This is particularly important for EEG RSN estimations since the oscillatory nature of EEG signals suggests potentially high autocorrelations. The nonparametric statistical test is based on Monte Carlo simulations (Smith and Nichols, 2009), which utilize a cluster-based thresholding technique to address the multiple comparison problem. While the considerations behind these statistical and correlation analyses are similar to those used in 3D volumetric fMRI data, their implementation in EEG/MEG RSN estimations is new and distinct in terms of the data domain, which is a highly convoluted 2D surface, i.e., the cortex.

Among three sets of experimental data, five major resting-state networks, including visual, auditory, somatomotor, frontoparietal, and default mode networks, have been identified and represented with different numbers of subnetworks (Figure 4.2-4.4). The spatial patterns of these identified RSNs indicate high spatial similarity to RSN templates from fMRI (Figure 4.5) (Yeo et al., 2011), as well as to fMRI RSNs reported in other literature (Liu and Duyn, 2013; Richiardi et al., 2015; Smith et al., 2009; Smith et al., 2012). These RSNs further indicate high spatial similarity among data from three experiments (Figure 4.6), while contrast-dependent variations can still be observed in

both spatial (Figure 4.7) and spectral features (Table 4.1). All these results demonstrate the effectiveness and robustness of the proposed framework in identifying the cortical-level RSNs directly from EEG across different cohorts of individuals. These findings are in line with previous reports that found RSNs in EEG data (Liu et al., 2017; Yuan et al., 2016) and/or MEG data (Brookes et al., 2011b; de Pasquale et al., 2010; Hipp et al., 2012). Previous EEG/MEG RSN research and advancements in TFICA-SCT indicate that RSN organizations can be retained from body surface recordings of brain signals via modeling and computation. The remarkable similarity between RSNs identified in fMRI and electrophysiological recordings (i.e., EEG/MEG) converges on the notion that RSNs as network-level organizations of distributed neural activity represent a fundamental aspect of brain physiology that are reflected in electrical and hemodynamic brain signals.

It is observed that the detection of EEG RSNs suggests several differences as compared with fMRI RSNs. Our results (Figure 4.2-4.4) revealed both lateralized RSNs and bilateral RSN from EEG, with a greater number of lateralized than bilateral RSNs, while fMRI literature indicates more symmetric and bilateral RSNs (Agosta et al., 2012; Damoiseaux et al., 2006; De Luca et al., 2006). However, this fact does not suggest inaccuracies in EEG RSNs results. First, lateralized RSNs from TFICA-SCT are consistent with resting EEG data analysis in the electrode domain, in which lateralized potential distributions toward either the left or right hemisphere have been reported (Ding et al., 2014; Yuan et al., 2012a). Second, while an EEG RSN is lateralized, another symmetric EEG RSN on the contralateral hemisphere can be found (Figure 4.2-4.4). This difference might be due to the intrinsic differences in brain electrical and hemodynamic signals, in which EEG is more dynamic and directly linked to underlying network

communication mechanisms than fMRI (Laufs, 2008; Mantini et al., 2007; Yuan et al., 2012a). Multiple subnetworks detected for each RSN class from EEG in the present study might reflect the fact that the networking of multiple nodes (or regions) in an RSN is dynamic rather than stationary. This notion has been observed in fMRI RSNs as well (Chang and Glover, 2010; Hindriks et al., 2016), in which the architect of the whole brain network is dynamic. While most of these fMRI RSN studies reveal dynamics at the network level built on RSNs, the present study suggests that the intrinsic organization of individual RSNs are also dynamic (Deco et al., 2011; Fox et al., 2005; van den Heuvel et al., 2008). Furthermore, less lateralized RSN patterns in fMRI might be due to the convolution from the electrical response to the hemodynamic response, which can increase correlations among different RSNs (Yuan et al., 2016). It can be further promoted due to the global contribution of respiration and blood flow to the hemodynamic process (Birn et al., 2006; Shmueli et al., 2007; Wise et al., 2004).

The second difference between fMRI and EEG RSNs is the observation of cross-talk between EEG RSNs, especially between the frontoparietal and DMN networks. The confusion might be partially caused by the mismatch between the bilateral templates of fMRI RSNs and more lateralized EEG RSNs, as discussed above. The non-optimal selection of metrics (e.g., vectorized cortical maps for calculating spatial correlation) and protocol (e.g., unique paired match) in the analysis procedure might contribute to it as well. The cross-talk could also be partially due to the vicinity of the regions involved in these two networks. Lastly, cross-talk could be influenced by artifacts in EEG recordings and inaccuracies of modeling and computation processes in TFICA-SCT. As an example, the DMN identified from EEG is of less spatial similarity to the template compared to the

other four networks. DMN constitutes multiple key regions, include mPFC, PCC, bilateral IPL (Buckner et al., 2008). Additionally, lateral temporal cortex and hippocampal cortex are often observed to be engaged as well (Buckner et al., 2008; Damoiseaux et al., 2007). Signals from mPFC are likely to be corrupted by residual artifacts of eye movements and blinks after preprocessing (Ille et al., 2002; Joyce et al., 2004). The inverse method, i.e., MNE, has limited penetration and accuracy in estimating deep sources such as those from the cingulate cortex (Gorodnitsky et al., 1995; Pascual-Marqui, 1999), resulting in poor estimates of the PCC in DMN. This can be improved with more advanced ISI techniques (Liao et al., 2013; Zhu et al., 2014). The spatial smoothing effect (Babiloni et al., 2005; Baillet and Garnero, 1997; Pascual-Marqui, 1999) in the ISI process might further obscure multiple regions of DMN that are close to each other.

The high temporal resolution of EEG signals over fMRI signals enables the investigation of spectral properties of individual RSNs, which is significant in understanding human brain communication mechanisms in both healthy and sick persons (Klimesch, 1999; Kounios et al., 2008; Mantini et al., 2007; Rangaswamy et al., 2002) since invasive electrical recordings have suggested different functional roles of different brain rhythms in communication (Canolty et al., 2006; Crone et al., 1998; Crone et al., 2006). Results in the present study show dominant alpha band activity in visual networks, which have been observed in MEG studies (Brookes et al., 2011b). The somatomotor networks have typically shown both alpha and beta spectral peaks while the frontoparietal networks have shown a strong peak in the beta band, which is consistent with MEG RSN studies (Brookes et al., 2011b; Mantini et al., 2007). Strong beta activity has been reported

in DMN (Brookes et al., 2011b; Laufs et al., 2003b; Mantini et al., 2007), especially in mPFC (D-b and D-c in Figure 4.3). Furthermore, power spectra changes have been observed due to different conditions, e.g., reduced alpha power in the visual and somatomotor networks, enhanced beta power in the frontoparietal network when eyes are open (Figure 4.2), and reduced alpha power in DMN in MdDS patients after rTMS (Figure 4.4) (see detailed discussions below). While data are preliminary, evidence behind them attest to the value of spectral powers of RSNs beyond spatial distributions (such as from fMRI) in understanding fundamental communication mechanisms in healthy brains and altered ones in patients. Future studies can use this additional RSN property, together with their spatial property, to investigate clinical problems in more depth.

The present results are generated based on unbiased and wide spectrum EEG data, whereas other approaches reported with MEG (Brookes et al., 2011b) or combined EEG and fMRI (Goldman et al., 2002; Laufs et al., 2003a) exploit pre-determined, narrow band-passed data. The advantage of using wide-spectrum data is to give unbiased weights to activity in all frequency points, which is essential in a data-driven approach. Furthermore, many RSNs in the present study suggest activity in more than one frequency band (e.g., alpha and beta in the frontoparietal network). While the present study only includes three frequency bands (i.e., theta, alpha, and beta bands), more bands, e.g., the gamma band, which may play an important role in functional connectivity (Kounios et al., 2008; Ossandón et al., 2011; Rutter et al., 2009), can be included in future studies as necessary.

The present study further demonstrates the capability of TFICA-SCT in detecting contrast differences in conditions involving both healthy and sick persons and both at baseline and after treatment. Contrast differences are reflected in two metrics. One is the thresholded SCC value after Eqs. (8)-(11), which indicates the affinity of a source point to an RSN (significant SCC: affinity to the RSN; non-significant SCC: no affinity to the RSN; the level of affinity indicated by the significant SCC value). The other metric is the spectral power at theta, alpha, or beta band for an RSN, which indicates the strength of an RSN that could change depending on the number of source points affined to the RSN and the accumulated strength from all affined source points. In the comparison between the eyes-closed and eyes-open conditions, the metrics of spatial affinity and spectral power indicate reduced activities in the visual and somatomotor networks with eyes open, especially in the low-frequency band (including the alpha band). The phenomenon has been well documented in literature (Fox and Raichle, 2007; Jao et al., 2013; Marx et al., 2004; Raichle et al., 2001; Yang et al., 2007). These two metrics also suggest increased beta band activities with eye open in the frontal and motor areas, which is consistent with previous EEG literature (Barry et al., 2009; Barry et al., 2007). Frontal areas are more active when persons are awake according to fMRI findings (Corbetta et al., 1998; Marx et al., 2004). Individuals with MdDS showed reduced spatial affinities in the left auditory RSN, which suggest hypo-connectivity that is consistent with hypo-metabolism from fMRI and PET studies, both in location and direction of abnormal connectivity (Cha et al., 2012). In the MdDS patients who responded to the treatment of rTMS, reduced spatial affinity and alpha power in the DMN RSNs were observed, lowering their hyper-connectivity in DMN (Figure 4.4B), which suggests the potential reason behind the

responsiveness of these patients to rTMS. Reduced alpha power in DMN following rTMS, indicative of the treatment effect, has been similarly revealed in our previous study based on sensor-level EEG data (Ding et al., 2014). Enhanced theta power in the auditory RSNs (Figure 4.6) might compensate hypo-connectivity observed in MdDS patients (A-b, Figure 4.6B).

In conclusion, a new framework termed as TFICA-SCT, integrating inverse source imaging, data-driven method, and statistical correlation analysis, is proposed to probe resting-state networks from scalp recordings in human brain electrical signals. The present study has evaluated the proposed framework in three experimental datasets to reconstruct, study, and compare resting state networks in both healthy persons and sick individuals. Results of the present study showed that the proposed framework could reconstruct large-scale, network-level organization of spontaneous brain activity that significantly resembles the spatial patterns of fMRI RSNs. Reconstructed EEG RSNs are able to reveal condition-dependent variations in both spatial and spectral domains. Its capability in estimating RSN spectral properties is further beyond the capability of fMRI in studying RSNs and the present results suggest that these spectral properties could be used to segregate healthy individuals with those with a clinical diagnosis. Since EEG can be recorded simultaneously with fMRI, the combination of EEG and fMRI suggests a more powerful tool in understanding human brain networks, with unsurpassed spatial, temporal, and spectral resolutions. Clinical uses of these technologies are of significant potential values in identifying biomarkers for various neurological and psychiatric disorders, both for diagnosis and for treatment monitoring.

In summary, I demonstrated in this study that TFICA-SCT was a promising technology to reconstruct and investigate RSNs based on EEG data only. It integrated a new ICA method, i.e., TFICA, and a new statistical processing step, i.e., SCT. Results of the present study showed that the proposed framework can reconstruct large-scale, network-level organization of spontaneous brain activity that significantly resembles the spatial patterns of fMRI RSNs.

5 An Advanced Inverse Source Imaging Method for Reconstructing EEG Resting State Networks

5.1 Introduction

In my previous studies, research was mainly focused on the development of ICA. On the contrary, the ISI step was not given research attention. Specifically, the conventional MNE was adopted in the ISI step due to its satisfactory performance in our previous study (Yuan et al., 2016). In this study, the research attention was paid to the ISI step, which has been largely overlooked by previous studies. An advanced ISI technique was adopted in the computational framework introduced in the previous chapters. The aim of this study is to investigate if the new ISI technique can advance the reconstruction of RSNs using the framework developed in the previous Chapter.

EEG/MEG data are recorded by sensors at the scalp surface, which cannot be directly linked with anatomical and structural substrates in the human brain. As a solution to this problem, various inverse source imaging (ISI) techniques have been developed to map EEG/MEG measurements to the domain of the cortex (Grech et al., 2008; Pascual-Marqui, 1999). More recently, with the progress in modeling and computational techniques (Brookes et al., 2011b; Ding and Yuan, 2013; Ding et al., 2013; Liao et al., 2013; Ramkumar et al., 2014), many studies have successfully reconstructed cortical maps of RSNs from EEG/MEG. Not only results with significant spatial similarity to fMRI RSNs have been revealed, but also temporal and spectral characteristics that are beyond the capability of fMRI have been reported (Brookes et al., 2011b; Liu et al., 2017; Ramkumar et al., 2012; Yuan et al., 2016). These efforts have provided new insights, in parallel and complementary to fMRI, into the neural mechanism underlying RSNs. On the other hand,

comparisons and cross-validations between fMRI RSNs and EEG/MEG RSNs also provided a means to interpret electrophysiological underpinnings of fMRI RSNs, given the unsettled debate regarding origins of these intrinsic networks (Cole et al., 2010; Friston et al., 1996; Mitra et al., 1997).

In these recent studies of EEG/MEG RSNs (Brookes et al., 2011a; Li et al., 2018; Liu et al., 2017; Yuan et al., 2017), both ISI techniques (Grech et al., 2008; Mosher et al., 1999; Pascual-Marqui, 1999) and data-driven methods (Hyvärinen and Oja, 2000; Lee et al., 1999) play crucial roles in the reconstruction of RSNs from EEG/MEG data. In these frameworks, ISI was used to achieve data projection from the sensor space to the source space, which lays the groundwork for and define the anatomic space of data from subsequent analyses. In resting conditions, there are no stimuli or behavioral references as found in task conditions when assessing EEG/MEG data. Therefore, data-driven methods are needed to recognize patterns or extract features from resting-state EEG/MEG data. In the majority of EEG/MEG RSNs studies, data-driven methods have been applied to data processed by the ISI and then, to identify patterns in the source space, where fMRI RSNs have been studied (Allen et al., 2012; Beckmann et al., 2009; Calhoun and Adali, 2012).

Independent component analysis (ICA) is the most popular data-driven method in RSN studies for both EEG/MEG and fMRI. Different ICA algorithms, such as infomax ICA (Lee et al., 1999) and FastICA (Hyvärinen and Oja, 1997), have been used to reconstruct RSNs (Liu et al., 2017; Yuan et al., 2016). Despite the difference in ICA algorithms, ICA has been implemented in various ways on data as well. In particular, the spatial ICA, widely used on fMRI data (Beckmann et al., 2009; Calhoun et al., 2009),

aims to discover spatially independent components. Temporal ICA, widely performed on EEG/MEG data (Brookes et al., 2011b; Yuan et al., 2016), searches independency in the temporal domain. Recently, a new ICA method, termed as time-frequency ICA, has been proposed to obtain components that are statistically independent in the tempo-spectral domain (Li et al., 2018; Shou et al., 2012). To define EEG/MEG RSNs on the cortical surface, i.e., the same domain of fMRI RSNs, both spatial and temporal ICAs have been used in combination with EEG/MEG ISI techniques (Grech et al., 2008; Mosher et al., 1999; Pascual-Marqui, 1999; Yuan et al., 2016). The way to implement ICA is largely determined by the property of data, in which the large dimension (either spatial or temporal) is selected as the sample domain in ICA to obtain reliable ICA analysis (Hyvärinen et al., 2004; Hyvärinen and Oja, 2000; James and Hesse, 2004).

In contrast to various versions of ICAs, only a few conventional ISI algorithms have been used in EEG/MEG RSN studies, including minimum norm estimation (MNE) (Yuan et al., 2016), beamforming (Brookes et al., 2011a), and low-resolution electromagnetic tomography (LORETA) (Liu et al., 2017). These conventional ISI techniques are not desirable due to the limited accuracy in estimating spatial patterns, in particular, the problem of spatial smoothing (Pascual-Marqui, 1999). It usually leads to overestimated spatial extents of activated cortical sources from EEG/MEG, which is crucial to many clinical applications (Ding et al., 2007; Zhu et al., 2013). At the same time, many advanced ISI algorithms beyond these conventional ones have been reported (Ding et al., 2013; Liao et al., 2013; Liao et al., 2012; Zhu et al., 2017), which either demonstrate better performance in reconstructing spatial patterns of cortical activities or in estimating their temporal fluctuations. In the previously reported studies, RSNs have been obtained

by applying ICA to outcomes of ISI. Therefore, the performance of ISI methods is of particular importance since any discrepancy in ISI solutions can be propagated to ICA and be amplified in subsequent analyses. Taken all together, it is crucial to improve the performance of ISI solutions in order to obtain more reliable and accurate estimations of cortical RSNs from EEG/MEG.

A recently developed ISI algorithm, i.e., sparse source imaging (SSI) (Chang et al., 2010; Ding and He, 2008; Ding et al., 2013; Uutela et al., 1999; Zhu et al., 2013), has been demonstrated to be a promising technique for cortical source estimation. SSI utilizes the L1-norm regularization technique to address the non-uniqueness and ill-posedness of the inverse problem, which makes it different from algorithms using the L2-norm regularization such as MNE and LORETA (Grech et al., 2008; Mosher et al., 1999; Pascual-Marqui, 1999). The L1-norm regularization allows accurate and optimal inverse reconstructions in under-sampled conditions when source signals to be estimated are sparse as compared with the number of measurements and measurements are incoherent against the support of signals (Candes and Tao, 2005; Donoho, 2006). The sparseness of signals in the source domain has been explored to reconstruct brain activities using EEG/MEG under task conditions (Ding and Yuan, 2012, 2013), which is reasonable considering brain areas evoked by tasks are expected much smaller than the whole brain, i.e., the entire source domain. However, such an assumption may not be valid in studying resting-state brain networks since, as revealed in fMRI data, brain activities associated with multiple RSNs are widely distributed over the whole brain (Beckmann et al., 2005; De Luca et al., 2006). Recently, SSI algorithms have been improved to utilize sparseness in a transform domain, e.g., the variation domain (Ding, 2009) and the wavelet domain

(Ding et al., 2013), instead of the original source domain. The wavelet transform has been demonstrated to be an efficient method in compressing signals without losing accuracy (Chang et al., 2010), and therefore it can be used to reconstruct widely distributed brain activities in RSNs. One of our previous studies has demonstrated that inverse solutions can be improved by enforcing sparseness in both variation and wavelet domains, as compared with algorithms considering sparseness in a single transform domain (Zhu et al., 2014). In spite of its promising performance, this technique has never been employed in any RSN studies. Therefore, a computational framework with the use of this new ISI method is expected to achieve further improvement in RSN reconstructions.

In the present study, the novel ISI method, i.e., variation and wavelet-based SSI (VW-SSI) (Zhu et al., 2014) was employed into our previously reported framework (Li et al., 2018) for estimating cortical RSNs from resting-state EEG data. The performance of the proposed method was evaluated using both simulated and experimental EEG data, and it was compared with the same framework but using MNE in the step of ISI. The performances of both VW-SSI and MNE in our previously reported framework (Li et al., 2018) were assessed regarding spatial and temporal accuracy with statistical analysis. Their results were further compared using five RSN templates defined with fMRI data as references.

5.2 Materials and Methods

5.2.1 Variation and Wavelet-based Sparse Source Imaging

From a methodological point of view, source imaging of EEG/MEG is an inverse problem, in which EEG/MEG measures are used to estimate the cortical sources. In order

to solve the inverse problem, an appropriate model is required for the forward problem, which can be expressed as:

$$\Phi = As + n \quad \mathbf{5-1}$$

where Φ is the EEG measurement; s is the cortical source; n is the noise; A is the lead field, which links the measurement and the source. Its inverse problem has infinite solutions to a given set of measurements because the number of sources is much larger than the number of measurements (Baillet et al., 2001). To obtain unique solutions to the inverse problem, L1-norm regularizations have been proposed as a regularization method by enforcing sparseness in the source domain (Ding and He, 2008; Uutela et al., 1999) or the transform domain (Ding, 2009; Ding and He, 2008; Liao et al., 2012). L1-norm regularizations can be expressed as:

$$\min \|Hs\|_1 \text{ subject to } \|\Phi - As\|_2 < \varepsilon \quad \mathbf{5-2}$$

where H is either an identity matrix or a transform matrix. ε denotes the regularization parameter which confines the discrepancy between the measurements and the model.

A variety of L1-norm regularizations have been introduced with the use of different transform matrix H , such as variation based sparse source imaging (V-SSI) and wavelet based sparse source imaging (W-SSI) (Ding, 2009; Liao et al., 2012). Both techniques have their advantages: V-SSI has excellent capability in reconstructing source extents; W-SSI can provide a much sparser representation of more distributed cortical activities (Ding, 2009; Liao et al., 2012). A recent study has proposed a new method, variation and wavelet based SSI (VW-SSI), which integrates the advantages of V-SSI and W-SSI (Zhu et al., 2014) and is used in the present study.

The L1-norm regularization of VW-SSI method is based on both variation and wavelet transforms and result in the optimization problem

$$\min(\|Vs\| + \lambda\|Ws\|) \text{ subject to } \|\Phi - As\|^2 < \varepsilon \quad 5-3$$

where $\lambda > 0$ is a hyper-parameter to balance the penalties of the variation and the wavelet.

What follows is a brief overview of the variation and wavelet transforms. More details can be found in the study by Zhu et al. (2014).

Variation Transforms: The variation transform is obtained by calculating variations between two neighbored triangles on the cortical surface (Ding, 2009)

$$V = \begin{bmatrix} v_{11} & v_{12} & \cdots & v_{1N} \\ v_{21} & v_{22} & \cdots & v_{2N} \\ \vdots & \vdots & \ddots & \vdots \\ v_{p1} & v_{p2} & \cdots & v_{pN} \end{bmatrix} \quad 5-4$$

$$\begin{cases} v_{ij} = 1; v_{ik} = -1; \text{if elements } j, k \text{ share the same edge} \\ v_{ij} = 0; \text{otherwise} \end{cases}$$

where P is the total number of triangular edges in the cortex model.

Wavelet Transform: To design wavelet functions on the cortical surface, a multi-resolution model of the cortical surface was obtained as follows. The original cortical surface segmented from MRI data (see section **Construction of Models** below) was used as the finest mesh for this multi-resolution model in order to generate lower-resolution meshes. A seed triangle on the fine level mesh (starting with the original mesh), which was arbitrarily selected, and its three neighbored triangles were merged into one triangle on the coarse level mesh. The merging was repeated until all triangles on the fine level were processed, leading to a new coarse mesh. By recursively merging the meshes, a set of multi-resolution cortical surface model was generated.

With the multi-resolution model, wavelet transform matrix is defined as (Liao et al., 2012):

$$W_m = \begin{bmatrix} (G^m)^{\frac{1}{2}} A^{m-1} A^{m-2} \dots A^0 \\ B^{m-1} A^{m-2} \dots A^0 \\ \vdots \\ B^1 A^0 \\ B^0 \end{bmatrix} \quad 5-5$$

where superscript denotes the level of the multi-resolution cortical model. G^m is the Gram-Schmidt matrix (Bonneau et al., 1996) in which the diagonal elements are areas of triangles on the cortical mesh at level m . A_m represents the proportion between the area of a triangle at level $m+1$ and the area of the four corresponding triangles at level m . B_m has the property of semi-orthogonality in basis functions (Bonneau et al., 1996), and it is obtained by solving,

$$\begin{cases} A^m (G^m)^{-1} (B^m)^T = 0 \\ B^m (G^m)^{-1} (B^m)^T = 1 \end{cases} \quad 5-6$$

After obtaining the variation transform and the wavelet transform, the problem in Eq. 3 can be solved using the second-order cone programming (SOCP) technique (Ben-Tal and Nemirovski, 2001) from the Matlab toolbox Self-Dual-Minimization (SeDuMi) (Sturm, 1999). More details about the conversion of the optimization problem in Eq. 3 into a SCOP problem and the SOCP solver can be found in the study of Zhu et al. (2014).

5.2.2 Computational Framework to Reconstruct RSNs

In the present study, the computational framework for RSN reconstructions was built upon previously reported frameworks (Ding et al., 2014; Li et al., 2018; Yuan et al., 2016) with minor modifications. It should be noted that MNE was used to solve the inverse problem in our previous study, while the present study employed VW-SSI to map sensor-space EEG data into the source space. Then, envelopes of source-space data were calculated through the Hilbert transform (Brookes et al., 2011b), which was followed by

the normalization using a z-transform to reduce inter-individual variations when data from multiple subjects were used. Afterward, the normalized envelopes from experimental data (see section **Experimental Protocols**) were concatenated in the temporal domain, yielding group-level data. However, the temporal concatenation was not conducted on the simulated data (see section **Simulation Protocols**). Then, the Infomax ICA (Lee et al., 1999) from the EEGLAB toolbox (Delorme and Makeig, 2004) was applied to the data to obtain multiple independent components (ICs).

After ICA, statistical correlation analysis (Li et al., 2018) was applied to all ICs as briefly described as follows. First, correlation coefficients (CCs) between the time course of each IC and the time course of each dipole source were calculated for all individual participants in the group. CC values were converted into z-values using the Fisher's z-transformation. All correlation maps were then smoothed by an iterative smoothing algorithm, i.e., the heat kernel smoothing with Full Width at Half Maximum of 8 mm (Chung et al., 2005). The group-level z-score maps were calculated by averaging across participants (Alexander, 1990; Silver and Dunlap, 1987) with autocorrelation being used to correct the degree of freedom (Bartlett, 1935). To quantitatively define brain regions of ICs, the averaged correlation maps were further thresholded. The thresholding was achieved by applying a source-wise t-test against zero to z-scores from all participants, and source points that achieve the significant threshold of $p < 0.01$ was kept. To address the multiple comparison problem, a cluster-based correction method was employed (Hagler et al., 2006) to remove small clusters in order to reduce false positives, where clusters were defined as regional active sources that were spatially connected (i.e., triangular elements of clusters were connected on the cortical surface model). Each RSN

usually consisted of multiple regional sources, which was similar to the definition of RSN nodes in fMRI RSN literature (Li et al., 2018; Zhu et al., 2013).

5.2.3 Construction of Models

Structural MRI data from FreeSurfer (<https://surfer.nmr.mgh.harvard.edu/>) (Fischl, 2012) were used to build the source model, i.e., the cortex where s was defined, and the volume conductor model for the calculation of A in Eq. 1. The surfaces of the cortex and other layers of the anatomical structure (the brain, skull, and scalp) were extracted and segmented. In the volume conductor model, the volumes between different layers are assigned different conductivity values (the scalp: $0.33/\Omega\text{m}$, the skull: $0.0165/\Omega\text{m}$, and the brain: $0.33/\Omega\text{m}$) (Lai et al., 2005). In the source model, the cortical surface was meshed and triangulated into 40,960 triangles, each of which represents a dipole source at its center with the orientation being perpendicular to its surface. The sensors were then co-registered to the volume conductor model by aligning three landmarks, i.e., nasion, left and right pre-auricular points. Based on the model and locations of EEG electrodes, the lead field, A in Eq. 1, can be calculated using the boundary element method (Hamalainen and Sarvas, 1989).

5.2.4 Simulation Protocols

In order to quantitatively evaluate the performance of VW-SSI, a simulation with 100 iterations was proposed as follows. In each simulation, three clusters of multiple distributed sources were generated on the cortical surface to mimic connected regions of networks. Three clusters were formed by three, two, and one source(s), respectively. Each source encompassed a surface region with the diameter of ~ 20 mm without overlap (Figure 5.1).

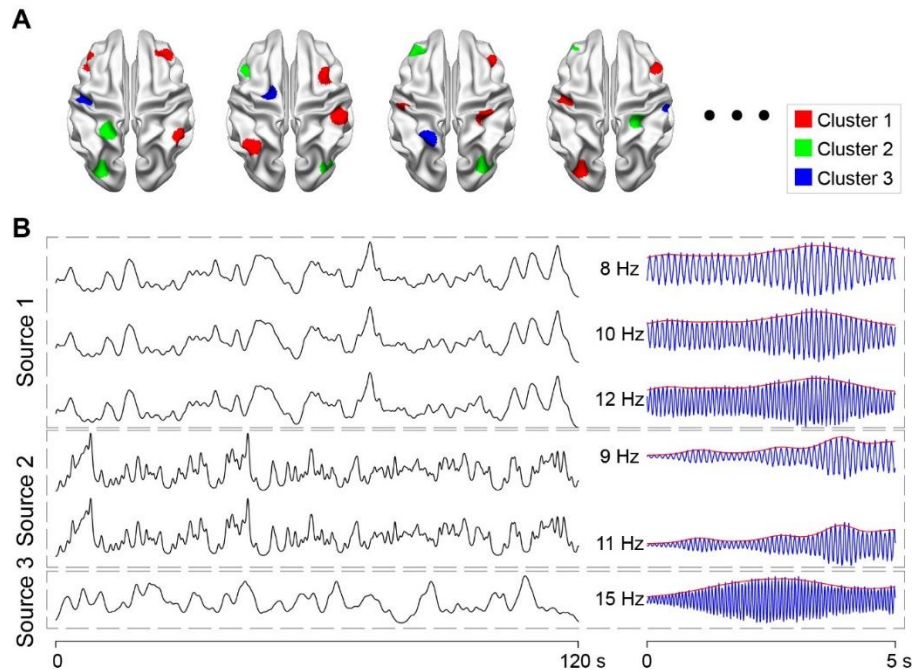


Figure 5.1 Schematic of the simulation

(A) The location and extent of three simulated clusters in different simulations. (B) Envelopes and carrier frequencies of the simulated clusters.

To mimic spontaneous fluctuations of RSNs, amplitude-modulated signals were generated based on the protocol of the study by Ramkumar et al (2014), where cortical activities were modeled being driven by thalamic origins, as briefly described below. In the first place, a binary spike train was generated with 1% of the elements being 1's, aiming to simulate a thalamic pacemaker signal (Steriade and Llinás, 1988). The sampling frequency of the signal was 150 Hz, and the duration was 2 minutes. To simulate the thalamic drives arriving at the cortex, six Gaussian functions were generated with 8 sec temporal support and standard deviation ranging from 4/15 to 8/5 in steps of 4/15. After obtaining the Gaussian functions and the spike train, the Gaussian functions were convolved with the spike trains, and then the convolved signals were summed to mimic the temporal summation of multiple thalamic drives. The envelopes of the three clusters were independent of each other, which met the requirement of independence in the ICA

analysis (see section **Computational Framework to Reconstruct RSNs**). In terms of carrier signals, six sinusoids of different frequencies were generated for the sources. Specifically, 8 Hz, 10 Hz, and 12 Hz were for the three sources of the first cluster; 9 Hz and 11 Hz for the two sources of the second cluster; 15 Hz is for the only source in the third cluster. Uniformly distributed noise with a standard deviation (SD) 5% of the SD of the waveform was added to the sinusoids. Then carrier signals were multiplied with corresponding envelopes to generate simulated time courses for all clusters. In order to mimic brain noise on the cortical surface, pink noises were added to the whole cortical surface (Ramkumar et al., 2014) with the standard deviation (SD) of noise 10% of SD of simulated signals. Afterward, simulated cortical signals were mapped to the sensor space by multiplying the lead field. Finally, Gaussian white noises with a SD 5% of the averaged SD of sensor-space signals were added to simulate measurement noises. In each iterative of simulation, locations for sources were randomly selected.

5.2.5 Experimental Protocols

Twenty healthy participants (all females; age: 48.8 ± 7.2 years) and forty patients (all females; age: 51.8 ± 12.5 years) of mal de débarquement syndrome (MdDS) (Cha et al., 2012; Ding et al., 2014) were recruited in the study. Here, only resting-state data from healthy participants were reported. It should be noted that only female participants were included because the prevalence of females is much higher than males in MdDS (Cha, 2009), and the healthy group was matched to the patient group in terms of gender. This study was approved by Western IRB (www.wirb.com). All participants were informed about the protocol of the study and signed a written informed consent form prior to the experiment. A 126 channel EEG system with a BrainAmp amplifier (Brain Products

GmbH, Munich, Germany) was used in the present study. The ground electrode was placed at AFz in the international 10-20 system, and FZ was chosen as the reference channel. Resting-state recordings were obtained for five minutes for each participant while they were asked to keep still and have their eyes closed.

For each participant, structural MRI data were obtained using a 3D MPRAGE sequence (124 contiguous axial slices with 1.2 mm slice thickness; matrix size = 256×256; FOV = 220 mm × 198 mm; TR/TE/TI/TD = 5 /1.98 /725 /1400 ms, flip angle = 8 degree; sampling bandwidth = 31.25 kHz, SENSE acceleration = 2).

5.2.6 Data Analysis Protocols

Simulation: The computational frameworks were applied to the simulated data, using six as the number of assumed ICs (as compared with three actual simulated ICs). To find three ICs that matched the simulated clusters, the spatial and temporal correlation coefficients (CCs) between the ICs and the simulated clusters were calculated for all possible pairs, resulting in two three-by-six matrices. Specifically, the spatial CC was calculated between the cortical map of an IC and the simulated cortical maps of the cluster. The temporal CC was calculated between the time course of an IC and the simulated envelopes of the cluster. Then, the spatial and temporal CC matrices were normalized by dividing the maximal CCs of each row, which was followed by the summation of the two normalized CC matrices. The IC with the largest sum in each row was matched to the corresponding simulated cluster.

Experimental Data Analysis: After obtaining resting-state EEG data, data were pre-processed individually with an established pipeline including rejection of bad segments, interpolation of bad channels, and re-reference to common average (Ding et

al., 2014). Then data were down-sampled to 250 Hz and band-pass filtered from 4 Hz to 30 Hz. ICA was used to remove artifacts caused by movement, eye movement, and noise.

By applying the framework to the experimental resting state data, forty ICs were obtained. The thresholded spatial patterns were assessed with fMRI-RSN templates (Yeo et al., 2011) as references. RSNs were selected from the ICs according to their spatial features such as spatial distributions and spatial coverages. Furthermore, based on the template matching metric (see section **Evaluation Protocols**), these ICs were categorized into five groups, including visual, auditory, somatomotor, frontoparietal, and default mode networks.

Other than the spatial patterns, the present study also investigated the spectral features of RSNs. In order to obtain spectral powers for the selected ICs, amplitude-modulated time courses of ICs were reconstructed by multiplying the unmixing matrix obtained from the group-level ICA with original cortical data obtained by VW-SSI in individual participants. Given the time courses for each IC, short time Fourier transform (STFT) was performed with 1-second non-overlapping window, resulting in time-frequency representation with a resolution of 1 Hz. Frequency bins ranging from 4 Hz to 30 Hz were kept as the bands of interest, i.e., theta, alpha, and beta bands. After STFT, the power at each frequency bin was calculated, averaged over epochs, and then averaged over participants, resulting in the power spectra of selected ICs.

5.2.7 Evaluation Protocols

In order to evaluate the performance of VW-SSI in reconstructing RSNs, a control framework was proposed with VW-SSI replaced by the minimum norm estimation (MNE) (Dale and Sereno, 1993; Hämäläinen and Ilmoniemi, 1984), which had been adopted in

the previous studies of reconstructing RSNs from EEG and/or MEG (Li et al., 2018; Yuan et al., 2016). In parallel with the frameworks using VW-SSI, the control framework repeated the data analysis for both simulated and experimental data. The results from the control framework were compared with the results from VW-SSI for the purpose of evaluation.

A series of evaluation protocols were conducted to assess the performance of frameworks using different ISI methods in reconstructing EEG RSNs. First, reconstructions from simulated data were compared with the ground truth through the matching process as discussed above (see section **Data Analysis Protocols**). Second, RSNs obtained with the use of VW-SSI and MNE were compared with fMRI RSN templates as the references (Yeo et al., 2011). Third, the region sizes of cortical RSN maps were quantitatively compared.

Simulation: Reconstructions of RSNs with the use of VW-SSI and MNE were compared in terms of spatial and temporal accuracies. Regarding the spatial pattern, spatial CCs between simulated clusters and matched reconstructed RSN maps (unthresholded) were used to quantitatively evaluate the accuracy of results. Besides, area under the receiver operating characteristic (ROC) curve, i.e., AUC (Grova et al., 2006), was also calculated and compared between these RSN maps to evaluate the accuracy of source locations and extents. Moreover, the similarity between these maps was quantified by a template-matching method (Greicius et al., 2007) with normalization as follows:

$$TD(t, c) = \frac{Z_{in}(t, c) - Z_{out}(t, c)}{Z_{in}(t, c) + Z_{out}(t, c)} \quad 5-7$$

where TD referred to the template-matching degree; t is the index for the simulated cluster and c is the index of the IC. Z_{in} is the averaged value from source points inside simulated

clusters and Z_{out} is the averaged value from source points outside. The temporal accuracy was assessed using the metrics of temporal CC and root mean square error (RMSE) between estimated time courses of ICs and simulated envelopes (Molins et al., 2008). A paired t-test was performed on all five metrics to evaluate whether there were statistical differences between the two sets of results with the uses of VW-SSI and MNE.

Experiment: To evaluate spatial patterns of obtained EEG RSNs, cortical maps obtained with the use of both VW-SSI and MNE were compared with the five fMRI RSN templates (Yeo et al., 2011) as references, including visual, auditory, somatomotor, frontoparietal, and default mode networks. TD values were calculated for all possible pairs between the reconstructed cortical RSN maps (thresholded) from selected ICs and the five fMRI RSN templates, generating a confusion matrix for both VW-SSI and MNE methods. To assess the confusion of RSNs, TD values for the within-class group and the between-class group were compared using unpaired t-tests across five networks. To evaluate the spatial similarity to fMRI RSN templates, within-class TD values from both VW-SSI and MNE were compared using a t-test. The same test was performed on between-class TD values from VW-SSI and MNE as well to evaluate the capability of two methods in distinguishing different RSNs. Furthermore, the above tests involving between-class TDs were repeated using only positive between-class TDs (still use all within-class TD values) since between-class TDs tended to have more negative TD values, which might lead to overlooking few but significant existing confusions (usually indicated by positive TD values).

To examine whether VW-SSI could help addressing the problem of spatial smoothing as found in conventional ISI methods, spatial extents of RSN regional sources

were used as an indicator to study the overall spatial sizes of reconstructed cortical sources in RSNs. The spatial extents were calculated as the numbers of triangular elements of regional sources in thresholded maps for RSNs (see section **Computational Frameworks to Reconstruct RSNs**). The spatial extents of all regional sources in all reconstructed RSNs from both VW-SSI and MNE were compared. An unpaired t-test was performed on values of the metric from VW-SSI and MNE.

5.3 Results

5.3.1 Simulation

Figure 5.2 illustrates spatial and temporal patterns of the selected RSNs and the simulated clusters from examples out of 100 simulations. In each simulation, the locations of simulated clusters/sources were different due to the random selection, while the simulated envelopes of the clusters were the same across simulations. In the examples, the three simulated clusters were detected by both VW-SSI and MNE with high spatial and temporal similarities. In the detection of individual clusters, residual patterns from other clusters were observed in results from both methods. For instance, the red cluster showed residue patterns in the estimated pattern for the green cluster, the middle column in Figure 5.2A in both VW-SSI and MNE. However, such residue patterns seemed more common in results from MNE than VW-SSI (e.g., the red cluster showed negative residue patterns in the estimated pattern for the green cluster, the middle column in Figure 5.2C, for MNE but not obvious for VW-SSI; the green cluster showed negative residue patterns in the estimated pattern for the red cluster, the left column in Figure 5.2C, for MNE but not for VW-SSI). Furthermore, the results from MNE seemed more widely spread, while the results from VW-SSI were more focused in areas of simulated sources and their

neighborhoods. This phenomenon was prominent in Figure 5.2A, in which VW-SSI results exhibited high spatial contrast while MNE results were overspread. In the detection of temporal envelopes of individual clusters, both methods had their advantages in different aspects. VW-SSI was better in depicting general tendencies of these envelopes. For instance, the high amplitude for the red cluster close to the end of the time course was better reconstructed in VW-SSI than MNE (especially in the left column of Figure 5.2D). On the contrary, MNE was better in catching subtle fluctuations of these envelopes. For example, the valley immediately after 20 s in the red cluster was better reconstructed in MNE than VW-SSI (especially in the left column of Figure 5.2C).

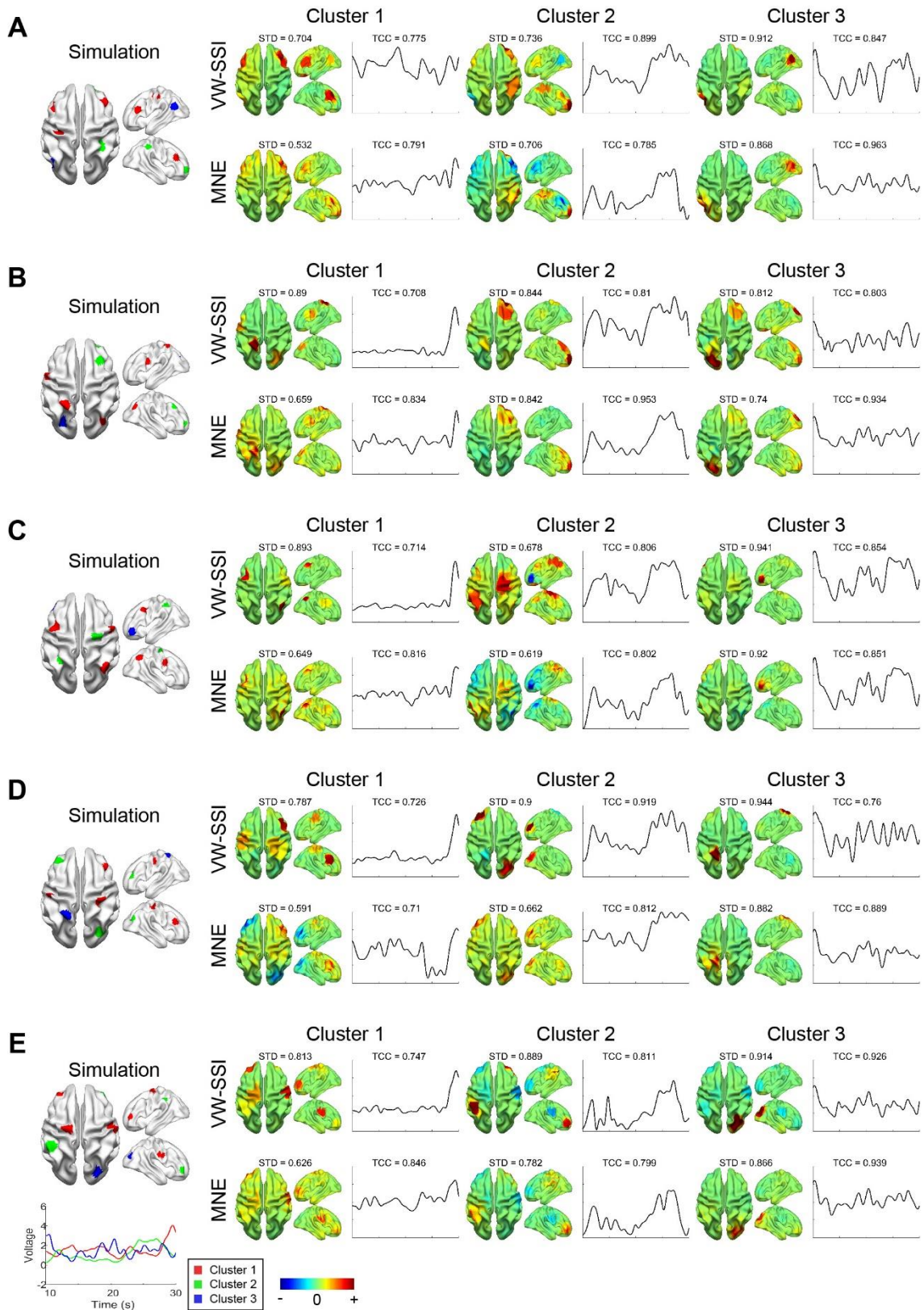


Figure 5.2 Spatial and temporal reconstruction of the simulation
 Left: spatial and temporal patterns of simulated clusters. Right: the reconstruction of spatial and temporal patterns.

The summary of metric values for both spatial and temporal accuracies of 100 simulations was shown in Figure 5.3. As indicated by the metric values of spatial CC (Figure 5.3A), TD (Figure 5.3B), and AUC (Figure 5.3C), the performance of VW-SSI is significantly better than MNE (i.e., spatial CC: $p < 1e-10$; TD: $p < 1e-10$; and AUC: $p < 5.02e-4$) in reconstructing the spatial properties of simulated networks. With regard to temporal CCs (Figure 5.3D), MNE performed significantly better than VW-SSI ($p < 1e-10$). On the other hand, VW-SSI exhibited much better temporal RMSE values than MNE ($p < 1e-10$). For both MNE and VW-SSI, there were large variations across 100 simulations (e.g., large value ranges of the metrics in Figure 5.3A and 5.3C for both MNE and VW-SSI; more outliers in Figure 5.3A, 5.3B, 5.3D, and 5.3E for MNE). The fact indicated the performances of both methods were location dependent (since source locations were randomly selected over the entire cortical source model). It is worth to note that VW-SSI was better in terms of variations and therefore more robust since it exhibited fewer outliers than MNE.

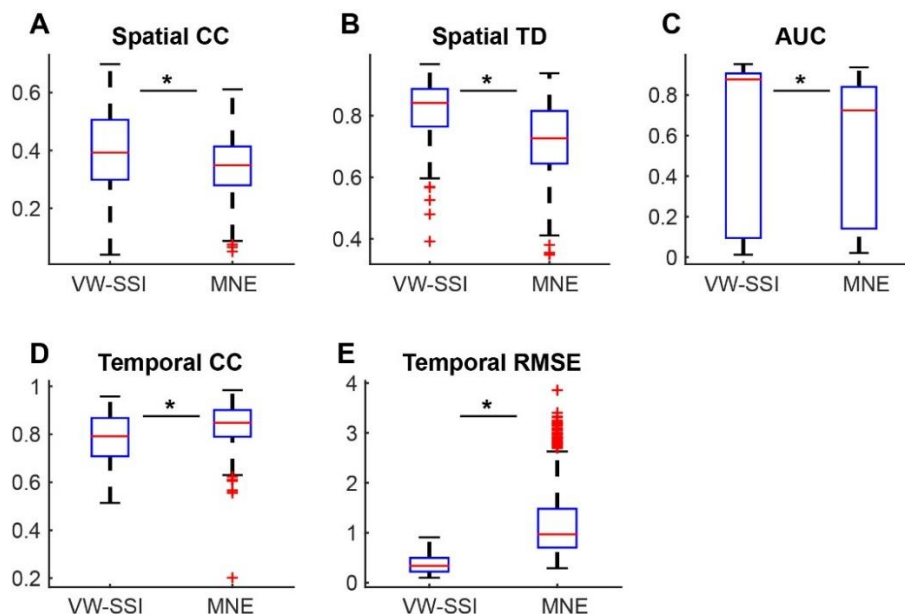


Figure 5.3 Performance of VW-SSI and MNE in the simulation

5.3.2 Experiment

Spatial and Spectral Patterns of RSNs: Figure 5.4 and 5.5 illustrates spatial and spectral patterns of identified EEG RSNs from both VW-SSI and MNE. According to their spatial similarity to five fMRI RSN templates (Yeo et al., 2011), they were categorized into five RSN groups: visual (V), auditory (A), somatomotor (M), frontoparietal (F), and default mode (D) networks.

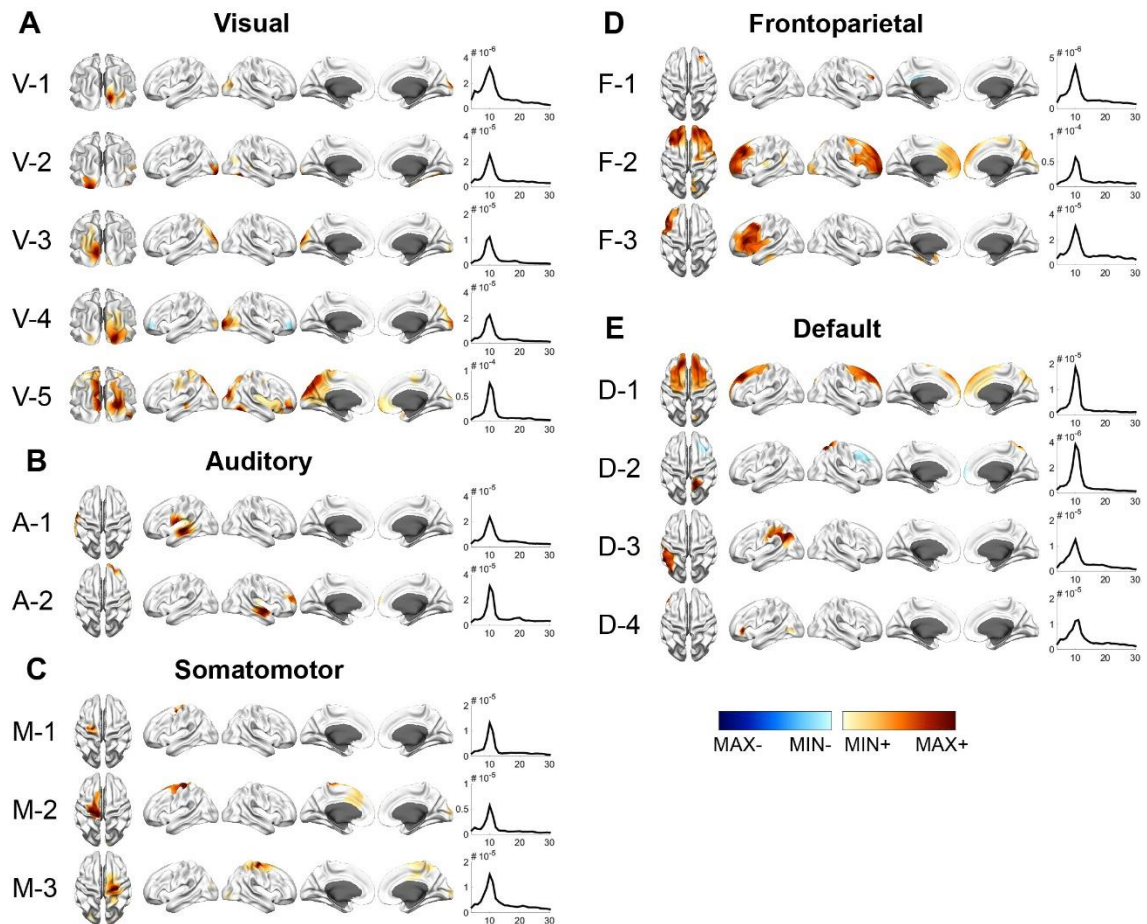


Figure 5.4 Spatial and spectral patterns of RSNs from VW-SSI
 (A) Visual. (B) Auditory. (C) Somatomotor. (D) Frontoparietal. (E) Default

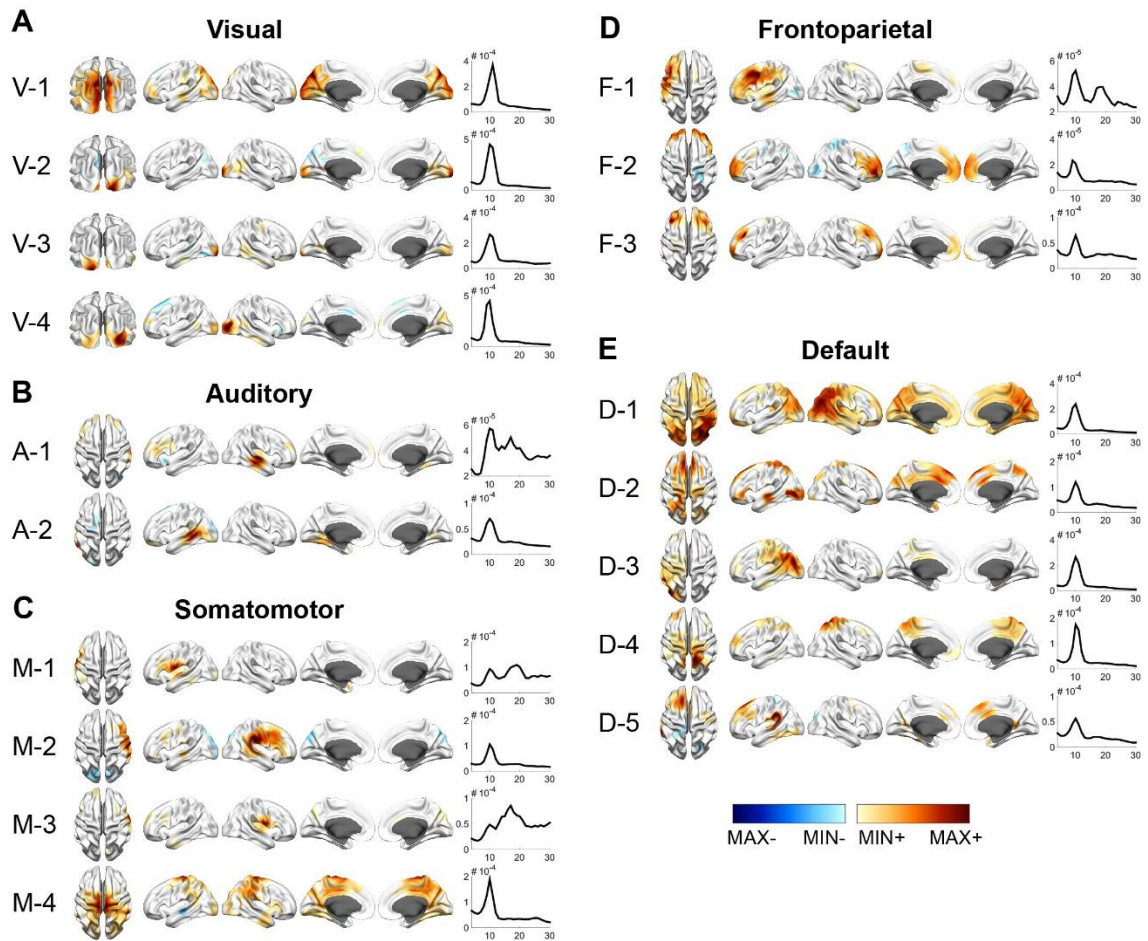


Figure 5.5 Spatial and spectral patterns of RSNs from MNE
 (A) Visual. (B) Auditory. (C) Somatomotor. (D) Frontoparietal. (E) Default

Each RSN group is consisted of more than one EEG RSN subnetworks with significant spatial resemblance identified. For the visual network, five subnetworks were detected using VW-SSI and four subnetworks were detected using MNE. The areas in these subnetworks were mainly found in the primary visual cortex (i.e., V-2, V-4 from VW-SSI, Figure 5.4, are same as V-2, V-3, V-4 from MNE, Figure 5.5) and the V2/V3 cortex (i.e., V-1, V-3, V-5 from VW-SSI, Figure 5.4, are same as V-1 from MNE, Figure 5.5). Some of these networks had bilateral symmetric distribution (e.g., V-1 in Figure 5.5). Some showed hemispheric dominance whereas the similar dominance was found on their symmetric hemispheres in other subnetworks (i.e., V-2, V-3 in Figure 5.5). In terms

of spectral patterns, the visual RSNs were characterized with evident peaks in the alpha band for both methods.

For the auditory network, both VW-SSI and MNE detected two subnetworks. These RSNs mainly covered the temporal cortices, with lateralized but symmetric distribution (i.e., A-1 and A-2 in Figure 5.4, are same as A-1 and A-2 in Figure 5.5). All auditory subnetworks had peaks in the alpha band while A-1 from MNE showed a peak in the beta band as well.

For the somatomotor network, three and four subnetworks were detected using VW-SSI and MNE, respectively. Three subnetworks from VW-SSI covered the premotor and primary motor cortices. Furthermore, M-2 and M-3 showed hemispheric dominances on symmetric areas. In MNE, M-4 covered the premotor and primary motor cortices while M-1, M-2, and M-3 covered lateral primary motor cortices, which were not detected in VW-SSI. M-1 and M-3 were symmetric, and M-4 showed bilateral symmetric distribution, which covered similar areas of M-2 and M-3 in VW-SSI. In terms of spectral patterns, two somatomotor subnetworks (i.e., M-1 and M-3) from MNE showed dominant peaks in the beta band while other subnetworks only had peaks in the alpha band.

For the frontoparietal network, both methods detected three subnetworks. They mostly covered the prefrontal cortex with either unilateral (e.g., F-1, F-3 in Figure 5.4 and F-1 in Figure 5.5) or bilateral distributions (e.g., F-2 in Figure 5.4; F-2 and F-3 in Figure 5.5). F-3 from VW-SSI covered the similar area as F-1 from MNE. F-1 and F-2 from VW-SSI covered the similar areas as F-2 and F-3 from MNE. These subnetworks all had the largest peaks in the alpha band while F-1 from MNE (Figure 5.5) also showed a peak in the beta band.

For DMN, four and five subnetworks were detected from VW-SSI and MNE, respectively. In comparison with the other four RSNs, the subnetworks of the DMN exhibited more variations. The subnetworks covered the medial prefrontal cortex (mPFC) (e.g., D-1 in Figure 5.4; D-2 and D-5 in Figure 5.5), the inferior parietal lobe (IPL) (e.g., D-3 in Figure 5.4; D-3 in Figure 5.5), and PCC (e.g., D-2 in Figure 5.4; D-4 in Figure 5.5). Symmetric patterns were available in results from both methods (e.g., D-1 in Figure 5.4; D-1 in Figure 5.5). In the comparison of two methods, D-2 and D-3 from VW-SSI covered the similar areas as D-3 and D-4 from MNE, respectively. D-1 from VW-SSI covered the similar areas as D-2 and D-5 from MNE in the frontal cortex, while D-2 from MNE had wider distributions over posterior cortices as well. All subnetworks from both methods exhibited the spectral peaks only in the alpha band.

Spatial patterns vs. fMRI RSN templates: Spatial patterns of RSNs derived using VW-SSI and MNE were further compared to fMRI-derived RSN templates using the concept of confusion matrix (Figure 5.6). The diagonal elements of the matrix represent the TD values of the same classes of EEG RSNs and fMRI RSNs, while the off-diagonal elements of the matrix represent the TD values of different classes of EEG and fMRI RSNs. Each EEG RSN was associated with an fMRI template RSN showing the largest TD. Similar patterns of spatial similarity indicated by the confusion matrices were observed for both methods, where diagonal elements in the confusion matrices showed much higher values than off-diagonal elements (Figure 5.6A and 5.6B). Furthermore, more negative values were observed in the off-diagonal matrix for VW-SSI (Figure 5.6A), which suggested the fact that the between-class differences in RSNs from VW-SSI were much larger than those from MNE. These observations were supported by the statistical

comparisons of the within-class and between-class TD values (Figure 5.6C). The within-class TD values were significantly higher than the between-class TD values (Figure 5.6C, t-test, $p < 0.001$) for both methods. The within-class TD values for VW-SSI are significantly higher than the within-class TD values for MNE (Figure 5.6C, t-test, $p = 0.0062$). The between-class TD values of VW-SSI are significantly lower than those of MNE (Figure 5.6C, t-test, $p = 2.8e-5$). In five classes of RSNs, visual and auditory networks exhibited relatively higher TD values than other networks while DMN showed relatively low TD values. For DMN, it was observed that the TD values were higher in results from VW-SSI.

Spatial extents: Figure 5.6D illustrates the statistics of the spatial extents of RSN node sources calculated from all reconstructed EEG RSNs showed in Figure 5.4 and Figure 5.5. The data indicated that VW-SSI had significantly smaller sizes of cortical sources reconstructed in all RSNs than MNE ($p < 0.0024$).

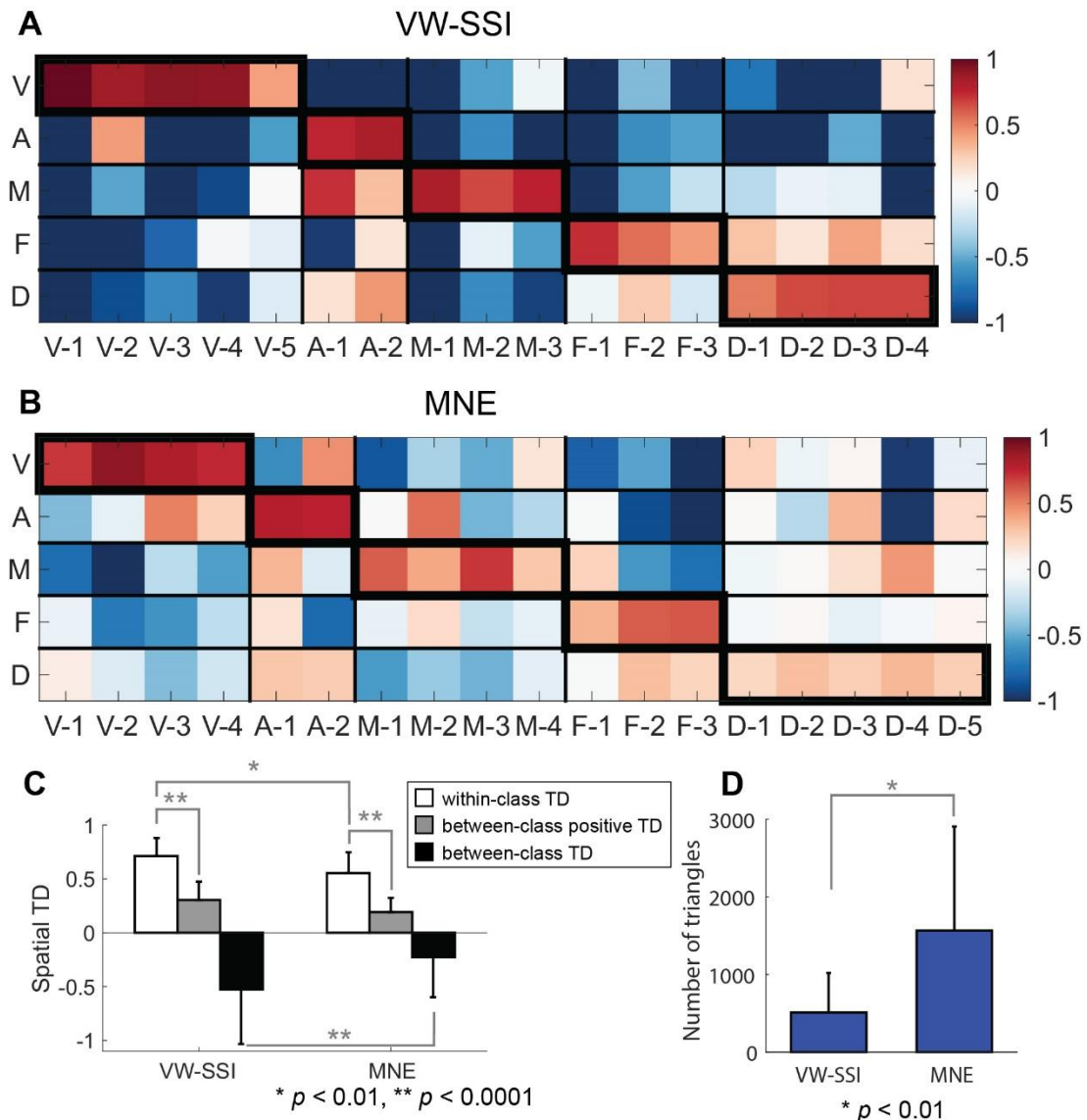


Figure 5.6 Spatial TD between spatial patterns and fMRI RSN templates
 (A) Spatial TD of VW-SSI. (B) Spatial TD of MNE. (C) Bar-plots of the within-class (enclosed with thicker boundaries) and between-class positive TDs over five RSN classes. (D) Cluster size.

5.4 Discussion

In the present study, a novel ISI method, i.e., VW-SSI, was used in our previously reported framework (Li et al., 2018) with the purpose of better estimating cortical RSNs from EEG data. In the original framework (Li et al., 2018), the reconstruction of EEG RSNs was achieved in three steps: mapping data from surface EEG/MEG recordings to

the cortical surface using ISI (i.e., MNE), extracting temporally co-activated spatial patterns using the data-driven approach (i.e., ICA), and generating thresholded cortical maps of RSNs through statistical correlation analysis. This study aims to improve the performance of the previously reported framework through adopting an advanced ISI technique (Zhu et al., 2014). The modified framework, together with a control framework that used MNE, were evaluated using both simulated and experimental resting-state EEG data. In the simulation, the reconstruction of multiple networked brain activities with the use of VW-SSI showed significantly better accuracies in estimating spatial patterns than results with the use of MNE (as indicated by all metrics). Meanwhile, VW-SSI was much better in estimating the coarse temporal scale and major temporal patterns than MNE (as indicated by the metric RMSE), while MNE is slightly better than VW-SSI in depicting detailed fluctuations (as indicated by the metric temporal CC). Using resting-state EEG data from healthy participants, it was demonstrated that the framework using VW-SSI could reconstruct RSNs that showed significantly higher spatial similarity to the fMRI RSNs templates than those obtained by the control framework. Results from VW-SSI further showed reduced spatial smoothing as those from MNE.

In contrast to the advancement of ICA in recent research (Brookes et al., 2011b; Li et al., 2018; Sockeel et al., 2016; Yuan et al., 2016), the critical role of ISI methods in the computational frameworks has been largely overlooked. Given the function (i.e., source mapping) and the implementation (i.e., before ICA) of ISI, it is believed that ISI largely determines the reconstruction accuracy of RSNs, especially in spatial estimations. While different aspects of spatial estimations have been considered in conventional ISI methods, the extents of distributed sources and the sparseness are two key features that

require research attention. The extents of estimated sources are the major factor in the association with specific anatomical structures and the definition of RSN regional nodes. In our previous study that used MNE (Li et al., 2018), the spatial patterns were diffused, making it difficult to localize regional nodes of RSNs. Regarding the sparseness, the whole-brain distribution of RSNs, as revealed in fMRI data (Beckmann et al., 2009; De Luca et al., 2006; Yuan et al., 2016), contradicts the assumption of sparseness of brain activities in the original source domain. Such an assumption is only valid under certain task conditions (Ding and He, 2008). Motivated by this limitation, recent studies have developed new SSI algorithms to explore sparseness in transform domains (Ding, 2009; Ding et al., 2013; Mihcak et al., 1999). Wavelets are well-established techniques to compress signals without the compromise of accuracy and have been successfully implemented in many areas (Dang and Chau, 2000; Thayaparan et al., 2007). The wavelet-based SSIs have been developed for EEG/MEG neuroimaging (Chang et al., 2010), which significantly compresses source signals for their better sparse representations in the wavelet domain, and the improvements in inverse imaging results have been reported (Chang et al., 2010). At the same time, the variation-based SSI promotes sparseness at boundaries between active and inactive brain regions and, therefore, it can be used to estimate extents of brain activities. However, it does not constrain the overall norm of source signals that allows the flipping of active and inactive brain regions, which leads to estimation ambiguities (Zhu et al., 2014). The VW-SSI algorithm integrates the variation and wavelet, which therefore combines the advantages of both transforms in reconstructing distributed brain activities with their extent information.

The expected improvements in estimated cortical data from the novel ISI algorithm are indicated in the enhanced spatial reconstruction of RSNs, which are suggested in both simulations and experimental results. In the simulation, it is observed that spatial patterns from VW-SSI suggest several differences as compared with results from MNE. Regions revealed by VW-SSI had clearer boundaries, less smoothed distributions, and smaller source node sizes, while sources from MNE are in general spatially diffused and cover relatively large areas. These observations were further confirmed by data from quantitative metrics (Figure 5.3). Among the quantitative metrics, the spatial CC is more affected by accuracies of estimated source locations and extents. Using VW-SSI, the spatial CC is significantly improved as compared with results from MNE ($p < 1e-10$). It is noted that some spatial patterns of estimated clusters from both MNE and VW-SSI both show residue patterns of sources from other simulated clusters. This is because, although temporal envelopes of clusters were independent among different clusters, simulated noises could change such independences. Since the residue pattern is not observed in all simulated cases, it might also be explained by errors induced in the process of ISI since more errors are expected in some simulated cases, for example, these with simulated sources from deep brain areas (Acar and Makeig, 2013; Lin et al., 2006). The fact also suggests the importance of advancing ISI methods in better estimating EEG RSNs.

The experimental results further confirmed the improvement in spatial reconstructions. Five major resting-state networks, including visual, auditory, somatomotor, frontoparietal, and default mode networks, have been identified and represented with different numbers of subnetworks. The spatial patterns from both

methods showed remarkable similarity with the RSN templates from fMRI (Yeo et al., 2011). However, the spatial reconstructions from VW-SSI and MNE still exhibited several different features. Specifically, the thresholded regions of RSNs from VW-SSI showed high-contrast boundaries. Besides, regional source extents from VW-SSI was significantly smaller than those from MNE. These observations were further confirmed by statistical comparisons using quantitative metrics. With the fMRI RSN templates as references, the spatial patterns of RSNs from VW-SSI showed significantly higher TD than MNE. The between-class TDs from VW-SSI were significantly lower than MNE. These important results might be explained by the fact that the small spatial extent from VW-SSI can reduce the spatial confusion and overlaps across different anatomical structures. These findings suggest that the purpose of VW-SSI is fulfilled in the reconstruction of RSNs: its advantage in recovering cortical sources can be propagated to the outcome of the computational framework, bringing about accurate estimations of RSN locations and extents.

Besides the spatial reconstruction, the temporal and spectral estimations of RSNs are two significant aspects that influence the characterization of RSNs. VW-SSI, however, did not exhibit obvious advantages in these two aspects. It is difficult to conduct an experimental evaluation of the temporal and spectral reconstructions of RSNs because there is no compelling reference at resting-station conditions. The simulation results showed that VW-SSI generated significantly better results in the metric of the temporal RMSE ($p < 1e-10$) but worse results in the metric of the temporal CC ($p < 1e-10$) than MNE. VW-SSI seems better in catching the scale and the general structure of temporal fluctuations, while MNE seems better in catching fluctuation patterns with more details.

The general and detailed features of fluctuations are both crucial to investigate RSNs because they directly affect the analysis of the RSN dynamics (Chen et al., 2013). In the analysis of experimental data, temporal data were not presented (while available) due to the lack of reference points to evaluate them. Instead, the power spectra were derived from temporal data and presented for all RSNs (Figure 5.4 and 5.5). The present results indicate that different RSNs have different spectral features (Li et al., 2018; Mantini et al., 2007). In the results of VW-SSI, the power spectra mainly exhibited peaks in the alpha band while peaks were also observed in the beta band in the results from MNE.

The simulations in the present study were featured with the consideration of several realistic aspects of the human physiological processes, including realistic models for the generation of neocortical electrical activity (Ramkumar et al., 2014) and modeling of noise at different levels of neurophysiological processes and measurements (Pijn et al., 1991; Teplan, 2002). Also, the locations of simulated sources and clusters were randomly generated, which made simulation results more generalizable over the whole human brain. However, the simulations in the present study were still simplified in aspects of the number of RSNs (i.e., three clusters) and the numbers of nodes within each RSN (i.e., one, two, and three in three clusters, respectively). Another limitation is the assumption of stationary independences among three simulated clusters, while dynamic functional connectivity has been suggested in previous studies (Chen et al., 2013; de Pasquale et al., 2010). The efforts of simulations in the present study were aimed mainly for the comparison between VW-SSI and MNE, as well as to provide a reference for the comparison of VW-SSI and MNE in experimental data. While the present study used fMRI data as references, it should be noted that RSNs identified from EEG might be

intrinsically different from fMRI RSNs since EEG and fMRI measure distinct signals generated by different physiological processes with the human brain and human brain networks (Brookes et al., 2011b; Yuan et al., 2012b). The use of fMRI RSN templates as references (Yeo et al., 2011) because the ground truth of RSNs for EEG is unknown and fMRI data are the best available references so far.

In the present study, we studied a new computational framework for the reconstruction of EEG RSNs by implementing a new sparse source imaging algorithm for the ISI step. The new framework yielded significantly enhanced reconstructions of spatial features of RSNs. It also showed improved accuracies in reconstructing large temporal fluctuations and their amplitudes, while its performance in catching the temporal patterns of fluctuations on smaller timescales needs to be further improved.

6 Assessing EEG Resting State Networks Changes in Different Conditions

6.1 Introduction

In the previous chapters, we have developed and improved the computational frameworks for the reconstruction of EEG RSNs from multiple perspectives, including the data-driven method, the statistical analysis, and the ISI method. The proposed frameworks have been demonstrated to be effective, accurate, and robust to identify different RSN characteristics such as the spatial pattern and the power spectra. The findings revealed by these frameworks inform our understanding of the mechanism of the human brain function and organization during the resting state. Despite the significance of the findings, an attractive proposition for these studies is to reveal the potential of RSNs in the diagnosis of neurological disorders, which requires assessing RSNs in different conditions, e.g., healthy controls and patients. However, previous studies in this dissertation mainly focused on detecting RSNs of healthy participants but did not comprehensively investigate the frameworks' capability of assessing RSN alterations of diseased persons. This study aims to probe RSNs in different conditions using the computational frameworks discussed in the previous studies, which investigates the capability of these frameworks in clinical conditions.

Recently, a growing interest has been drawn to assessing RSN alterations in different conditions, which is partially due to recent findings showing that conditions, e.g., disease and age, may modulate specific RSNs (Bassett et al., 2012; Brookes et al., 2018; Cao and Slobounov, 2010; Chen et al., 2016). Specifically, by comparing between healthy controls and patients, previous studies have reported the alternations of RSNs in

different neurological disorders, such as Alzheimer's disease (Agosta et al., 2012; Sorg et al., 2007) and epilepsy (Pereira et al., 2010; Voets et al., 2009). These studies mainly used seed-based connectivity analysis (SCA), which needs pre-selection of regions of interest based on some prior knowledge. However, the selection of seeds confines the findings of SCA to a limited number of brain nodes or regions, limiting its potential in revealing RSN differences beyond prior knowledge. Other than SCA, independent component analysis (ICA) is another important and popular method to study RSNs, in particular, the spatial feature of RSNs. All studies in this dissertation employed ICA to investigate RSNs from EEG data. In contrast to the SCA, ICA is data-driven and does not require *a priori* structural knowledge. Despite its advantages over SCA, ICA has rarely been used to assess RSNs in different conditions.

In the study of Chapter 4, we conducted comparisons of RSNs between healthy controls and patients of a balance disorder, aiming to find RSN differences that may be explained by the disorder. That research, however, was limited by the number of subjects, i.e., seven patients vs. seven healthy controls, which led to insufficient statistical power of the results. Moreover, the RSN differences had not been systematically interpreted or quantitatively assessed, which limited the understanding of the RSN changes. Therefore, a further study with larger sample sizes and comprehensive investigations is needed to draw valid conclusions on the RSN differences.

In this chapter, data reflecting different conditions (i.e., a neurological disorder and the symptom severity) are analyzed together in a previously reported ICA-based framework (Li et al., 2018), aiming to obtain the RSN difference between conditions (e.g., healthy vs. patients) and the relationship between RSNs and condition levels (e.g. the

symptom severity). Simulated EEG data are used to test the framework and provide quantitative evaluation of the outcome. Moreover, experimental data from twenty healthy controls (HCs) and twenty patients with a balance disorder were employed to further assess its performance in terms of detecting of potential biomarkers. We test two hypotheses: 1) The proposed framework can detect RSN differences between different conditions, which are associated with changes in the functional connectivity in networks. 2) Different levels of conditions (such as diseased conditions) are significantly correlated with different levels of RSN changes, and such a relationship can be detected using the proposed framework. Here, both different conditions and different condition levels were considered in the investigation of RSN changes. To the best of our knowledge, this is the first study to provide extensive and quantitative evaluations of RSN changes using ICA-based frameworks, regardless of the employed neuroimaging technique.

6.2 Materials and Methods

6.2.1 Assessing RSN Changes in Different Conditions

The computational framework to assess RSNs was built upon previously reported frameworks (Ding et al., 2014; Li et al., 2018; Yuan et al., 2016) with minor modifications. As a result, the framework needed to reconstruct RSNs from EEG data in the first place, which was followed by the comparison of different conditions and the detection of relationship between RSNs and different condition levels.

Reconstruction of RSNs: First, in order to conduct subsequent analyses on the cortex, the sensor-space EEG data were mapped to the source space using the minimum norm estimation (MNE) (Hamalainen and Ilmoniemi, 1994). Then, Hilbert envelopes of

the source-space data were calculated and normalized using a z-transform in order to reduce inter-individual variations (Brookes et al., 2011b). Afterward, the normalized envelopes from different conditions were concatenated in the temporal domain. Specifically, in the comparison of different conditions, data of two conditions (e.g., HCs and patients) were analyzed together regardless of the difference of condition levels (e.g., the symptom severity of patients). In the detection of relationships, the condition level was taken into consideration in subsequent analyses. After obtaining the group-level data, the Infomax ICA (Lee et al., 1999) from the EEGLAB toolbox (Delorme and Makeig, 2004) was applied to the data to obtain multiple independent components (ICs).

After the ICA, statistical correlation analysis (Li et al., 2018) was applied to all ICs as described below. First, correlation coefficients (CCs) between the time course of each IC and the time course of each source on the cortex were calculated for all individual participants in the group. CC values of each source point were further converted into the z-value using the Fisher's z-transformation, resulting in normalized correlation values, termed as independent component correlation (ICC). After obtaining ICC maps from all individuals, ICC maps were then smoothed by an iterative smoothing algorithm, i.e., the heat kernel smoothing with Full Width at Half Maximum of 8 mm (Chung et al., 2005). Then, the group-level maps were calculated by averaging across participants (Alexander, 1990; Silver and Dunlap, 1987) with autocorrelation used to correct the degree of freedom (Bartlett, 1935). To provide a statistical definition of brain regions from these ICs, the averaged correlation maps were further thresholded by applying a source-wise t-test against zero to ICCs from all participants. The significance level was set at $p < 0.01$, and significant source nodes were kept to form clusters on the cortex. To address the multiple

comparison problem, a cluster-based correction method was employed (Hagler et al., 2006) to remove small clusters in order to reduce false positives. The t-test and the cluster-based correction resulted in binary masks to represent the significant regions of each ICC. By applying the binary masks to the averaged ICC maps, thresholded ICC maps were obtained.

Comparison of RSNs: One of the aims of this study was to compare RSNs in different conditions. To detect regions with significant differences, a two-tailed t-test was performed to compare ICC of each source between two conditions. The t-test was repeated across all source points in all ICs, generating maps showing significant differences between two conditions ($p < 0.01$). The multiple comparison problem was solved by the cluster-based thresholding as described above. Because the spatial region of each IC was defined using a binary mask in the previous step, the difference maps were further thresholded by the corresponding masks in order to reject differences that were not significant in the derived RSNs.

Detection of Relationships: Another important aim of this study is to detect the relationship between RSNs and different condition levels. To detect regions with significant relations, ICCs were plotted as a function of condition levels, i.e., functional connectivity (see Section 6.2.2) or symptom severity (see Section 6.2.3). Relationships between ICCs and covariates were tested through a model fit, in which a linear model was employed to regress condition levels against ICCs across all source nodes. With the significance level at $p < 0.01$, regions with significant relationships were detected. The cluster-based thresholding (see Reconstruction of RSNs) was adopted to control the false

positive rate. Similar to the previous section, the significant maps were spatially filtered using the binary masks that defined the region of RSNs.

6.2.2 Simulation Protocols

In order to quantitatively evaluate the performance of the proposed framework, a simulation with multiple iterations was proposed. To meet the data requirement of the proposed framework, i.e., different conditions and condition levels, networks with different connectivity but the same spatial distributions were simulated. Therefore, two datasets with different connectivity can be used to test the capability of comparisons, and multiple datasets with different connectivity can be used to examine the detection of relationships.

To simulate a network consisting of distributed brain regions, two source regions with the diameter of 20 mm were placed on the cortical surface as shown in Figure 6.1B, and they are fixed across simulations. The time courses of the two sources, which were randomly generated in each simulation, were modeled as amplitude-modulated signals including the envelope and the carrier signal. The connectivity between two sources was reflected in the envelope while the carrier signal was employed to mimic the fast dynamic of brain activity. The sampling frequency of the signals was 150 Hz, and the duration was 2 minutes. In order to simulate different connectivity between two sources, the envelope was divided into non-overlapping 4-second windows, in each of which envelopes of two sources were either same (i.e., correlation coefficient = 1) or independent (i.e., correlation coefficient = 0) (Figure 6.1A). The proportion of same envelopes, P_I , varied across simulations, ranging from 0 to 1 with the step of 0.1. The envelope in each window was generated using the protocol reported by Ramkumar, Parkkonen et al (2014) (Ramkumar

et al., 2014), which has also been described in Chapter 5.2.3. In brief, the envelopes were generated by convolving Gaussian functions with binary spike trains. After obtaining the envelopes for all thirty windows, carrier signals, which were sinusoids with 8 Hz for the left source and 10 Hz for the right source, were multiplied with the envelopes. In order to mimic brain noise on the cortical surface, pink noises were added to the whole cortical surface (Ramkumar et al., 2014) with the standard deviation (SD) of the noise 10% of SD of simulated signals. Afterward, the simulated cortical signals were mapped to sensor space by multiplying the lead field (see Section 5.2.3). Finally, Gaussian white noises with an SD 5% of the averaged SD of sensor-space signals were added to simulate measurement noises. For a specific P_I , the simulation was repeated 50 times, each time with fixed source regions but randomly generated time courses. The simulation provided 550 datasets, D_p (where the subscript $p = P_I$), which are subject to the following analysis.

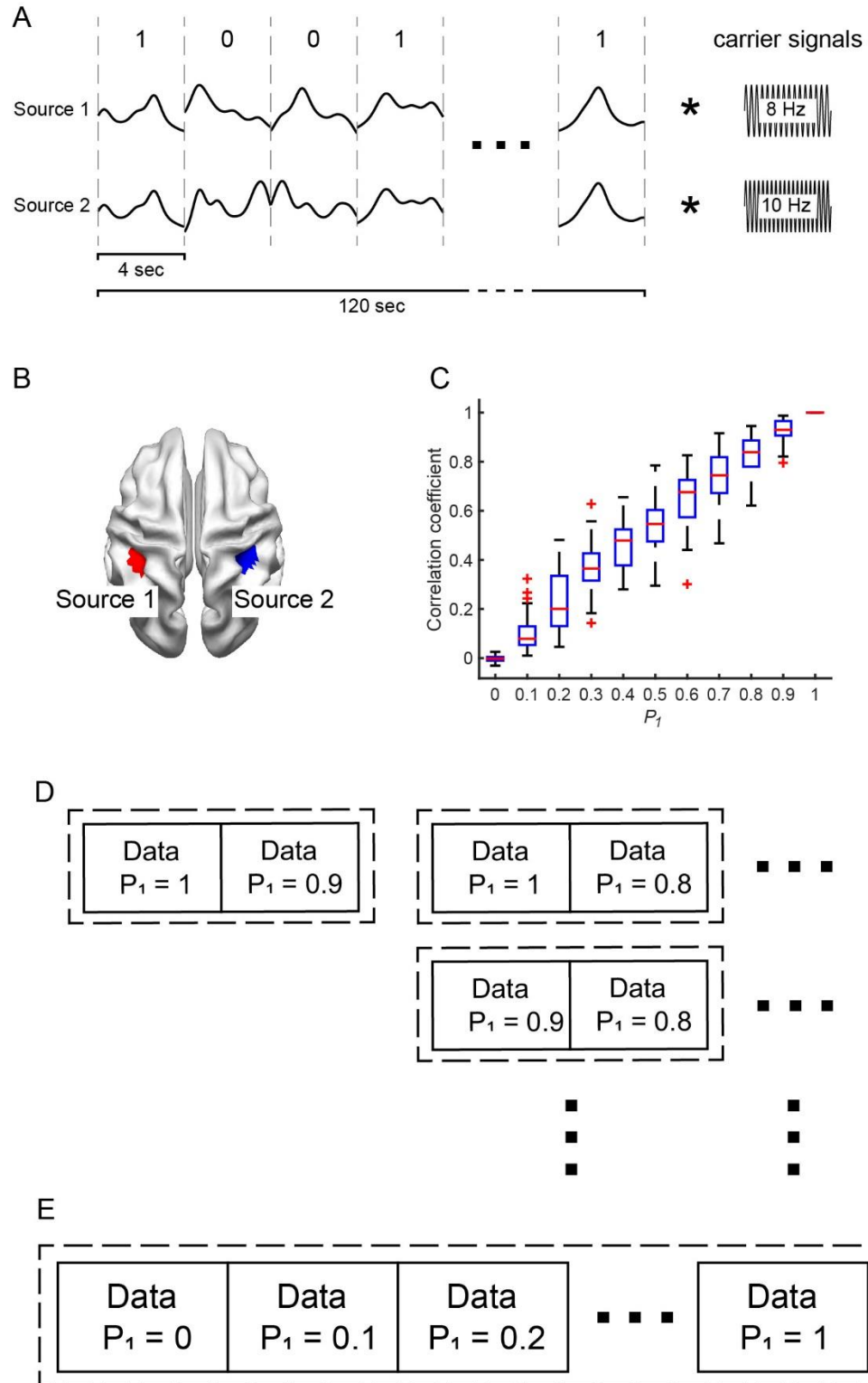


Figure 6.1 Schematic of the simulation

(A) Envelope and carrier signals of simulated time courses. (B) Source locations (C) Connectivity at different P_1 . (D) Concatenation of data for the comparison (E) Concatenation of data for the detection of relationships

6.2.3 Experimental Data

Twenty healthy controls (HCs) (all females; age: 48.8 ± 7.2 years) and twenty patients (all females; age: 51.8 ± 12.5 years) of mal de débarquement syndrome (MdDS) (Cha et al., 2012; Ding et al., 2014) participated in this study, which was approved by Western IRB (www.wirb.com). All participants have been fully informed about the study and have signed the informed consent form before the experiment.

A 126 channel EEG system with a BrainAmp amplifier (Brain Products GmbH, Munich, Germany) was used in the present study. The ground electrode was placed at AFz in the international 10-20 system, and FZ was chosen as the reference channel. Resting-state recordings were obtained for five minutes for each participant while they were asked to keep still and have their eyes closed. For each participant, structural MRI data were obtained using a 3D MPRAGE sequence (124 contiguous axial slices with 1.2 mm slice thickness; matrix size = 256×256 ; FOV = $220 \text{ mm} \times 198 \text{ mm}$; TR/TE/TI/TD = $5 / 1.98 / 725 / 1400$ ms, flip angle = 8 degree; sampling bandwidth = 31.25 kHz, SENSE acceleration = 2). Other than EEG and structural MRI recordings, patients of MdDS rated the degree of their symptoms on a visual analogue scale (VAS) of 0-100, where 0 indicated free of rocking sensation. Here, VAS represented the symptom severity which would be used as covariates in subsequence analyses.

6.2.4 Analysis and Evaluation Protocols

Simulation: The simulation aimed to determine whether the proposed framework can detect the connectivity difference. To evaluate this capability, two datasets, D_i and D_j (where $i > j$), were concatenated and analyzed using the proposed framework, with three ICs generated (Figure 6.1D). In order to select the IC corresponding to the simulated

sources, spatial and temporal correlation coefficients (CCs) were calculated between the ICs and the simulated sources. The IC with the highest sum of spatial and temporal CCs was chosen as the reconstructed network. Because only a single dataset was selected in either condition, statistical comparisons cannot be conducted in each simulation. Consequently, the proposed framework cannot be used to localize the difference. However, since regions with different connectivity were already known (i.e., the simulated sources), ICCs in the simulated regions were compared in the analysis of each simulation. By repeating the comparison 50 times, ICCs in the simulated regions can be statistically compared between two conditions using a paired t-test, with the significance level at $p < 0.05$. Since different connectivity was simulated and every two datasets with different connectivity could form a comparing pair, all possible pairs were compared using the above method, resulting in 55 comparisons.

The simulation also aimed to test the relationship between ICC and connectivity. To evaluate this capability, 11 datasets, D_i (where $i = 0, 0.1, 0.2, \dots, 1$), were selected and analyzed using the proposed framework, with three ICs generated (Figure 6.1E). The selection of ICs followed the same strategy as described above. Also, the ICCs in the simulated region were averaged to generate the averaged ICC which was used as the covariates for the model fit. In the analysis of each simulation, a linear regression was conducted between averaged ICCs and P_l 's, with the significant level at $p < 0.001$. This was repeated 50 times and the times with significant relationship were summarized to evaluate the performance.

Experiment: After obtaining resting-state EEG data, data were pre-processed with an established pipeline including rejection of bad segments, interpolation of bad

channels, and re-reference to common average. Then data were down-sampled to 250 Hz and band-pass filtered from 4 Hz to 30 Hz. ICA was used to remove artifacts caused by movement, eye movement, and noise (Ding et al., 2014).

The preprocessed data from twenty healthy controls (HCs) and twenty MdDS patients were concatenated and processed using the proposed framework, with 40 ICs generated. RSNs were selected from the ICs according to their spatial features such as spatial distributions and spatial coverages, with fMRI RSN templates as references (Yeo et al., 2011). In the comparison of two conditions, i.e., HCs vs. patients, the patients' symptom severity, i.e., VAS, was not taken into account. Hence, HCs were treated as the control condition while all MdDS patients were treated as the comparison condition. In the detection of relationships, only ICC maps from the MdDS patients were considered, and a linear regression was performed between ICC and VAS of the patients.

6.3 Results

6.3.1 Simulation

To evaluate the framework, networks with different connectivity were simulated. To simulated different connectivity, the time courses were divided into multiple windows with the binary state, i.e., identical or independent. Figure 6.1C shows the relationship between connectivity and P_I 's. It can be observed that increased P_I is associated with increased connectivity. Meanwhile, for each P_I , variation of connectivity can be observed, which may be explained by the randomization of envelopes.

The comparison of simulated data contained 55 possible pairs, each of which included 50 iterations. Figure 6.2A illustrates six examples of the comparisons. Each plot represents the information of two paired conditions. The bar plots show the mean and the

standard deviation of ICCs in the simulated sources, and the spatial patterns show the corresponding ICC maps. In the spatial patterns, relatively higher ICC can be observed around the simulated sources. In the comparison of ICCs, differences were detected between two compared conditions. In general, the condition with higher P_I exhibited higher ICCs. One exception in the fourth example in which $P_I = 0.5$ shows higher ICCs than $P_I = 0.8$.

Figure 6.2B shows the summary of 50 simulations. The left figure illustrates the mean and standard deviation of ICCs for one condition, and the right figure shows the same information for the second condition. The color represents the amplitude of the mean. It can be observed that ICC increased with P_I for both conditions regardless of the P_I of the compared condition. Also, for the same P_I , the averaged ICCs are relatively consistent, with small variations observed. The result of the statistical analysis over 50 simulations is displayed in Figure 6.2B. Among all 55 pairs, differences can be significantly detected in 54 pairs. The condition with higher P_I exhibits higher ICC than the condition with lower P_I . The pair of $P_I = 0.5$ and 0.4 does not show significant difference but reaches a p -value of 0.079.

Figure 6.3A shows five examples out of 50 simulations of the linear regression. The bar plots show the mean and standard deviation of ICCs in the simulated sources, and the spatial patterns depict the ICC distributions over the cortex. In each bar plots, the blue line represents the best fit of linear regression, which is significant ($p < 0.01$). All 50 simulations exhibit significant linear relationship at the significance level of $p < 0.01$.

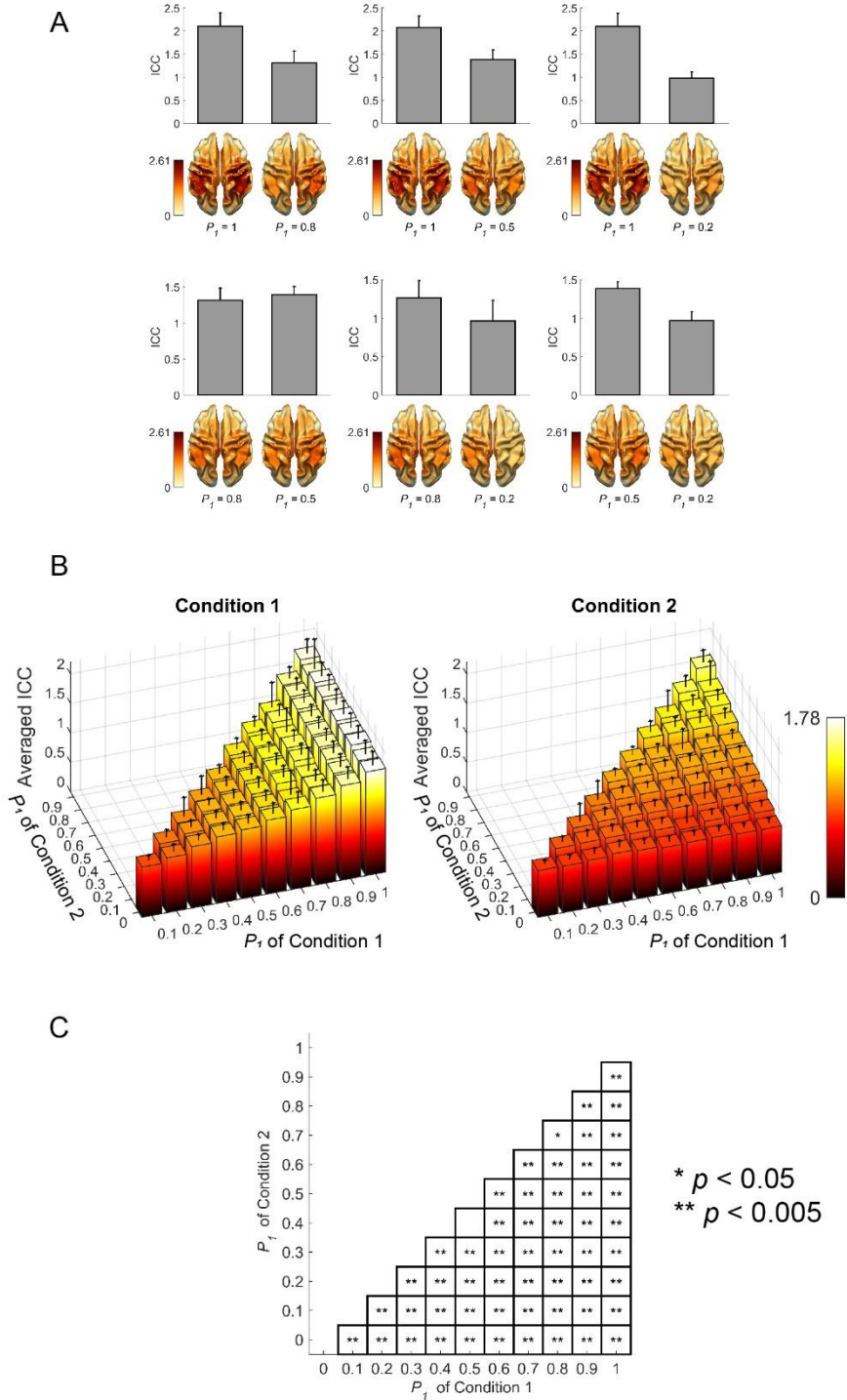


Figure 6.2 Simulation results of comparisons
 (A) Six examples of comparisons. (B) Bar plot of ICCs in two conditions in 50 simulations. (C) T-test results of all 55 pairs. * $p < 0.05$; ** $p < 0.005$

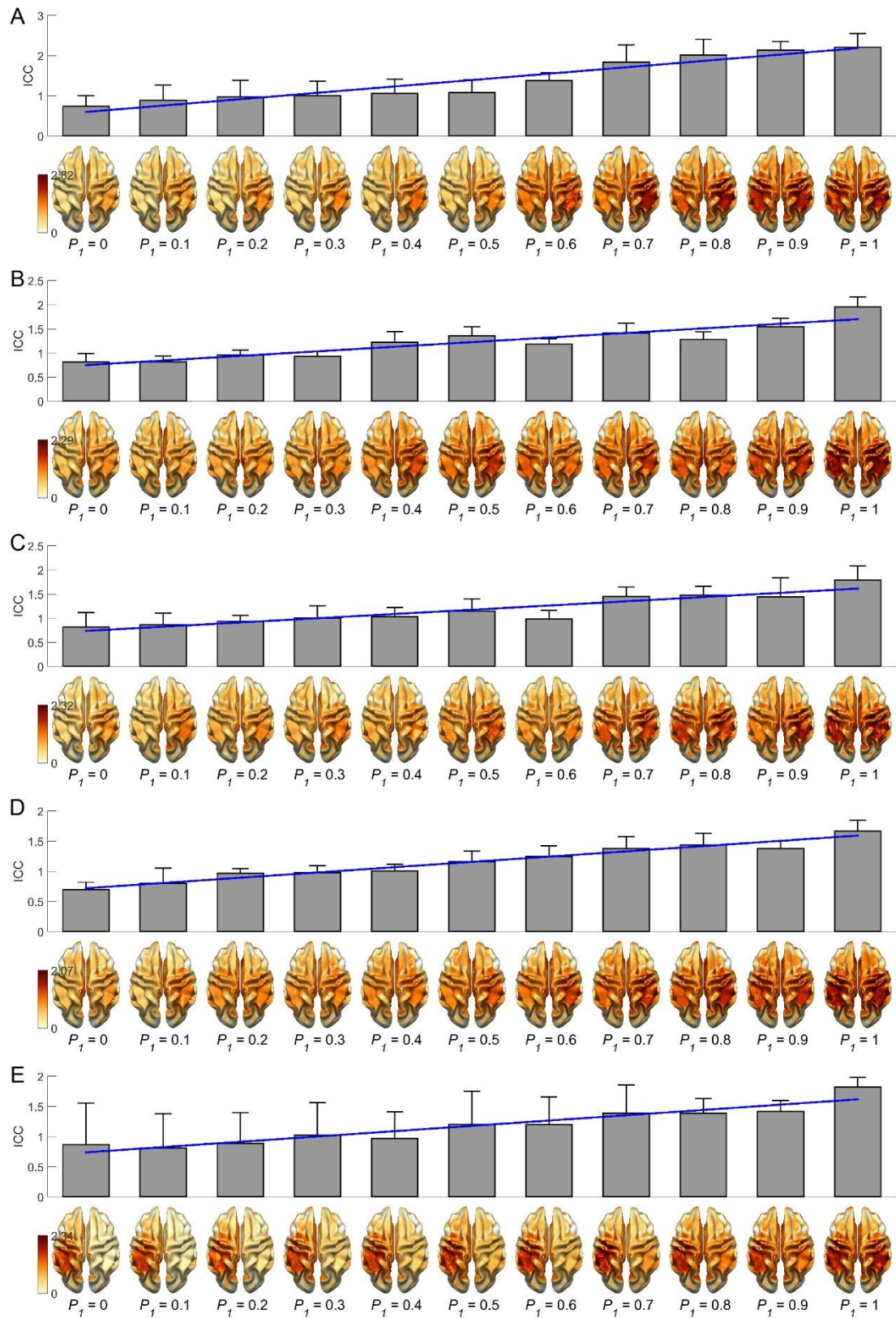


Figure 6.3 Examples of Simulation Results of linear relationships

6.3.2 Experiment

Spatial Patterns of RSNs: Before assessing RSNs in different conditions, it is necessary to obtain spatial patterns of RSNs. Figure 6.4A-E illustrates spatial patterns of identified RSNs from the experimental data including both HCs and MdDS patients. The spatial patterns were further categorized into five groups, i.e., visual, auditory, somatomotor, frontoparietal, and default mode networks. For each group, multiple RSNs are selected according to their spatial distributions.

In the selected RSNs, four, four, four, three, and five RSNs were selected for the five classes of RSNs, respectively. As shown in Figure 6.4A-E, these spatial patterns are remarkably similar to fMRI RSNs templates. Also, their spatial features are in agreement with the results in previous chapters. Specifically, both bilateral (e.g., V-1) and lateralized (e.g., V-2) patterns can be observed in each RSN class. Moreover, some show the hemispheric dominance whereas the similar dominance can be found on their symmetric hemisphere in other corresponding RSNs. For example, M-1 and M-2 are dominant on the motor cortex of one hemisphere, but their spatial patterns are symmetric. In all five classes of RSNs, the DMN exhibit the most complicated spatial features. Different brain regions, including the prefrontal cortex, the parietal cortex, and the posterior cingulate cortex (PCC), are covered by multiple components.

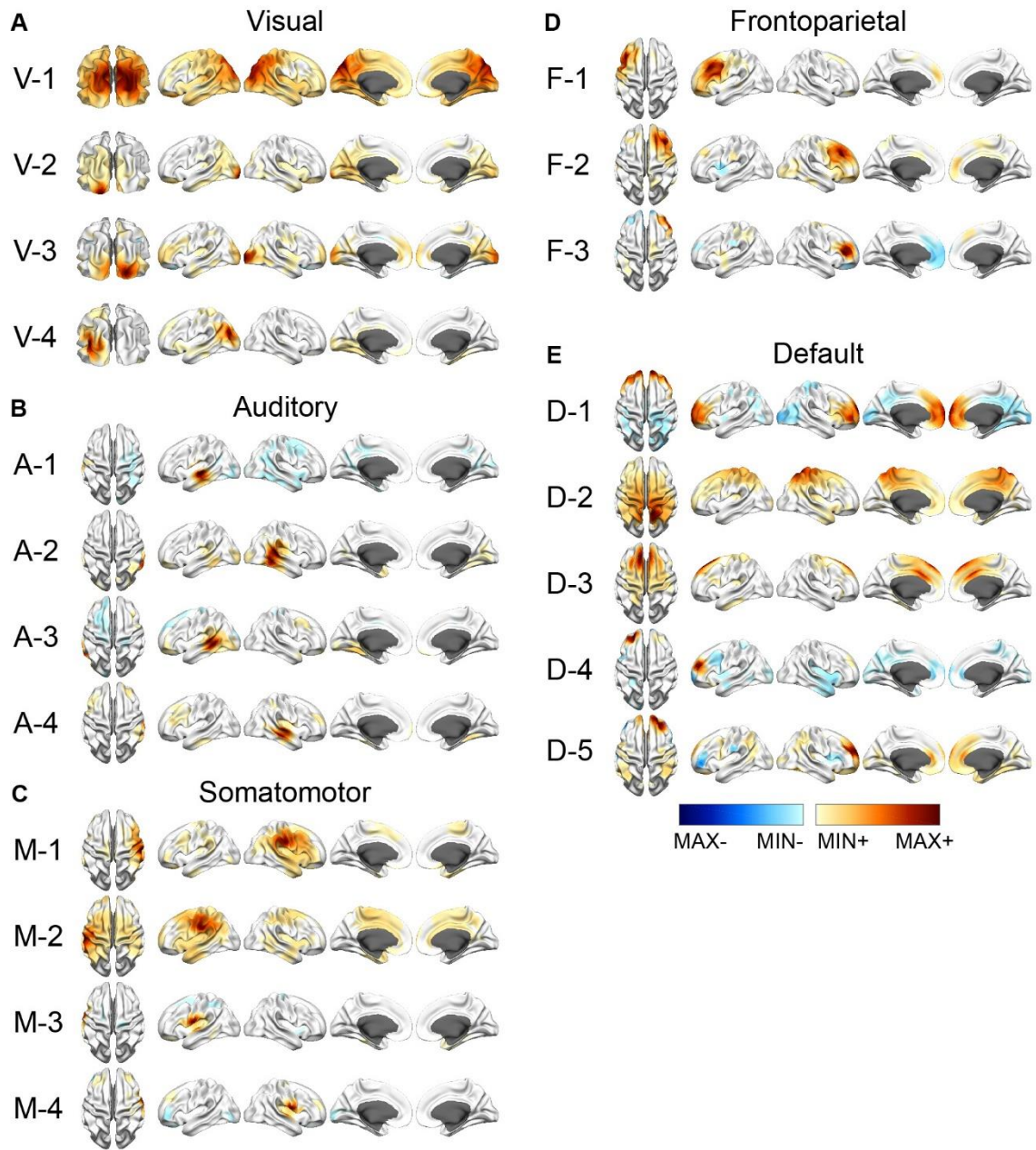


Figure 6.4 Spatial patterns of RSNs

(A) Visual. (B) Auditory. (C) Somatomotor. (D) Frontoparietal. (E) Default.

Comparison of RSNs: The framework was used to compare all derived RSNs of HCs and MdDS patients. Four RSNs show significant differences as shown in Figure 6.4, including V-2, V-3, A-1, and D-5 (Figure 6.5). The spatial patterns show the regions and the difference values of the detected differences. The blue color represents that the ICC

is lower in MdDS patients. The bar plot shows the mean and the standard deviation of ICCs in corresponding regions. All five results show decreased ICC in the patient group. Specifically, in the two visual subnetworks (i.e., V-2 and V-3), significantly lower ICCs are detected in the right primary visual cortex. In the auditory network (i.e., A-1), significantly lower ICCs are detected in the left auditory cortex and left inferior motor cortex. In the DMN (i.e., D-5), significantly lower ICCs are detected in the inferior parietal lobe (IPL). Although some RSNs cover multiple regions (e.g., D-5), significant differences are only detected in one of the regions instead of all regions.

Relationship between ICC and VAS: Figure 6.5 shows the five RSNs with significant linear relationships between ICC and VAS, including one auditory network, one sensorimotor network, and three DMNs. The spatial patterns show the brain regions and the fit parameter of significant linear relationships. Red represents that VAS increases when ICC increases; blue represents that VAS decreases with reduced ICC. In the auditory network (i.e., A-2), a negative linear relationship is found in the right auditory cortex. In the auditory network (i.e., A-2), a negative linear relationship is found in the right auditory cortex. In the sensorimotor network (i.e., M-3), a positive linear relationship is found in the left motor cortex. The three DMNs exhibit distinct linear relationships: D-1 shows a positive linear relationship in three areas in the prefrontal cortex; D-2 shows negative linear relationship; D-3 shows a positive linear relationship in the right prefrontal cortex while negative linear relationship in the right tempo-parietal cortex.

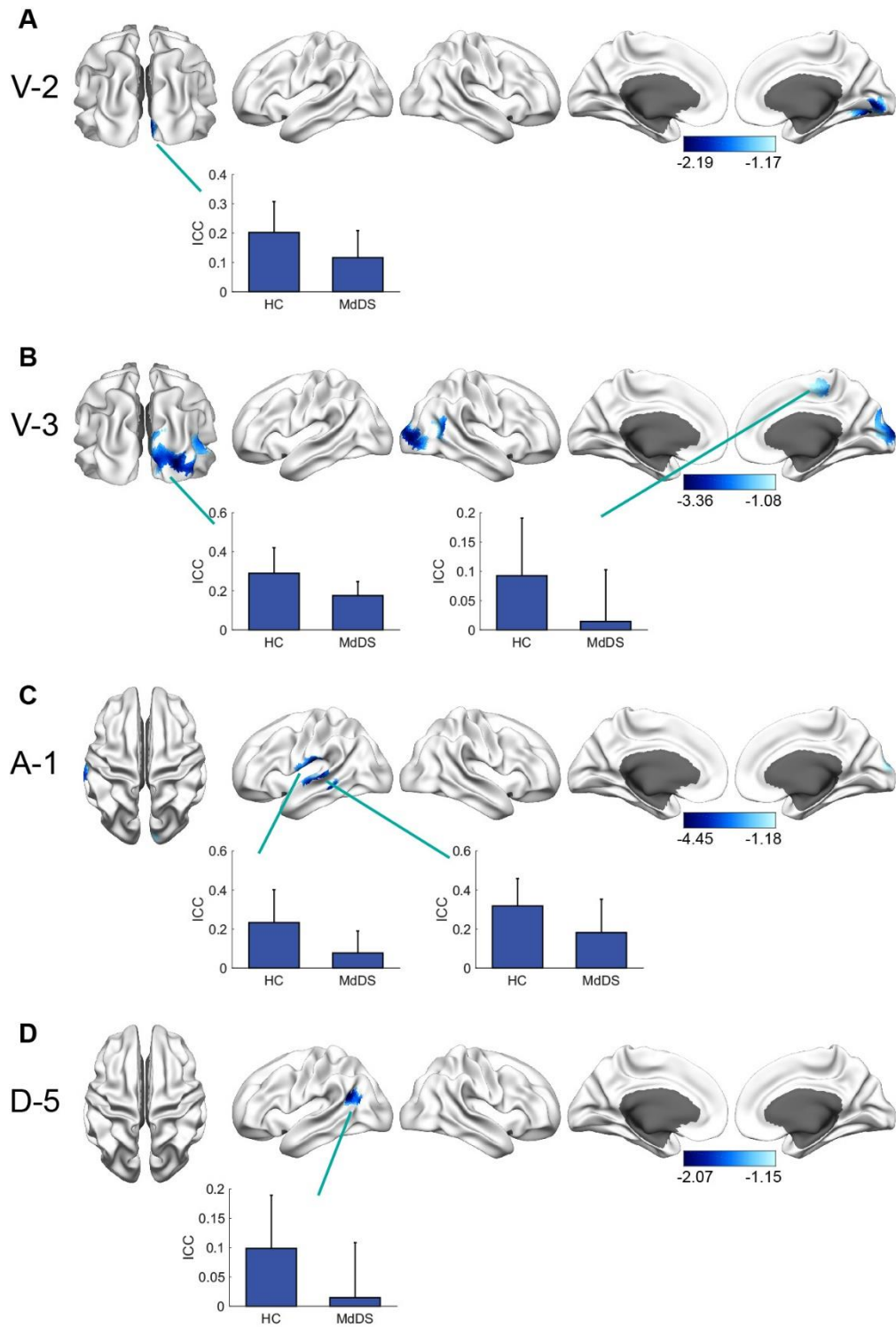


Figure 6.5 RSN differences between HCs and MdDS

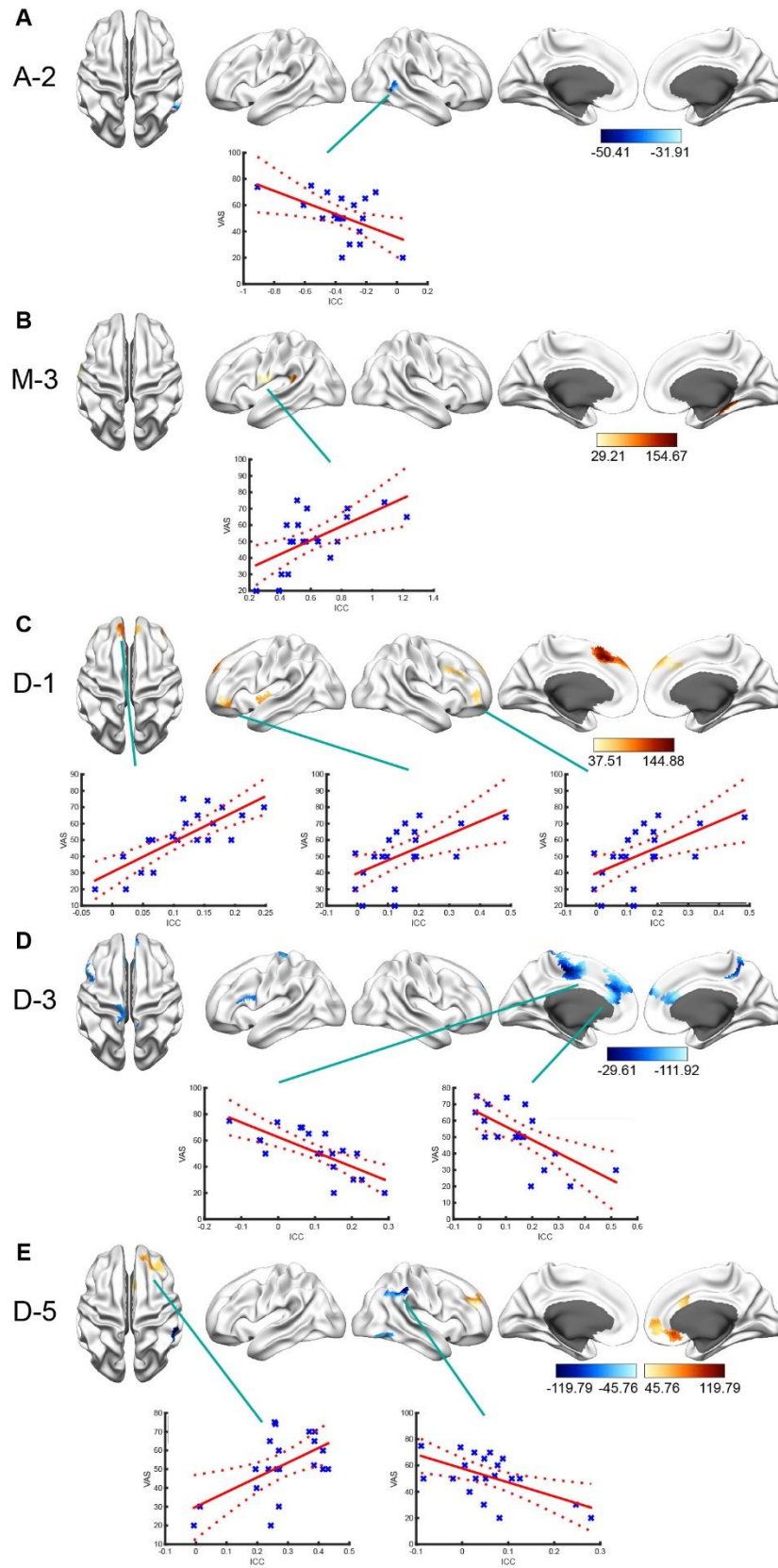


Figure 6.6 Linear relationships between ICC and VAS

6.4 Discussion and Summary

A number of recent studies have shown that the change of RSNs may reflect the alternation of conditions or the degree of quantified status, such as functional brain disorders and the degree of symptoms (Brookes et al., 2018; Buckner and Vincent, 2007; Chen et al., 2015; Fox and Raichle, 2007). The relationship between RSNs and the conditions can be characterized by assessing RSNs in different conditions or condition levels. In previous studies regarding RSN differences, RSNs are only assessed in a relatively small number of nodes, which limits the localization of RSN changes. From a methodological point of view, ICA can overcome this limitation and therefore offers more flexibility. However, ICA has been mainly used to reconstruct the spatial patterns of RSNs while its capability of comparing RSNs has not been extensively investigated. In the present study, an ICA-based framework was developed to compare RSNs from different conditions and detect underlying relationships between RSNs and participants' condition level. The framework included data from different conditions in a single implementation and statistically compared RSNs of different conditions. Its capability to assess RSNs was validated using simulated data. More importantly, using experimental data from HCs and MdDS patients, the proposed framework successfully detected RSN differences in MdDS patients and revealed the relationship between RSNs and the degree of symptoms.

MdDS is caused by exposure to oscillating environments such as a flight or a cruise, leading to a persistent sensation of rocking dizziness (Cha, 2009; Cha et al., 2012; Cha et al., 2013; Cha, 2015). It is the unnatural persistence of the natural phenomenon of motion entrainment. In the analysis of experimental data, resting-state EEG data from

patients of MdDS were used in the comparison to healthy participants. The comparison revealed reduced ICC in multiple RSNs, including the auditory network, the visual network, and the DMN. In particular, the hypo-connectivity in the left temporal cortex and in the left tempo-parietal cortex are consistent with hypo-metabolism from fMRI and PET studies regarding the same disorder, in terms of the location of the differences and the direction of changes (i.e., decreased) (Cha et al., 2012). Moreover, resting-state fMRI studies have found that MdDS patients show an increased functional connectivity in the primary visual cortex (Cha et al., 2012). The finding is in agreement with the results of visual RSNs regarding the spatial location. However, the direction of change of the two studies is the opposite, which warrant further research in the future.

Significant linear relationships between ICC and VAS have been detected in the present study. The results showed that a linear relationship exists in the prefrontal cortex (i.e., D-1 and D-3), which is consistent with the functional connectivity changes revealed by previous PET studies (Cha et al., 2012). It is noteworthy that the relationship has been found in the right temporal cortex. Although this brain area has not been reported in previous studies regarding MdDS or our comparison results, it is on the symmetric hemisphere of the results of A-1, as reported in both PET study and our comparison results. The negative fit parameter suggests that the connectivity decreases as the symptom increases. Among the five results, D-5 is the only result that has been reported in both the comparison and the linear regression. However, the significant regions are different in two analyzes. Specifically, the left posterior cortex was reported in the companion while the right prefrontal cortex and the right posterior cortex were reported in the linear regression. Moreover, the fit parameters for the two brain regions were

different, indicating the symptom may have an opposite effect on the connectivity in different regions.

In this study, the comparisons and the linear regressions are both based on ICC, which represents the correlation between the IC activation and the envelope of sources. The implementation of ICA is based on the assumption of stationary functional connectivity in RSNs (Brookes et al., 2011b). Therefore, the time courses of ICs represent the common activations of networked regions. By calculating the correlation coefficients between the common activation and the actual activation, ICC indicates the proportion of the common activation, which further reflects the strength of connectivity. This inference is supported by the results of the simulation, in which ICC increases with the increasing connectivity. Hence, ICC can be used as an indicator of the functional connectivity.

Notably, the quality of results from the simulated data and the experimental data is distinct. Specifically, the simulation results revealed bilateral areas of the simulated sources, while most of the experimental results only showed a single area. This can be explained by the simplicity of the simulation. In the simulation, we only simulated one network with two interconnected sources. Although noise was added to mimic the realistic recordings, the simulation cannot represent the real RSNs, which include multiple networks with complicated connectivity. On the other hand, the comparison of experimental data was confined by the spatial patterns of reconstructed RSNs (see Section 6.2.4), which exhibited dominance in a single area. This problem has been observed in our previous studies (Li et al., 2018; Li et al., 2017), and it can be explained by the fast sampling frequency of EEG and the dynamic of RSNs. Taken together, the complexity

of real RSNs causes the limitation of the results, which warrant further investigations in the future.

In summary, a computational framework was used to compare RSNs in different conditions and detect relationships between RSNs and condition levels. A major advantage of this framework is that it provides more flexibility in the detection of RSN differences or relationships, which allows us to find the contrast in the whole brain. This study paves the way for further research assessing the relationship between RSNs and neurological disorders. It also sheds new light on the potential of RSNs in clinical diagnosis and evaluation.

7 Discussion and Conclusion

Resting state networks (RSNs), which reflect the intrinsic functional architecture of the human brain, have drawn growing research interest to probe their neurophysiological underpinning (Finn et al., 2015; Hipp et al., 2012; Yuan et al., 2016). To date, several studies have developed different computational and analytical frameworks to characterize RSNs using the technique of EEG, with interesting features of RSNs revealed from multiple perspectives (Ding et al., 2014; Liu et al., 2017; Yuan et al., 2016). These studies, however, have limitations that require further studies. Therefore, there is abundant room for more research effort and further improvement.

This dissertation presents novel frameworks that overcome some of the limitations of current frameworks used to investigate RSNs using EEG. The proposed frameworks are illustrated and evaluated in different studies, with each study focusing on solving one or two limitations. First, the study in Chapter 3 reported that studying RSNs in the source space can provide accurate estimations of RSNs. This finding provides an important direction for the frameworks in later studies. Second, the study in Chapter 4 develops a new computational framework to provides insights into the spatial and spectral characteristics of RSNs. Third, the study in Chapter 4 improves the spatial definition of RSNs by applying new statistical correlation analysis to spatial patterns of RSNs. Fourth, the study in Chapter 5 uses an advanced ISI method to improve the RSN reconstruction accuracy. Although the studies are illustrated separately in each chapter, their development and invocation are largely interdependent. In this chapter, some discussion of the proposed frameworks is provided to highlight the significance of each contribution

and summarize limitations to my studies and provide important directions for further research.

7.1 Summary of the Findings

RSNs can be reconstructed either in the sensor space, i.e., the scalp surface, or in the source space, i.e., the cortex (Ding et al., 2014; Liu et al., 2017; Yuan et al., 2016). Surprisingly, little research has compared the quality of reconstructed RSNs in the two spaces to determine an optimal option to generate more accurate RSNs. In the study of Chapter 3, the performances of the sensor-space ICA (i.e., using ISI after ICA) and the source-space ICA (i.e., using ISI before ICA) in deriving RSNs were compared using both simulated and experimental data. Notably, this is the first study to our knowledge to investigate performance differences between these two ICAs. Both compared frameworks used identical ISI and ICA methods, while the only difference is the sequence to apply ISI and ICA. The results from simulated data showed that the source-space ICA achieved significantly better ($p < 0.01$) spatial and temporal feature estimations. For the real data, spatial patterns from the source-space ICA exhibited higher spatial similarity to the fMRI RSN templates. These findings suggest that analyzing RSNs in the source space (i.e., ISI then ICA) is preferable in computational frameworks for RSNs because it can provide more accurate estimations of RSNs. This study, therefore, determines the sequence to use ISI and ICA in later studies.

To reconstruct RSNs from the data in the cortical space, a larger number of studies have used ICA as the primary tool in computational frameworks (Brookes et al., 2011b; Liu et al., 2017; Sockeel et al., 2016; Yuan et al., 2016). In previous studies, ICA is used to detect RSNs under the assumption of either spatial independence, i.e., spatial ICA, or

temporal independence, i.e., temporal ICA. In the study of Chapter 4, we propose a new type of ICA, time-frequency ICA (TFICA), for the reconstruction of RSNs. In TFICA, the temporal data are firstly transformed into time-frequency representation using STFT. Then, ICA is applied to the transformed data to derive components that are statistically independent in the time-frequency domain. The aims of the new method are threefold. First, the transformation by STFT makes the components non-Gaussian distributed, which meets the mathematical principle of ICA (Hyvärinen and Oja, 2000). Second, the transformation by STFT reduces the computational loads for ICA. In our study, the temporal data from one second contain 250 sample points, while in STFT, only 27 sample points are selected to represent the spectra from 4 to 30 Hz. Hence, the data for ICA are largely down-sampled. Third, the usage of STFT brings the spectral domain into RSN analysis. The spectral analysis was mostly achieved by applying a band-pass filter in earlier studies (Hipp et al., 2012). In contrast, TFICA provides an efficient way investigation of spectral features over a broad frequency band.

The identification and characterization of RSNs were mostly based on the group-level analysis (Ding et al., 2014; Liu et al., 2017; Yuan et al., 2016). Previous studies overlooked the critical role of group-level statistical analysis after ICA, making the results lack statistical meanings. In the study of Chapter 4, we propose statistical correlation analysis to process the ICA output. In statistical correlation analysis, subject-specific spatial patterns are obtained to represent the spatial feature of RSNs at the individual level. Then, spatial patterns are averaged and statistically thresholded. The averaging step reduces the influence of inter-subject variance, which has not been taken into consideration of in prior studies. The statistical thresholding, which is achieved by the

voxelwise t-test, refines the spatial localization of RSNs. In addition, the effect of autocorrelation on generating false cross-correlations has been considered in the study, as in resting-state fMRI studies (Honey et al., 2009; Rombouts et al., 2005; Roy et al., 2009; Woolrich et al., 2001). This is particularly important for EEG RSN since the oscillatory nature of EEG signals suggests potentially high autocorrelations. Moreover, a cluster-based thresholding technique was used to address the multiple comparison problem. Its implementation in EEG RSN estimations is new and distinct in terms of the data domain, and it provides an alternative solution to the conservative Bonferroni correction for multiple comparisons.

The statistical correlation analysis proposed in Chapter 4 also extends the capability of ICA-based frameworks. RSNs from participants in different conditions, e.g., healthy control and patients of MdDS, are compared to detect contrast differences, which is achieved by performing a t-test on subject-specific spatial patterns of different conditions. The significant differences revealed by our study are consistent with the findings observed in previous literature in terms of locations and directions of changes (Fox and Raichle, 2007; Jao et al., 2013; Marx et al., 2004; Raichle et al., 2001; Yang et al., 2007). Importantly, this method is data-driven while previous studies have widely used SCA, which requires pre-selection of regions of interest. Therefore, the statistical correlation analysis shed new light on the detection of RSN differences induced by different conditions (tasks, neurological disorders, brain injuries, etc.).

ISI plays a critical role in current computational frameworks for EEG RSNs. The performance of ISI can substantially affect the reconstruction of RSNs. Despite the development of studies regarding EEG RSNs, little progress has been made in improving

ISI, and only conventional ISI methods such as minimum norm estimation (Hamalainen and Ilmoniemi, 1994) have been used in previous frameworks. In the study of Chapter 5, a novel inverse source imaging method, termed as variation and wavelet based sparse source imaging (VW-SSI), is used in the ISI step of the framework, aiming to improve the reconstructed RSNs. This modification was evaluated by comparing with the framework using conventional MNE. Results from both simulated and experimental EEG showed that VW-SSI improves the accuracy of spatial estimation. These findings suggest that the reconstruction of RSNs can be advanced by the development of ISI methods. On the other hand, the temporal estimation by VW-SSI does not give better performance than MNE. This is an important issue for further research because the temporal feature is a crucial aspect of RSNs.

One major aim of the proposed frameworks is to reconstruct the spatial patterns of RSNs. In all the studies in this dissertation, spatial patterns were obtained for different classes of RSNs, including visual, auditory, somatomotor, frontoparietal, and default mode networks. The spatial patterns of these identified RSNs indicate high spatial similarity to RSN templates from fMRI (Yeo et al., 2011), as well as to fMRI RSNs reported in other literature (Liu and Duyn, 2013; Richiardi et al., 2015; Smith et al., 2009; Smith et al., 2012). Moreover, spatial patterns from all the studies in this dissertation further indicate similar features across studies. Specifically, each class of RSNs (defined by fMRI) have multiple EEG RSNs. Also, regardless of the RSN class, EEG RSNs exhibit bilateral or unilateral distributions in different components. These findings demonstrate the effectiveness and robustness of proposed frameworks in identifying RSNs from EEG. The remarkable similarity between RSNs identified in fMRI and EEG supports the notion

that RSNs represent a fundamental aspect of brain physiology that can be reflected in hemodynamic and electrical brain signals.

It also should be noted that differences have been observed when comparing the spatial patterns from fMRI and EEG. A great proportion of EEG RSNs are lateralized, while fMRI RSNs exhibit more symmetric and bilateral patterns (Agosta et al., 2012; Damoiseaux et al., 2006; De Luca et al., 2006). This fact, however, does not challenge the contribution of EEG RSNs. This difference can be explained by the intrinsic differences in brain electrical and hemodynamic signals, in which EEG is more dynamic and directly linked to underlying network communication mechanisms compared to fMRI (Laufs, 2008; Mantini et al., 2007; Yuan et al., 2012a). Furthermore, bilateral patterns in fMRI might be due to the convolution from the electrical response to the hemodynamic response, which can increase correlations among different RSNs (Yuan et al., 2016).

7.2 Limitations and Future Works

A number of limitations need to be noted regarding the studies in this dissertation. First, the categorization of SCTs into RSNs was not fully quantitative and not fully objective. While fMRI templates were used, the quantitative metric, i.e., vectorized spatial correlation, and the protocol of unique matching were not optimal and, therefore, visual inspections were still used. Fully automated procedures need to be established in defining various classes of RSNs in the future. Second, our experimental data had relatively small numbers of participants and only included female participants. Some of the findings in the present study might not be generalizable to males because of the gender differences in resting states (Gur et al., 1995; Kilpatrick et al., 2006; Tian et al., 2011). The proposed frameworks need to be tested in data from a larger population with equal

gender distributions to enhance the statistical power of findings and eliminate potential gender biases. Third, no direct comparisons between our proposed framework and other existing works are performed in the present study, especially those from MEG studies (Brookes et al., 2011b; Liu et al., 2017; Nugent et al., 2015). This is because such comparisons are very complicated since our current framework involves three major components: ISI, ICA, and correlation analysis, and each component has a group of variants in their implementations. Furthermore, the statistical correlation analysis is introduced to the current framework from fMRI, which is relatively new and has not been used in EEG/MEG RSN studies (Brookes et al., 2011b; Yuan et al., 2016). Nevertheless, the comparisons with other methods will be conducted in future studies. Last, the current studies do not comprehensively explain why fMRI RSNs and EEG RSNs exhibit different spatial features to a certain degree, despite being observed in all studies in this dissertation. A quantitative investigation is required to address this issue.

In this dissertation, the proposed frameworks were mainly used to probe the spatial and spectral properties of RSNs. On the contrary, the temporal property of RSNs has not been reported in any of the studies. The lack of the temporal property is due to the spontaneous nature of RSN fluctuations. The temporal activations of RSNs can hardly be interpreted because there are no stimuli or behavioral references as found in task condition. However, recent studies have raised the notion of the temporal dynamic, i.e., the networking of RSNs is dynamic rather than stationary (Chang and Glover, 2010; Hindriks et al., 2016). This finding provides a new perspective to characterize RSNs using EEG. Importantly, it should be noted that the proposed frameworks may not be suitable for analysis of RSN dynamic because current ICA-based frameworks are under the

assumption of stationary connectivity. Therefore, further research might explore new frameworks to investigate the temporal dynamic of RSN.

7.3 Conclusion

The aim of the study was to develop, optimize and validate computational frameworks for the reconstruction of RSNs from EEG data. With both simulated and experimental EEG data, the spatial, temporal, and spectral estimations of RSNs reconstructed from the sensor space (scalp surface) and the source space were compared. The study demonstrated that the source space is preferable to generate an accurate reconstruction of RSNs. By integrating ISI, ICA, and statistical correlation analysis, we proposed a new computational framework, TFICA-SCT, for reliable and robust reconstruction of RSNs from EEG. Besides, it has also been demonstrated that TFICA-SCT can be used to detect spatial and spectral differences of RSNs induced by different conditions such as a balance disorder. Moreover, an advanced ISI method, VW-SSI, was used to replace the conventional ISI methods (e.g., MNE) in the above-mentioned frameworks, and the comparison of results demonstrated that the modification significantly improved the spatial reconstruction of RSNs. Taken all together, the proposed frameworks and analysis contribute to our understanding of the underlying electrophysiological basis of RSNs. This study not only addresses the limitations in the previous studies but also establishes new perspectives for detecting RSNs from EEG. The findings of this study extend our knowledge of the characteristics of RSNs in multiple aspects: different RSNs have distinguishing spatial and spectral patterns; neurological disorders can alter the property of specific regions of RSNs. A key strength of the present study is that all proposed frameworks are data-driven, which break the constraint of

conventional seed-based connectivity analysis. Being limited to spatial and spectral analysis, this study lacks the investigation into the temporal dynamic of RSNs due to the assumption under which the frameworks were proposed. Further studies need to be carried out in order to extend our understanding of the human brain networks. Despite its limitations, the study certainly contributes to the research methodology of EEG RSNs.

8 References

- Abou - Elseoud, A., Starck, T., Remes, J., Nikkinen, J., Tervonen, O., Kiviniemi, V., 2010. The effect of model order selection in group PICA. *Human brain mapping* 31, 1207-1216.
- Acar, Z.A., Makeig, S., 2013. Effects of forward model errors on EEG source localization. *Brain topography* 26, 378-396.
- Agosta, F., Pievani, M., Geroldi, C., Copetti, M., Frisoni, G.B., Filippi, M., 2012. Resting state fMRI in Alzheimer's disease: beyond the default mode network. *Neurobiology of aging* 33, 1564-1578.
- Alexander, R.A., 1990. A note on averaging correlations. *Bulletin of the Psychonomic Society* 28, 335-336.
- Allen, E.A., Erhardt, E.B., Wei, Y., Eichele, T., Calhoun, V.D., 2012. Capturing inter-subject variability with group independent component analysis of fMRI data: a simulation study. *Neuroimage* 59, 4141-4159.
- Allison, T., Puce, A., McCarthy, G., 2000. Social perception from visual cues: role of the STS region. *Trends in cognitive sciences* 4, 267-278.
- Babiloni, F., Cincotti, F., Babiloni, C., Carducci, F., Mattia, D., Astolfi, L., Basilisco, A., Rossini, P.M., Ding, L., Ni, Y., 2005. Estimation of the cortical functional connectivity with the multimodal integration of high-resolution EEG and fMRI data by directed transfer function. *Neuroimage* 24, 118-131.
- Baillet, S., Garnero, L., 1997. A Bayesian approach to introducing anatomo-functional priors in the EEG/MEG inverse problem. *Ieee Transactions on Biomedical Engineering* 44, 374-385.
- Baillet, S., Mosher, J.C., Leahy, R.M., 2001. Electromagnetic brain mapping. *IEEE Signal Processing Magazine* 18, 14-30.
- Barnes, G.R., Hillebrand, A., 2003. Statistical flattening of MEG beamformer images. *Human brain mapping* 18, 1-12.
- Barry, R.J., Clarke, A.R., Johnstone, S.J., Brown, C.R., 2009. EEG differences in children between eyes-closed and eyes-open resting conditions. *Clinical Neurophysiology* 120, 1806-1811.
- Barry, R.J., Clarke, A.R., Johnstone, S.J., Magee, C.A., Rushby, J.A., 2007. EEG differences between eyes-closed and eyes-open resting conditions. *Clinical Neurophysiology* 118, 2765-2773.
- Bartlett, M., 1935. Some aspects of the time-correlation problem in regard to tests of significance. *Journal of the Royal Statistical Society* 98, 536-543.

- Bassett, D.S., Nelson, B.G., Mueller, B.A., Camchong, J., Lim, K.O., 2012. Altered resting state complexity in schizophrenia. *Neuroimage* 59, 2196-2207.
- Beckmann, C.F., DeLuca, M., Devlin, J.T., Smith, S.M., 2005. Investigations into resting-state connectivity using independent component analysis. *Philosophical Transactions of the Royal Society B-Biological Sciences* 360, 1001-1013.
- Beckmann, C.F., Mackay, C.E., Filippini, N., Smith, S.M., 2009. Group comparison of resting-state fMRI data using multi-subject ICA and dual regression. *Neuroimage* 47, S148.
- Ben-Tal, A., Nemirovski, A., 2001. Lectures on modern convex optimization: analysis, algorithms, and engineering applications. Siam.
- Birn, R.M., Diamond, J.B., Smith, M.A., Bandettini, P.A., 2006. Separating respiratory-variation-related fluctuations from neuronal-activity-related fluctuations in fMRI. *Neuroimage* 31, 1536-1548.
- Biswal, B., Yetkin, F.Z., Haughton, V.M., Hyde, J.S., 1995. Functional connectivity in the motor cortex of resting human brain using echo-planar MRI. *Magn Reson Med* 34, 537-541.
- Biswal, B.B., 2012. Resting state fMRI: a personal history. *Neuroimage* 62, 938-944.
- Bonneau, G.-P., Hahmann, S., Nielson, G.M., 1996. Blac-wavelets: a multiresolution analysis with non-nested spaces. *Visualization'96. Proceedings. IEEE*, pp. 43-48.
- Bressler, S.L., Menon, V., 2010. Large-scale brain networks in cognition: emerging methods and principles. *Trends in cognitive sciences* 14, 277-290.
- Brookes, M.J., Groom, M.J., Liuzzi, L., Hill, R.M., Smith, H.J., Briley, P.M., Hall, E.L., Hunt, B.A., Gascoyne, L.E., Taylor, M.J., 2018. Altered temporal stability in dynamic neural networks underlies connectivity changes in neurodevelopment. *Neuroimage* 174, 563-575.
- Brookes, M.J., Hale, J.R., Zumer, J.M., Stevenson, C.M., Francis, S.T., Barnes, G.R., Owen, J.P., Morris, P.G., Nagarajan, S.S., 2011a. Measuring functional connectivity using MEG: methodology and comparison with fcMRI. *Neuroimage* 56, 1082-1104.
- Brookes, M.J., Tewarie, P.K., Hunt, B.A.E., Robson, S.E., Gascoyne, L.E., Liddle, E.B., Liddle, P.F., Morris, P.G., 2016. A multi-layer network approach to MEG connectivity analysis. *Neuroimage* 132, 425-438.
- Brookes, M.J., Woolrich, M., Luckhoo, H., Price, D., Hale, J.R., Stephenson, M.C., Barnes, G.R., Smith, S.M., Morris, P.G., 2011b. Investigating the electrophysiological basis of resting state networks using magnetoencephalography. *Proceedings of the National Academy of Sciences of the United States of America* 108, 16783-16788.

Buckner, R.L., Andrews - Hanna, J.R., Schacter, D.L., 2008. The brain's default network. *Annals of the New York Academy of Sciences* 1124, 1-38.

Buckner, R.L., Vincent, J.L., 2007. Unrest at rest: default activity and spontaneous network correlations. *Neuroimage* 37, 1091-1096.

Calhoun, V.D., Adali, T., 2012. Multisubject independent component analysis of fMRI: a decade of intrinsic networks, default mode, and neurodiagnostic discovery. *IEEE reviews in biomedical engineering* 5, 60-73.

Calhoun, V.D., Liu, J., Adali, T., 2009. A review of group ICA for fMRI data and ICA for joint inference of imaging, genetic, and ERP data. *Neuroimage* 45, S163-S172.

Candes, E.J., Tao, T., 2005. Decoding by linear programming. *IEEE transactions on information theory* 51, 4203-4215.

Canolty, R.T., Edwards, E., Dalal, S.S., Soltani, M., Nagarajan, S.S., Kirsch, H.E., Berger, M.S., Barbaro, N.M., Knight, R.T., 2006. High gamma power is phase-locked to theta oscillations in human neocortex. *Science* 313, 1626-1628.

Cao, C., Slobounov, S., 2010. Alteration of cortical functional connectivity as a result of traumatic brain injury revealed by graph theory, ICA, and sLORETA analyses of EEG signals. *IEEE Transactions on Neural Systems and Rehabilitation Engineering* 18, 11-19.

Castellanos, F.X., Proal, E., 2012. Large-scale brain systems in ADHD: beyond the prefrontal–striatal model. *Trends in cognitive sciences* 16, 17-26.

Cha, Y.-H., 2009. Mal de débarquement. *Seminars in neurology*. © Thieme Medical Publishers, pp. 520-527.

Cha, Y.-H., Chakrapani, S., Craig, A., Baloh, R.W., 2012. Metabolic and functional connectivity changes in mal de débarquement syndrome. *PLoS One* 7, e49560.

Cha, Y.-H., Cui, Y., Baloh, R.W., 2013. Repetitive transcranial magnetic stimulation for mal de débarquement syndrome. *Otology & neurotology: official publication of the American Otological Society, American Neurotology Society [and] European Academy of Otology and Neurotology* 34, 175.

Cha, Y.-H., Deblieck, C., Wu, A.D., 2016a. Double-blind sham-controlled crossover trial of repetitive transcranial magnetic stimulation for Mal de Débarquement Syndrome. *Otology & Neurotology* 37, 805-812.

Cha, Y.-H., Urbano, D., Pariseau, N., 2016b. Randomized single blind sham controlled trial of adjunctive home-based tDCS after rTMS for mal de débarquement syndrome: safety, efficacy, and participant satisfaction assessment. *Brain stimulation* 9, 537-544.

Cha, Y.H., 2015. Mal de débarquement syndrome: new insights. *Annals of the New York Academy of Sciences* 1343, 63-68.

Chang, C., Glover, G.H., 2010. Time–frequency dynamics of resting-state brain connectivity measured with fMRI. *Neuroimage* 50, 81-98.

Chang, W.-T., Nummenmaa, A., Hsieh, J.-C., Lin, F.-H., 2010. Spatially sparse source cluster modeling by compressive neuromagnetic tomography. *Neuroimage* 53, 146-160.

Chen, C.P., Keown, C.L., Jahedi, A., Nair, A., Pflieger, M.E., Bailey, B.A., Müller, R.-A., 2015. Diagnostic classification of intrinsic functional connectivity highlights somatosensory, default mode, and visual regions in autism. *NeuroImage: Clinical* 8, 238-245.

Chen, J.L., Ros, T., Gruzelier, J.H., 2013. Dynamic changes of ICA - derived EEG functional connectivity in the resting state. *Human brain mapping* 34, 852-868.

Chen, T., Yang, M., Liu, B., Liu, Y.T., Zhang, H.X., Liu, C.C., Zhu, Y., Huang, Z.C., Yuan, T.F., 2016. The Resting-State Functional Connectivity of the Default Mode Networks in Patients With Obstructive Sleep Apnea-Hypopnea Syndrome. *CNS Neurol Disord Drug Targets*.

Chenji, S., Jha, S., Lee, D., Brown, M., Seres, P., Mah, D., Kalra, S., 2016. Investigating default mode and sensorimotor network connectivity in amyotrophic lateral sclerosis. *PLoS One* 11, e0157443.

Chung, M.K., Robbins, S.M., Dalton, K.M., Davidson, R.J., Alexander, A.L., Evans, A.C., 2005. Cortical thickness analysis in autism with heat kernel smoothing. *Neuroimage* 25, 1256-1265.

Chung, M.K., Worsley, K.J., Nacewicz, B.M., Dalton, K.M., Davidson, R.J., 2010. General multivariate linear modeling of surface shapes using SurfStat. *Neuroimage* 53, 491-505.

Cohen, D., Cuffin, B.N., Yunokuchi, K., Maniewski, R., Purcell, C., Cosgrove, G.R., Ives, J., Kennedy, J.G., Schomer, D.L., 1990. MEG versus EEG localization test using implanted sources in the human brain. *Annals of neurology* 28, 811-817.

Colclough, G.L., Woolrich, M.W., Tewarie, P., Brookes, M.J., Quinn, A.J., Smith, S.M., 2016. How reliable are MEG resting-state connectivity metrics? *Neuroimage* 138, 284-293.

Cole, D.M., Smith, S.M., Beckmann, C.F., 2010. Advances and pitfalls in the analysis and interpretation of resting-state fMRI data. *Frontiers in systems neuroscience* 4.

Corbetta, M., Akbudak, E., Conturo, T.E., Snyder, A.Z., Ollinger, J.M., Drury, H.A., Linenweber, M.R., Petersen, S.E., Raichle, M.E., Van Essen, D.C., 1998. A common network of functional areas for attention and eye movements. *Neuron* 21, 761-773.

Crone, N.E., Miglioretti, D.L., Gordon, B., Sieracki, J.M., Wilson, M.T., Uematsu, S., Lesser, R.P., 1998. Functional mapping of human sensorimotor cortex with

electrocorticographic spectral analysis. I. Alpha and beta event-related desynchronization. *Brain: a journal of neurology* 121, 2271-2299.

Crone, N.E., Sinai, A., Korzeniewska, A., 2006. High-frequency gamma oscillations and human brain mapping with electrocorticography. *Progress in brain research* 159, 275-295.

da Silva, F.L., 2013. EEG and MEG: relevance to neuroscience. *Neuron* 80, 1112-1128.

Dale, A.M., Sereno, M.I., 1993. Improved localization of cortical activity by combining EEG and MEG with MRI cortical surface reconstruction: a linear approach. *Journal of Cognitive Neuroscience* 5, 162-176.

Damoiseaux, J., Beckmann, C., Arigita, E.S., Barkhof, F., Scheltens, P., Stam, C., Smith, S., Rombouts, S., 2007. Reduced resting-state brain activity in the “default network” in normal aging. *Cerebral cortex* 18, 1856-1864.

Damoiseaux, J., Rombouts, S., Barkhof, F., Scheltens, P., Stam, C., Smith, S.M., Beckmann, C., 2006. Consistent resting-state networks across healthy subjects. *Proceedings of the National Academy of Sciences* 103, 13848-13853.

Dang, P.P., Chau, P.M., 2000. Image encryption for secure internet multimedia applications. *Consumer Electronics, 2000. ICCE. 2000 Digest of Technical Papers. International Conference on. IEEE*, pp. 6-7.

De Luca, M., Beckmann, C., De Stefano, N., Matthews, P., Smith, S.M., 2006. fMRI resting state networks define distinct modes of long-distance interactions in the human brain. *Neuroimage* 29, 1359-1367.

de Pasquale, F., Della Penna, S., Snyder, A.Z., Lewis, C., Mantini, D., Marzetti, L., Belardinelli, P., Ciancetta, L., Pizzella, V., Romani, G.L., Corbetta, M., 2010. Temporal dynamics of spontaneous MEG activity in brain networks. *Proc Natl Acad Sci U S A* 107, 6040-6045.

Deco, G., Jirsa, V.K., McIntosh, A.R., 2011. Emerging concepts for the dynamical organization of resting-state activity in the brain. *Nature Reviews Neuroscience* 12, 43-56.

Delorme, A., Makeig, S., 2004. EEGLAB: an open source toolbox for analysis of single-trial EEG dynamics including independent component analysis. *Journal of Neuroscience Methods* 134, 9-21.

Di Martino, A., Scheres, A., Margulies, D.S., Kelly, A., Uddin, L.Q., Shehzad, Z., Biswal, B., Walters, J.R., Castellanos, F.X., Milham, M.P., 2008. Functional connectivity of human striatum: a resting state FMRI study. *Cerebral cortex* 18, 2735-2747.

Ding, L., 2009. Reconstructing cortical current density by exploring sparseness in the transform domain. *Physics in Medicine & Biology* 54, 2683.

- Ding, L., He, B., 2008. Sparse source imaging in electroencephalography with accurate field modeling. *Human brain mapping* 29, 1053-1067.
- Ding, L., Shou, G., Yuan, H., Urbano, D., Cha, Y.-H., 2014. Lasting modulation effects of rTMS on neural activity and connectivity as revealed by resting-state EEG. *Ieee Transactions on Biomedical Engineering* 61, 2070-2080.
- Ding, L., Wilke, C., Xu, B., Xu, X., van Drongelene, W., Kohrman, M., He, B., 2007. EEG source imaging: correlate source locations and extents with ECoG and surgical resections in epilepsy patients. *Journal of clinical neurophysiology: official publication of the American Electroencephalographic Society* 24, 130.
- Ding, L., Yuan, H., 2012. Sparse electromagnetic source imaging using EEG and MEG. *Engineering in Medicine and Biology Society (EMBC), 2012 Annual International Conference of the IEEE. IEEE*, pp. 6224-6227.
- Ding, L., Yuan, H., 2013. Simultaneous EEG and MEG source reconstruction in sparse electromagnetic source imaging. *Human brain mapping* 34, 775-795.
- Ding, L., Zhu, M., Liao, K., 2013. Wavelet based sparse source imaging technique. *Engineering in Medicine and Biology Society (EMBC), 2013 35th Annual International Conference of the IEEE. IEEE*, pp. 5418-5421.
- Donoho, D.L., 2006. For most large underdetermined systems of linear equations the minimal Communications on Pure and Applied Mathematics: A Journal Issued by the Courant Institute of Mathematical Sciences 59, 797-829.
- Finn, E.S., Shen, X., Scheinost, D., Rosenberg, M.D., Huang, J., Chun, M.M., Papademetris, X., Constable, R.T., 2015. Functional connectome fingerprinting: identifying individuals using patterns of brain connectivity. *Nature neuroscience* 18, 1664.
- Fischl, B., 2012. FreeSurfer. *Neuroimage* 62, 774-781.
- Fisher, R.A., 1915. Frequency distribution of the values of the correlation coefficient in samples from an indefinitely large population. *Biometrika* 10, 507-521.
- Fox, M.D., Raichle, M.E., 2007. Spontaneous fluctuations in brain activity observed with functional magnetic resonance imaging. *Nat Rev Neurosci* 8, 700-711.
- Fox, M.D., Snyder, A.Z., Vincent, J.L., Corbetta, M., Van Essen, D.C., Raichle, M.E., 2005. The human brain is intrinsically organized into dynamic, anticorrelated functional networks. *Proceedings of the National Academy of Sciences of the United States of America* 102, 9673-9678.
- Fox, P.T., Mintun, M.A., Reiman, E.M., Raichle, M.E., 1988. Enhanced detection of focal brain responses using intersubject averaging and change-distribution analysis of subtracted PET images. *Journal of Cerebral Blood Flow & Metabolism* 8, 642-653.

- Freeman, W.J., Rogers, L.J., Holmes, M.D., Silbergeld, D.L., 2000. Spatial spectral analysis of human electrocorticograms including the alpha and gamma bands. *Journal of Neuroscience Methods* 95, 111-121.
- Friston, K.J., Jezzard, P., Turner, R., 1994. Analysis of functional MRI time - series. *Human brain mapping* 1, 153-171.
- Friston, K.J., Williams, S., Howard, R., Frackowiak, R.S., Turner, R., 1996. Movement - related effects in fMRI time - series. *Magnetic Resonance in Medicine* 35, 346-355.
- Goldman, R.I., Stern, J.M., Engel Jr, J., Cohen, M.S., 2002. Simultaneous EEG and fMRI of the alpha rhythm. *Neuroreport* 13, 2487.
- Golub, G.H., Heath, M., Wahba, G., 1979. Generalized cross-validation as a method for choosing a good ridge parameter. *Technometrics* 21, 215-223.
- Goncalves, S., De Munck, J., Pouwels, P., Schoonhoven, R., Kuijer, J., Maurits, N., Hoogduin, J., Van Someren, E., Heethaar, R., Da Silva, F.L., 2006. Correlating the alpha rhythm to BOLD using simultaneous EEG/fMRI: inter-subject variability. *Neuroimage* 30, 203-213.
- Goodale, M.A., Milner, A.D., 1992. Separate visual pathways for perception and action. *Trends in neurosciences* 15, 20-25.
- Gorodnitsky, I.F., George, J.S., Rao, B.D., 1995. Neuromagnetic source imaging with FOCUSS: a recursive weighted minimum norm algorithm. *Electroencephalography and clinical Neurophysiology* 95, 231-251.
- Grech, R., Cassar, T., Muscat, J., Camilleri, K.P., Fabri, S.G., Zervakis, M., Xanthopoulos, P., Sakkalis, V., Vanrumste, B., 2008. Review on solving the inverse problem in EEG source analysis. *Journal of neuroengineering and rehabilitation* 5, 25.
- Greicius, M.D., Flores, B.H., Menon, V., Glover, G.H., Solvason, H.B., Kenna, H., Reiss, A.L., Schatzberg, A.F., 2007. Resting-state functional connectivity in major depression: abnormally increased contributions from subgenual cingulate cortex and thalamus. *Biological psychiatry* 62, 429-437.
- Greicius, M.D., Krasnow, B., Reiss, A.L., Menon, V., 2003. Functional connectivity in the resting brain: a network analysis of the default mode hypothesis. *Proceedings of the National Academy of Sciences* 100, 253-258.
- Grova, C., Daunizeau, J., Lina, J.-M., Bénar, C., Benali, H., Gotman, J., 2006. Evaluation of EEG localization methods using realistic simulations of interictal spikes. *Neuroimage* 29, 734-753.
- Gur, R.C., Mozley, L.H., Mozley, P.D., Resnick, S.M., Karp, J.S., Alavi, A., Arnold, S.E., Gur, R.E., 1995. Sex differences in regional cerebral glucose metabolism during a resting state. *Science* 267, 528-531.

- Hagler, D.J., Saygin, A.P., Sereno, M.I., 2006. Smoothing and cluster thresholding for cortical surface-based group analysis of fMRI data. *Neuroimage* 33, 1093-1103.
- Hämäläinen, M., Hari, R., Ilmoniemi, R.J., Knuutila, J., Lounasmaa, O.V., 1993. Magnetoencephalography—theory, instrumentation, and applications to noninvasive studies of the working human brain. *Reviews of modern Physics* 65, 413.
- Hamalainen, M.S., Ilmoniemi, R.J., 1994. Interpreting Magnetic-Fields of the Brain - Minimum Norm Estimates. *Medical & Biological Engineering & Computing* 32, 35-42.
- Hämäläinen, M.S., Ilmoniemi, R.J., 1984. Interpreting measured magnetic fields of the brain: estimates of current distributions. Helsinki University of Technology, Department of Technical Physics.
- Hamalainen, M.S., Sarvas, J., 1989. Realistic conductivity geometry model of the human head for interpretation of neuromagnetic data. *Ieee Transactions on Biomedical Engineering* 36, 165-171.
- Hawellek, D.J., Hipp, J.F., Lewis, C.M., Corbetta, M., Engel, A.K., 2011. Increased functional connectivity indicates the severity of cognitive impairment in multiple sclerosis. *Proceedings of the National Academy of Sciences* 108, 19066-19071.
- Herculano-Houzel, S., 2009. The human brain in numbers: a linearly scaled-up primate brain. *Frontiers in human neuroscience* 3, 31.
- Hindriks, R., Adhikari, M.H., Murayama, Y., Ganzetti, M., Mantini, D., Logothetis, N.K., Deco, G., 2016. Can sliding-window correlations reveal dynamic functional connectivity in resting-state fMRI? *Neuroimage* 127, 242-256.
- Hipp, J.F., Engel, A.K., Siegel, M., 2011. Oscillatory synchronization in large-scale cortical networks predicts perception. *Neuron* 69, 387-396.
- Hipp, J.F., Hawellek, D.J., Corbetta, M., Siegel, M., Engel, A.K., 2012. Large-scale cortical correlation structure of spontaneous oscillatory activity. *Nature neuroscience* 15, 884-890.
- Honey, C., Sporns, O., Cammoun, L., Gigandet, X., Thiran, J.-P., Meuli, R., Hagmann, P., 2009. Predicting human resting-state functional connectivity from structural connectivity. *Proceedings of the National Academy of Sciences* 106, 2035-2040.
- Hyvärinen, A., Karhunen, J., Oja, E., 2004. *Independent component analysis*. John Wiley & Sons.
- Hyvärinen, A., Oja, E., 1997. A fast fixed-point algorithm for independent component analysis. *Neural computation* 9, 1483-1492.
- Hyvärinen, A., Oja, E., 2000. *Independent component analysis: algorithms and applications*. *Neural networks* 13, 411-430.

- Ille, N., Berg, P., Scherg, M., 2002. Artifact correction of the ongoing EEG using spatial filters based on artifact and brain signal topographies. *Journal of clinical neurophysiology* 19, 113-124.
- James, C.J., Hesse, C.W., 2004. Independent component analysis for biomedical signals. *Physiological measurement* 26, R15.
- Jann, K., Kottlow, M., Dierks, T., Boesch, C., Koenig, T., 2010. Topographic electrophysiological signatures of fMRI resting state networks. *PLoS One* 5, e12945.
- Jao, T., Vértes, P.E., Alexander-Bloch, A.F., Tang, I.-N., Yu, Y.-C., Chen, J.-H., Bullmore, E.T., 2013. Volitional eyes opening perturbs brain dynamics and functional connectivity regardless of light input. *Neuroimage* 69, 21-34.
- Joyce, C.A., Gorodnitsky, I.F., Kutas, M., 2004. Automatic removal of eye movement and blink artifacts from EEG data using blind component separation. *Psychophysiology* 41, 313-325.
- Kandel, E.R., Schwartz, J.H., Jessell, T.M., Biochemistry, D.o., Jessell, M.B.T., Siegelbaum, S., Hudspeth, A., 2000. *Principles of neural science*. McGraw-hill New York.
- Kilpatrick, L., Zald, D., Pardo, J., Cahill, L., 2006. Sex-related differences in amygdala functional connectivity during resting conditions. *Neuroimage* 30, 452-461.
- Klimesch, W., 1999. EEG alpha and theta oscillations reflect cognitive and memory performance: a review and analysis. *Brain research reviews* 29, 169-195.
- Kounios, J., Fleck, J.I., Green, D.L., Payne, L., Stevenson, J.L., Bowden, E.M., Jung-Beeman, M., 2008. The origins of insight in resting-state brain activity. *Neuropsychologia* 46, 281-291.
- Ku, J., Cho, Y.W., Lee, Y.S., Moon, H.-J., Chang, H., Earley, C.J., Allen, R.P., 2014. Functional connectivity alternation of the thalamus in restless legs syndrome patients during the asymptomatic period: a resting-state connectivity study using functional magnetic resonance imaging. *Sleep medicine* 15, 289-294.
- Lai, Y., Van Drongelen, W., Ding, L., Hecox, K., Towle, V., Frim, D., He, B., 2005. Estimation of in vivo human brain-to-skull conductivity ratio from simultaneous extra- and intra-cranial electrical potential recordings. *Clinical Neurophysiology* 116, 456-465.
- Laufs, H., 2008. Endogenous brain oscillations and related networks detected by surface EEG - combined fMRI. *Human brain mapping* 29, 762-769.
- Laufs, H., Kleinschmidt, A., Beyerle, A., Eger, E., Salek-Haddadi, A., Preibisch, C., Krakow, K., 2003a. EEG-correlated fMRI of human alpha activity. *Neuroimage* 19, 1463-1476.

- Laufs, H., Krakow, K., Sterzer, P., Eger, E., Beyerle, A., Salek-Haddadi, A., Kleinschmidt, A., 2003b. Electroencephalographic signatures of attentional and cognitive default modes in spontaneous brain activity fluctuations at rest. *Proceedings of the National Academy of Sciences* 100, 11053-11058.
- Lee, T.-W., Girolami, M., Sejnowski, T.J., 1999. Independent component analysis using an extended infomax algorithm for mixed subgaussian and supergaussian sources. *Neural computation* 11, 417-441.
- Li, C., Yuan, H., Shou, G., Cha, Y.-H., Sunderam, S., Besio, W., Ding, L., 2018. Cortical Statistical Correlation Tomography of EEG Resting State Networks. *Frontiers in Neuroscience* 12, 365.
- Li, C., Yuan, H., Urbano, D., Cha, Y.-H., Ding, L., 2017. ICA on sensor or source data: A comparison study in deriving resting state networks from EEG. *Engineering in Medicine and Biology Society (EMBC), 2017 39th Annual International Conference of the IEEE. IEEE*, pp. 3604-3607.
- Liao, K., Zhu, M., Ding, L., 2013. A new wavelet transform to sparsely represent cortical current densities for EEG/MEG inverse problems. *Computer Methods and Programs in Biomedicine* 111, 376-388.
- Liao, K., Zhu, M., Ding, L., Valette, S., Zhang, W., Dickens, D., 2012. Sparse imaging of cortical electrical current densities via wavelet transforms. *Physics in medicine and biology* 57, 6881.
- Lin, F.-H., Witzel, T., Ahlfors, S.P., Stufflebeam, S.M., Belliveau, J.W., Hämäläinen, M.S., 2006. Assessing and improving the spatial accuracy in MEG source localization by depth-weighted minimum-norm estimates. *Neuroimage* 31, 160-171.
- Liu, Q., Farahibozorg, S., Porcaro, C., Wenderoth, N., Mantini, D., 2017. Detecting large - scale networks in the human brain using high - density electroencephalography. *Human brain mapping* 38, 4631-4643.
- Liu, X., Duyn, J.H., 2013. Time-varying functional network information extracted from brief instances of spontaneous brain activity. *Proceedings of the National Academy of Sciences* 110, 4392-4397.
- Logothetis, N.K., 2008. What we can do and what we cannot do with fMRI. *Nature* 453, 869-878.
- Makeig, S., Bell, A.J., Jung, T.-P., Sejnowski, T.J., 1996. Independent component analysis of electroencephalographic data. *Advances in neural information processing systems*, 145-151.
- Mantini, D., Perrucci, M.G., Del Gratta, C., Romani, G.L., Corbetta, M., 2007. Electrophysiological signatures of resting state networks in the human brain. *Proceedings of the National Academy of Sciences* 104, 13170-13175.

- Marx, E., Deutschländer, A., Stephan, T., Dieterich, M., Wiesmann, M., Brandt, T., 2004. Eyes open and eyes closed as rest conditions: impact on brain activation patterns. *Neuroimage* 21, 1818-1824.
- Mayeli, A., Zotev, V., Refai, H., Bodurka, J., 2016. Real-Time EEG artifact correction during fMRI using ICA. *Journal of Neuroscience Methods* 274, 27-37.
- Menon, V., 2011. Large-scale brain networks and psychopathology: a unifying triple network model. *Trends in cognitive sciences* 15, 483-506.
- Michel, C.M., Murray, M.M., Lantz, G., Gonzalez, S., Spinelli, L., de Peralta, R.G., 2004. EEG source imaging. *Clinical Neurophysiology* 115, 2195-2222.
- Mihcak, M.K., Kozintsev, I., Ramchandran, K., Moulin, P., 1999. Low-complexity image denoising based on statistical modeling of wavelet coefficients. *IEEE Signal Processing Letters* 6, 300-303.
- Miltner, W.H., Braun, C., Arnold, M., Witte, H., Taub, E., 1999. Coherence of gamma-band EEG activity as a basis for associative learning. *Nature* 397, 434.
- Mitra, P.P., Ogawa, S., Hu, X., Uğurbil, K., 1997. The nature of spatiotemporal changes in cerebral hemodynamics as manifested in functional magnetic resonance imaging. *Magnetic Resonance in Medicine* 37, 511-518.
- Molins, A., Stufflebeam, S.M., Brown, E.N., Hämäläinen, M.S., 2008. Quantification of the benefit from integrating MEG and EEG data in minimum ℓ_2 -norm estimation. *Neuroimage* 42, 1069-1077.
- Mosher, J.C., Leahy, R.M., Lewis, P.S., 1999. EEG and MEG: forward solutions for inverse methods. *Ieee Transactions on Biomedical Engineering* 46, 245-259.
- Nolan, H., Whelan, R., Reilly, R., 2010. FASTER: fully automated statistical thresholding for EEG artifact rejection. *Journal of Neuroscience Methods* 192, 152-162.
- Nugent, A.C., Robinson, S.E., Coppola, R., Furey, M.L., Zarate, C.A., 2015. Group differences in MEG-ICA derived resting state networks: application to major depressive disorder. *Neuroimage* 118, 1-12.
- Nunez, P.L., Silberstein, R.B., 2000. On the relationship of synaptic activity to macroscopic measurements: does co-registration of EEG with fMRI make sense? *Brain topography* 13, 79-96.
- Oh, S.W., Harris, J.A., Ng, L., Winslow, B., Cain, N., Mihalas, S., Wang, Q., Lau, C., Kuan, L., Henry, A.M., 2014. A mesoscale connectome of the mouse brain. *Nature* 508, 207.
- Ossandón, T., Jerbi, K., Vidal, J.R., Bayle, D.J., Henaff, M.-A., Jung, J., Minotti, L., Bertrand, O., Kahane, P., Lachaux, J.-P., 2011. Transient suppression of broadband

gamma power in the default-mode network is correlated with task complexity and subject performance. *Journal of Neuroscience* 31, 14521-14530.

Park, H.-J., Friston, K., 2013. Structural and functional brain networks: from connections to cognition. *Science* 342, 1238411.

Pascual-Marqui, R.D., 1999. Review of methods for solving the EEG inverse problem. *International journal of bioelectromagnetism* 1, 75-86.

Pascual-Marqui, R.D., 2007. Discrete, 3D distributed, linear imaging methods of electric neuronal activity. Part 1: exact, zero error localization. arXiv preprint arXiv:0710.3341.

Pascual-Marqui, R.D., Lehmann, D., Koenig, T., Kochi, K., Merlo, M.C., Hell, D., Koukkou, M., 1999. Low resolution brain electromagnetic tomography (LORETA) functional imaging in acute, neuroleptic-naive, first-episode, productive schizophrenia. *Psychiatry Research: Neuroimaging* 90, 169-179.

Pereira, F.R., Alessio, A., Sercheli, M.S., Pedro, T., Bilevicius, E., Rondina, J.M., Ozelo, H.F., Castellano, G., Covolan, R.J., Damasceno, B.P., 2010. Asymmetrical hippocampal connectivity in mesial temporal lobe epilepsy: evidence from resting state fMRI. *BMC neuroscience* 11, 66.

Pijn, J.P., Van Neerven, J., Noest, A., da Silva, F.H.L., 1991. Chaos or noise in EEG signals; dependence on state and brain site. *Electroencephalography and clinical Neurophysiology* 79, 371-381.

Raichle, M.E., MacLeod, A.M., Snyder, A.Z., Powers, W.J., Gusnard, D.A., Shulman, G.L., 2001. A default mode of brain function. *Proceedings of the National Academy of Sciences* 98, 676-682.

Ramkumar, P., Parkkonen, L., Hari, R., Hyvärinen, A., 2012. Characterization of neuromagnetic brain rhythms over time scales of minutes using spatial independent component analysis. *Human brain mapping* 33, 1648-1662.

Ramkumar, P., Parkkonen, L., Hyvärinen, A., 2014. Group-level spatial independent component analysis of Fourier envelopes of resting-state MEG data. *Neuroimage* 86, 480-491.

Rangaswamy, M., Porjesz, B., Chorlian, D.B., Wang, K., Jones, K.A., Bauer, L.O., Rohrbaugh, J., O'connor, S.J., Kuperman, S., Reich, T., 2002. Beta power in the EEG of alcoholics. *Biological psychiatry* 52, 831-842.

Richiardi, J., Altmann, A., Milazzo, A.-C., Chang, C., Chakravarty, M.M., Banaschewski, T., Barker, G.J., Bokde, A.L., Bromberg, U., Büchel, C., 2015. Correlated gene expression supports synchronous activity in brain networks. *Science* 348, 1241-1244.

Ritter, P., Villringer, A., 2006. simultaneous EEG-fMRI. *Neuroscience & Biobehavioral Reviews* 30, 823-838.

- Robinson, P., Rennie, C., Wright, J., Bahramali, H., Gordon, E., Rowe, D., 2001. Prediction of electroencephalographic spectra from neurophysiology. *Physical Review E* 63, 021903.
- Rombouts, S.A., Barkhof, F., Goekoop, R., Stam, C.J., Scheltens, P., 2005. Altered resting state networks in mild cognitive impairment and mild Alzheimer's disease: an fMRI study. *Human brain mapping* 26, 231-239.
- Roy, A.K., Shehzad, Z., Margulies, D.S., Kelly, A.C., Uddin, L.Q., Gotimer, K., Biswal, B.B., Castellanos, F.X., Milham, M.P., 2009. Functional connectivity of the human amygdala using resting state fMRI. *Neuroimage* 45, 614-626.
- Rutter, L., Carver, F.W., Holroyd, T., Nadar, S.R., Mitchell - Francis, J., Apud, J., Weinberger, D.R., Coppola, R., 2009. Magnetoencephalographic gamma power reduction in patients with schizophrenia during resting condition. *Human brain mapping* 30, 3254-3264.
- Scheeringa, R., Bastiaansen, M.C., Petersson, K.M., Oostenveld, R., Norris, D.G., Hagoort, P., 2008. Frontal theta EEG activity correlates negatively with the default mode network in resting state. *International Journal of Psychophysiology* 67, 242-251.
- Shmueli, K., van Gelderen, P., de Zwart, J.A., Horovitz, S.G., Fukunaga, M., Jansma, J.M., Duyn, J.H., 2007. Low-frequency fluctuations in the cardiac rate as a source of variance in the resting-state fMRI BOLD signal. *Neuroimage* 38, 306-320.
- Shou, G., Ding, L., Dasari, D., 2012. Probing neural activations from continuous EEG in a real-world task: time-frequency independent component analysis. *Journal of Neuroscience Methods* 209, 22-34.
- Shou, G., Yuan, H., Urbano, D., Cha, Y.-H., Ding, L., 2014. Changes of symptom and EEG in mal de débarquement syndrome patients after repetitive transcranial magnetic stimulation over bilateral prefrontal cortex: a pilot study. *Engineering in Medicine and Biology Society (EMBC), 2014 36th Annual International Conference of the IEEE. IEEE*, pp. 4294-4297.
- Siems, M., Pape, A.-A., Hipp, J.F., Siegel, M., 2016. Measuring the cortical correlation structure of spontaneous oscillatory activity with EEG and MEG. *Neuroimage* 129, 345-355.
- Silver, N.C., Dunlap, W.P., 1987. Averaging correlation coefficients: should Fisher's z transformation be used? *Journal of Applied Psychology* 72, 146.
- Smith, S.M., Fox, P.T., Miller, K.L., Glahn, D.C., Fox, P.M., Mackay, C.E., Filippini, N., Watkins, K.E., Toro, R., Laird, A.R., 2009. Correspondence of the brain's functional architecture during activation and rest. *Proceedings of the National Academy of Sciences* 106, 13040-13045.

Smith, S.M., Miller, K.L., Moeller, S., Xu, J., Auerbach, E.J., Woolrich, M.W., Beckmann, C.F., Jenkinson, M., Andersson, J., Glasser, M.F., 2012. Temporally-independent functional modes of spontaneous brain activity. *Proceedings of the National Academy of Sciences* 109, 3131-3136.

Smith, S.M., Nichols, T.E., 2009. Threshold-free cluster enhancement: addressing problems of smoothing, threshold dependence and localisation in cluster inference. *Neuroimage* 44, 83-98.

Sockeel, S., Schwartz, D., Pélégriani-Issac, M., Benali, H., 2016. Large-scale functional networks identified from resting-state EEG using spatial ICA. *PLoS One* 11, e0146845.

Sokoloff, L., Mangold, R., Wechsler, R.L., Kennedy, C., Kety, S.S., 1955. The effect of mental arithmetic on cerebral circulation and metabolism. *The Journal of clinical investigation* 34, 1101-1108.

Sorg, C., Riedl, V., Mühlau, M., Calhoun, V.D., Eichele, T., Läer, L., Drzezga, A., Förstl, H., Kurz, A., Zimmer, C., 2007. Selective changes of resting-state networks in individuals at risk for Alzheimer's disease. *Proceedings of the National Academy of Sciences* 104, 18760-18765.

Sridharan, D., Levitin, D.J., Menon, V., 2008. A critical role for the right fronto-insular cortex in switching between central-executive and default-mode networks. *Proceedings of the National Academy of Sciences* 105, 12569-12574.

Stam, C.J., Nolte, G., Daffertshofer, A., 2007. Phase lag index: assessment of functional connectivity from multi channel EEG and MEG with diminished bias from common sources. *Human brain mapping* 28, 1178-1193.

Steriade, M., Llinás, R.R., 1988. The functional states of the thalamus and the associated neuronal interplay. *Physiological reviews* 68, 649-742.

Sturm, J.F., 1999. Using SeDuMi 1.02, a MATLAB toolbox for optimization over symmetric cones. *Optimization methods and software* 11, 625-653.

Teplan, M., 2002. Fundamentals of EEG measurement. *Measurement science review* 2, 1-11.

Thayaparan, T., Abrol, S., Riseborough, E., Stankovic, L., Lamothe, D., Duff, G., 2007. Analysis of radar micro-Doppler signatures from experimental helicopter and human data. *IET Radar, Sonar & Navigation* 1, 289-299.

Tian, L., Wang, J., Yan, C., He, Y., 2011. Hemisphere-and gender-related differences in small-world brain networks: a resting-state functional MRI study. *Neuroimage* 54, 191-202.

Towle, V.L., Bolaños, J., Suarez, D., Tan, K., Grzeszczuk, R., Levin, D.N., Cakmur, R., Frank, S.A., Spire, J.-P., 1993. The spatial location of EEG electrodes: locating the best-

fitting sphere relative to cortical anatomy. *Electroencephalography and clinical Neurophysiology* 86, 1-6.

Uutela, K., Hämäläinen, M., Somersalo, E., 1999. Visualization of magnetoencephalographic data using minimum current estimates. *Neuroimage* 10, 173-180.

van den Broek, S.P., Reinders, F., Donderwinkel, M., Peters, M., 1998. Volume conduction effects in EEG and MEG. *Electroencephalography and clinical Neurophysiology* 106, 522-534.

van den Heuvel, M.P., Stam, C.J., Boersma, M., Pol, H.H., 2008. Small-world and scale-free organization of voxel-based resting-state functional connectivity in the human brain. *Neuroimage* 43, 528-539.

Van Veen, B.D., Van Drongelen, W., Yuchtman, M., Suzuki, A., 1997. Localization of brain electrical activity via linearly constrained minimum variance spatial filtering. *Ieee Transactions on Biomedical Engineering* 44, 867-880.

Vigário, R., Sarela, J., Jousmiki, V., Hamalainen, M., Oja, E., 2000. Independent component approach to the analysis of EEG and MEG recordings. *Ieee Transactions on Biomedical Engineering* 47, 589-593.

Vincent, J.L., Patel, G.H., Fox, M.D., Snyder, A.Z., Baker, J.T., Van Essen, D.C., Zempel, J.M., Snyder, L.H., Corbetta, M., Raichle, M.E., 2007. Intrinsic functional architecture in the anaesthetized monkey brain. *Nature* 447, 83.

Voets, N.L., Adcock, J.E., Stacey, R., Hart, Y., Carpenter, K., Matthews, P.M., Beckmann, C.F., 2009. Functional and structural changes in the memory network associated with left temporal lobe epilepsy. *Human brain mapping* 30, 4070-4081.

Wahba, G., 1990. *Spline models for observational data*. SIAM.

Ward, L.M., 2003. Synchronous neural oscillations and cognitive processes. *Trends in cognitive sciences* 7, 553-559.

Wendel, K., Narra, N.G., Hannula, M., Kauppinen, P., Malmivuo, J., 2008. The influence of CSF on EEG sensitivity distributions of multilayered head models. *Ieee Transactions on Biomedical Engineering* 55, 1454-1456.

Wise, R.G., Ide, K., Poulin, M.J., Tracey, I., 2004. Resting fluctuations in arterial carbon dioxide induce significant low frequency variations in BOLD signal. *Neuroimage* 21, 1652-1664.

Woolrich, M.W., Ripley, B.D., Brady, M., Smith, S.M., 2001. Temporal autocorrelation in univariate linear modeling of fMRI data. *Neuroimage* 14, 1370-1386.

- Yang, H., Long, X.-Y., Yang, Y., Yan, H., Zhu, C.-Z., Zhou, X.-P., Zang, Y.-F., Gong, Q.-Y., 2007. Amplitude of low frequency fluctuation within visual areas revealed by resting-state functional MRI. *Neuroimage* 36, 144-152.
- Yeo, B.T., Krienen, F.M., Sepulcre, J., Sabuncu, M.R., Lashkari, D., Hollinshead, M., Roffman, J.L., Smoller, J.W., Zöllei, L., Polimeni, J.R., 2011. The organization of the human cerebral cortex estimated by intrinsic functional connectivity. *Journal of neurophysiology* 106, 1125-1165.
- Yuan, H., Ding, L., Zhu, M., Zotev, V., Phillips, R., Bodurka, J., 2016. Reconstructing Large-Scale Brain Resting-State Networks from High-Resolution EEG: Spatial and Temporal Comparisons with fMRI. *Brain Connect* 6, 122-135.
- Yuan, H., Liu, T., Szarkowski, R., Rios, C., Ashe, J., He, B., 2010. Negative covariation between task-related responses in alpha/beta-band activity and BOLD in human sensorimotor cortex: an EEG and fMRI study of motor imagery and movements. *Neuroimage* 49, 2596-2606.
- Yuan, H., Shou, G., Urbano, D., Ding, L., Cha, Y.-H., 2017. Resting state functional connectivity signature of treatment effects of rTMS in Mal de Debarquement Syndrome. *Brain Connectivity*.
- Yuan, H., Zotev, V., Phillips, R., Drevets, W.C., Bodurka, J., 2012a. Spatiotemporal dynamics of the brain at rest--exploring EEG microstates as electrophysiological signatures of BOLD resting state networks. *Neuroimage* 60, 2062-2072.
- Yuan, H., Zotev, V., Phillips, R., Drevets, W.C., Bodurka, J., 2012b. Spatiotemporal dynamics of the brain at rest - Exploring EEG microstates as electrophysiological signatures of BOLD resting state networks. *Neuroimage* 60, 2062-2072.
- Zhang, J.J., Ding, J., Li, J.Y., Wang, M., Yuan, Y.S., Zhang, L., Jiang, S.M., Wang, X.X., Zhu, L., Zhang, K.Z., 2017. Abnormal Resting-State Neural Activity and Connectivity of Fatigue in Parkinson's Disease. *CNS Neurosci Ther*.
- Zhu, M., Zhang, W., Dickens, D.L., Ding, L., 2014. Reconstructing spatially extended brain sources via enforcing multiple transform sparseness. *Neuroimage* 86, 280-293.
- Zhu, M., Zhang, W., Dickens, D.L., King, J.A., Ding, L., 2013. Sparse MEG source imaging for reconstructing dynamic sources of interictal spikes in partial epilepsy. *Journal of clinical neurophysiology* 30, 313-328.
- Zhu, X., Zhu, Q., Jiang, C., Shen, H., Wang, F., Liao, W., Yuan, F., 2017. Disrupted Resting-State Default Mode Network in Betel Quid-Dependent Individuals. *Front Psychol* 8, 84.